UC Irvine
UC Irvine Electronic Theses and Dissertations

Title
The roles of föhn and katabatic winds in ice sheet surface melt

Permalink
https://escholarship.org/uc/item/9tw9w5h0

Author
Laffin, Matthew K

Publication Date
2022

Peer reviewed|Thesis/dissertation

eScholarship.org Powered by the California Digital Library
University of California

UNIVERSITY OF CALIFORNIA,
IRVINE

The roles of föhn and katabatic winds in ice sheet surface melt

DISSERTATION

submitted in partial satisfaction of the requirements
for the degree of

DOCTOR OF PHILOSOPHY

in Earth System Science

by

Matthew Keith Laffin

Dissertation Committee:
Professor Charles S. Zender, Chair
Associate Professor Sameer Singh
Professor Eric Rignot

2022

Chapter 2 © 2021 Matthew Keith Laffin and Coauthors
Chapter 3 © 2022 Matthew Keith Laffin and Coauthors
All other materials © 2022 Matthew Keith Laffin

DEDICATION

To those whose lives have been or will be challenged as a result of human caused climate change, in the hope that a better scientific understanding of the relationships between wind, surface melt, and sea level rise may help mitigate some burden to lives and communities.

TABLE OF CONTENTS

LIST OF FIGURES

LIST OF TABLES

ACKNOWLEDGEMENTS

My work was supported by a National Science Foundation (NSF) National Research Training Graduate Fellowship (NRT-1633631) and a National Aeronautics and Space Administration (NASA) AIST (80NSSC17K0540), which allowed me to pursue my personal research interests. This work utilized the infrastructure for high-performance and high-throughput computing, research data storage and analysis, and scientific software tool integration built, operated, and updated by the Research Cyberinfrastructure Center (RCIC) at the University of California, Irvine (UCI).

I was fortunate to have been advised throughout my PhD by Charlie Zender who was a constant advocate for my success in graduate research. Charlie has been an honest, patient, and grounding advisor. He recognizes his students as individuals and celebrates their strengths, which translates into his research group being a strong scientific team. I admire Charlie's expertise across many fields in Earth System Science and his ability to ask the right questions. I thank Charlie for emphasizing a healthy work-life balance and being tuned in with both my personal and professional goals.

I am privileged to have Sameer Singhn as one of my committee members and advisor for the Machine Learning and Physical Sciences Fellowship. Sameer has provided excellent guidance as a machine learning scientist. I am grateful for my brilliant cohort of ESS graduate students for their selfless support and encouragement as well as the present and past members of the Zender research group. Thank you to the zotCAMS board members for somehow letting me be your president. A special thank you to Tien-Yiao, the python wizard, and Zach for your support and friendship.

In addition to those at UCI, I have had several mentors during internships and research experiences that fully supported my endeavors, despite the fact that I now recognize taking me on as an undergraduate student fell more along the lines of community service: a sincere thank you especially to Mika Tosca and Mo Wozniacki. I also want to thank my co-authors including, Charlie Zender, Sameer Singh, Wenshan Wang, Melchior van Wessem, Brice Noel, and Sebastian Merinsek, who all contributed significantly to the success of my research and manuscripts.

What truly drove me forward throughout my PhD was support from my family and friends. Thank you to my friends and family for learning what a PhD is along with me. Thank you to Kris for your friendship, advice, and ability to distract, Nolan and Kylie for being loyal friends, Jon for the endless laughs and good conversation, Henry and Lola for your unconditional love, trust, and forcing me to get outside for a walk, and my parents for

teaching me independence and work ethic.

Lastly, my biggest supporter and love of my life, Hayley. Without fail, she always listened to me ramble on about my research. She has helped me to see and think differently, makes anywhere feel like home, and could not have been more supportive through this process. I am grateful for her beyond measure.

VITA

Matthew K Laffin

Ph.D. Candidate | Department of Earth System Science, University of California, Irvine
Atmospheric Science | Climate Dynamics | Polar Science | Machine Learning

---

EDUCATION

UNIVERSITY OF CALIFORNIA, IRVINE | Ph.D. in EARTH SYSTEM SCIENCE
2017-2022 | Irvine, CA, USA (GPA: 3.99/4.0)
COMMITTEE MEMBERS: Charles Zender, Eric Rignot, Sameer Singh

UNIVERSITY OF CALIFORNIA, IRVINE | M.S. in EARTH SYSTEM SCIENCE
2017-2019 | Irvine, CA, USA (GPA: 3.973/4.0)

OREGON STATE UNIVERSITY | B.S. in CLIMATE SCIENCE
2015-2017 | Corvallis, OR, USA (GPA: 3.62/4.0)
Cum Laude | Research Distinction | Advisors: Anders Carlson, Maureen (Mo) Walczak, Karen Shell

CALIFORNIA POLYTECHNIC UNIVERSITY POMONA | B.S. in BUSINESS, MINOR in FINANCE
2004-2008 | Pomona CA, USA

AWARDS AND FELLOWSHIPS

2019	2 years of stipend, fees	National Science Foundation (NSF) National Research Traineeship (NRT) Machine Learning and Physical Science (MAPS)
2018	Honorary Fellow	National Science Foundation (NSF) National Research Traineeship (NRT) Machine Learning and Physical Science (MAPS)
2017	2 years of stipend, fees	UC Irvine Graduate Fellowship
2016	1 Summer of support	NASA, Jet Propulsion Laboratory Summer Fellowship *(JPLSIP)*
2016	$6,000	Oregon State University Climate Science Scholarship

PUBLICATIONS

FIRST AUTHOR

2. **Laffin, M. K**., Zender, C. S., van Wessem, M., and Marinsek, S. (2022). The role of föhn winds in eastern Antarctic Peninsula rapid ice shelf collapse. The Cryosphere, 16(4), 1369–1381. https://doi.org/10.5194/tc-16-1369-2022

1. **Laffin, M.K.**, Zender, C., Singh, S., Van Wessem, J., Smeets, P., Reijmer, C., (2021) Climatology and Evolution of the Antarctic Peninsula Föhn Wind-induced Melt Regime from 1979-2018. *Journal of Geophysical Research: Atmospheres*, 126, e2020JD033682. https://doi.org/10.1029/2020JD033682

CO-AUTHOR

3. Morlighem, M., **Laffin, M.K.**, Neftci, E., Lee, K.M., (in press) Physics-Constrained Neural Networks for Large-Scale Inference of Subglacial Topography under Greenland and Antarctica. *The Cryosphere*.

2. Carlsen A.E., W., Beard, A.L., Hatfield, R.G., **Laffin, M.K.**, (2021) Absence of West Antarctica-sourced silt at ODP Site 1096 in the Bellingshausen Sea during the last interglaciation: support for West Antarctic ice-sheet deglaciation. *Quaternary Science Reviews., 261,* https://doi.org/10.1016/j.quascirev.2021.106939

1. Wang, W., Zender, C., Vas As, D., Fausto, R. S., **Laffin, M.K.,** (2021) Greenland surface melt dominated by solar and sensible heating. *Geophysical Research Letters*, 48, e2020GL090653. https://doi.org/10.1029/2020GL090653

PRESENTATIONS

ORAL PRESENTATIONS

4. **Laffin, M.K.**, Zender, C., Van Wessem, J., Marinsek, S., Did Föhn Winds Help Trigger the Collapses of the Larsen A and B Ice Shelves?, *AGU Fall Meeting*, December 17, 2021; New Orleans, LA [Abstract]

3. **Laffin, M.K.,** C. Zender, and S. Singh. Machine Learning Identification of Sub-grid scale Weather Events: Application to Antarctic Foehn Winds, presented at the *University of California, Irvine, Machine Learning Bootcamp*, October 19, 2019 [Bootcamp website]

2. **Laffin, M.K.,** A. Carlson, and M. Walczak. An investigation of the ACC using "mean sortable-silt" as a proxy to determine ocean current strength, presented at the *Oregon State (OSU) Paleoclimate Quaternary Tea Seminar*, June 8, 2017 [Presentation]

1. **Laffin, M.K.,** S. Bell, R. Fofrich, and M. Tosca. A global database of smoke injection heights from landscape fires: an analysis of 2009-2010, presented at the *AGU Fall Meeting*, December 15, 2016; San Francisco, CA [Abstract]

POSTER PRESENTATIONS

5. **Laffin, M.K.**, M. Morlighem, E. Neftci, K.M. Lee., Physics-Constrained Neural Networks for Large-Scale Inference of Subglacial Topography under Greenland and Antarctica, presented at the Frontiers in Machine Learning for Physical Sciences Virtual Symposium, October 26, 2020

4. **Laffin, M.K.,** Zender, Z.S., Singh, S., Van Wessem, M.K., Climatology and Evolution of the Antarctic Peninsula Föhn Wind-induced Melt Regime from 1979-2018, presented at the SCAR2020 virtual conference, August 6, 2020 [Poster]

3. **Laffin, M.K.,** Zender, Z.S., Singh, S., Van Wessem, M.K., 40 Years of Föhn Winds on the Antarctic Peninsula: Impact on Surface Melt from 1979-2018, presented at the AGU Fall Meeting, December 9, 2019; San Francisco, Ca [Poster]

2. **Laffin, M.K.,** Zender, Z.S., Singh, S. Foehn Winds on Larsen C Ice Shelf During Polar Night: Impacts on the Surface Energy Budget and Melt, presented at the AGU Fall Meeting, December 14, 2018; Washington D.C. [Poster]

1. **Laffin, M.K.,** Zender, Z.S. Using AWS and MERRA-2 data to estimate the climatology and impact of polar night foehn wind on Larsen C Ice Shelf, presented at the 13th Workshop in Antarctic Climate and Meteorology (WAMC), July 17, 2018; Madison, WI [Abstract]

TEACHING

EarthSS 138: SATELLITE REMOTE SENSING | GRADUATE INSTRUCTOR
Spring 2019 | Earth System Science Department, UC Irvine, CA, USA | Instructor Charles Zender

- 30 student upper-division course; responsible for teaching labs, holding office hours, conducting exam review sessions, reviewing course material (assignments and exams), and grading exams.
- Course provides an overview of the principles behind remote sensing, and the types of satellite data available for study of the oceans, land, and atmosphere. It requires a hands-on lab component where students process remotely sensed data in class and for final projects.

EarthSS 3: OCEANOGRAPHY | GRADUATE INSTRUCTOR
Winter 2019 | Earth System Science Department, UC Irvine, CA, USA | Instructor Julie Ferguson

- 400 student introductory course for all undergraduate majors; responsible for teaching sections, holding office hours, conducting exam review sessions, reviewing course material (assignments and exams), and grading exams.
- Course examines the circulation of the world's oceans, ocean chemistry as it relates to rivers, hydrothermal vents, atmospheric inputs, geological features, the wide variety of biological organisms, and global climate changes, such as greenhouse warming.

EarthSS 1: INTRODUCTION TO EARTH SYSTEM SCIENCE | GRADUATE INSTRUCTOR
Fall 2018/2021 | Earth System Science Department, UC Irvine, CA, USA | Instructor Dr. Ferguson

- 400 student introductory course for all undergraduate majors; responsible for teaching sections, holding office hours, conducting exam review sessions, reviewing course material (assignments and exams), and grading exams.
- Course introduces Earth System Science, which involves viewing Earth's environment in a holistic fashion. Topics covered in the course include: the origin and evolution of the Earth, its atmosphere, and oceans, from the perspective of biogeochemical cycles, energy use, and human impacts on the Earth system.

PROFESSIONAL AND ACADEMIC EXPERIENCE

Graduate Student Researcher | University of California Irvine
09/2017 - Present | Irvine, CA, USA | Advisor Dr. Charles Zender

- Explored the atmospheric/ice interaction of foehn/katabatic wind on the Antarctic and Greenland Ice sheets and their effects on ice sheet melt and ice shelf stability.
- Use A deep neural network (Machine Learning) to produce a high-resolution description of the bed topography of Greenland and Antarctica informed by surface observations and constrained by physical principles such as conservation of mass.

Undergraduate Researcher | Oregon State University
09/2016 - 06/2017 | Corvallis, OR, USA | Advisor Dr. Maureen (Mo) Walczak

- Processed ocean sediment cores for sortable silt as a proxy to determine paleocurrent strength and sea ice extent for the Southern Ocean from the late Holocene through the Pleistocene.

Summer Research Intern | NASA Jet Propulsion Laboratory (JPL)
06/2016 - 09/2016 | La Cañada Flintridge, CA, USA | Advisor Dr. Mika Tosca

- Analyzed remotely sensed smoke plume data using the MISR satellite instrument, to derive smoke injection height into the atmosphere both spatially and temporally.

Undergraduate Researcher | Oregon State University
11/2015 - 06/2016 | Corvallis, OR, USA | Advisor Dr. Andreas Schmittner

- Assessed isopycnal diffusivity interactions between model grid cells using the UVic (University of Victoria) Earth System Climate Model.

Pension Benefits Analyst | Producer Writers Guild of America
05/2012 - 01/2017 | Burbank, CA, USA

SERVICE AND OUTREACH

President | The Student Chapter of the American Meteorological Society (zotCAMS)
2019/2021 | Community and Student outreach
Presenter | Climate, Literacy, Empowerment, and iNquiry (CLEAN)
2018/2021 | Monthly Weather and Climate student outreach classes
MacArthur Fundamental Intermediate School | Santa Ana, CA
Co-Organizer/Presenter | Earth Day Earth Science Fair
05/2018 | Vista Verde Elementary School | Irvine, CA, USA

TECHNICAL SKILLS

PROGRAMMING
Python, Fortran, Unix, PyTorch

SOFTWARE/TOOLS
NCO, NCL, ArcGIS, QGIS, Google docs, JAWS

ABSTRACT OF THE DISSERTATION

The role of föhn and katabatic winds on ice sheet surface melt
by

Matthew Keith Laffin

Doctor of Philosophy in Earth System Science

University of California, Irvine, 2022

Professor Charles S. Zender, Chair

The Greenland and Antarctic ice sheets are losing mass that contributes to sea level rise. Föhn and katabatic winds (downslope winds) can enhance surface melt that can run off into the ocean directly affecting sea level rise and can destabilize ice shelves that provide a buttress force to grounded ice. Despite extensive research, melt associated with föhn or katabatic winds is still not fully understood, nor is the response of these winds and associated melt to climate change.

My dissertation examined the role of föhn and katabatic winds on surface melt on the Greenland and Antarctic ice sheets. In my first study, I examined how föhn-induced melt affects the spatial melt pattern of the Antarctic Peninsula (AP), especially south of the Larsen C ice shelf and west of the AP, what fraction of the total melt on the AP is caused by föhn winds, how melt varies through time, and how föhn-induced melt has evolved on the AP. To address these questions, I use in situ meteorological observations to train a Machine Learning algorithm to identify the föhn signature in ERA5 global reanalysis and RACMO2 regional climate model simulations. In my second paper, I used the same föhn detection

algorithm to identify the role of föhn winds in rapid ice shelf collapse. I found that föhn winds were present at the time of collapse for the Larsen A and B ice shelves which increased surface melt and pushed sea ice away from the calving front and allowed large period ocean swells to initiate collapse. In my third paper, I expand what I learned on the AP and explore the impact and trends of föhn and katabatic winds on the Greenland and Antarctic ice sheets.

The collective results of my dissertation help us understand how föhn and katabatic winds impact surface melt and ice shelf stability with the ultimate goal of understanding future sea level rise. I hope these results will help complete the climate and climate change puzzle and help alleviate the burden of future sea level rise to those who do not have the voice , power, or resources to help themselves and their communities.

CHAPTER 1

Introduction

1.1 Föhn and katabatic winds in the climate system

The Greenland (GIS) and Antarctic ice sheets (AIS) hold enough water to raise global sea levels by 65.4m (GIS-7.4m, AIS-58m) and have already contributed to 18.4mm (GIS-10.8 ± 0.9mm, AIS-7.6 ± 3.9mm) of sea level rise since 1992 (Rignot et al., 2008; Hanna et al., 2013; The IMBIE team, (2018, 2020)). Recent mass loss from the GIS has been primarily attributed to surface melt and runoff due to warmer air temperatures (Noël et al., 2014; Fettweis et al., 2017; Straneo et al., 2013) and increased isolation due to reduced summer cloud cover (Fettweis et al., 2013; Tedesco et al., 2013; Hofer et al., 2017; Noël et al., 2019). Mass loss from the AIS has been attributed to increased surface runoff and acceleration of marine-terminating glaciers primarily from regional increased air and ocean temperatures that have cause thinning, retreat, and collapse of marine-terminating glaciers and ice shelves (Rignot et al., 2004, 2014; Scambos et al., 2004; Konrad et al., 2018; Bozkurt et al., 2020, Auger et al., 2021). To understand mass loss on both ice sheets, it is important to identify all drivers of surface melt and if those drivers have changed through time.

On the margins of the GIS and AIS directionally consistent katabatic winds, and föhn winds mainly focused on the Antarctic Peninsula (AP), enhance surface melt rates (Lenaerts et al., 2017; Datta et al., 2019; Laffin et al., 2021, 2022; Wang et al., 2021). Katabatic winds originate in the cold, high, and dry ice sheet interior where relatively dense surface air drains downslope towards warmer regions. The polar highs coupled with the very cold and sloped ice sheets, make katabatic winds a consistent force on both ice sheet margins and some of the

strongest and most persistent winds on Earth (Bromwich 1988; Parish and Cassano, (2003)). Föhn winds form when relatively cool moist air, forced over a mountain barrier, releases latent heat and precipitates during ascent. The warmer, drier air descends the leeside slope and compresses to create warm and dry gusty winds (Elvidge and Renfrew (2016)). Both wind mechanisms reduce atmospheric moisture and inhibit cloud formation which increases surface insolation and heating (Vihma et al., 2011; Mioduszewski et al., 2016). The strong winds turbulently mix the stable polar boundary layer, enhance sensible heat exchange, and accelerate surface melt (Nylen et al., 2004; Vihma et al., 2011; King et al., 2017; Kuipers Munneke et al., 2018 Laffin et al., 2021; Wang et al., 2021).

The effect of föhn and katabatic winds on surface processes has been studied extensively on both the GIS and AIS, however the contribution of melt associated with föhn and katabatic winds has not been constrained. Observational and model studies have identified impacts of downslope winds on surface temperatures (Parish and Bromwich, (1986); Nylan et al., 2004), the surface energy budget (Kuipers Munneke et al., 2012, 2018, Laffin et al., 2021; Le Toumelin et al., 2021), surface mass balance including enhanced surface melt (Kuipers Munneke et al., 2012, 2018, Laffin et al., 2021), coastal precipitation (Grazioli et al., 2017), snow mass transport (Grazioli et al., 2017; Palm et al., 2017), ice shelf stability (Laffin et al., 2022), and sea ice and polynya formation with attendant impacts on ocean currents and biological productivity (Davis and McNider, (1997), Cape et al., 2014; Wenta and Cassano, 2020).

The goal of my dissertation was to better understand the contributory role of föhn and katabatic winds and associated melt on the GIS and AIS, and if melt trends have changed through time. Our understanding of ice sheet dynamics and sea level rise hinge

upon understanding every contributor to surface mass balance. Föhn and katabatic winds are prominent meteorological and climatic staples of the polar climate that contribute significantly to surface mass loss.

1.2 Organization of research

In Chapter 2, I examined how föhn-induced melt affects the spatial melt pattern of the Antarctic Peninsula (AP), especially south of the Larsen C ice shelf and west of the AP, what fraction of the total melt on the AP is caused by föhn winds, and whether melt trends and it's drivers evolved through time on the AP. To address these questions, I use in situ meteorological observations to train a Machine Learning algorithm to identify the föhn signature in ERA5 global reanalysis and RACMO2 regional climate model simulations. I found that machine learning is a useful and accurate way to identify when and where föhn winds occur on the AP. I also found that föhn winds are a significant driver of surface melt on the eastern and western ice shelves of the AP and melt trends mirror those of air temperature through time. This research provided a valuable proof of concept for the machine learning algorithm using weather stations and model simulations and help to better identify the drivers of melt on the AP. This research was published in the Journal of Geophysical Research, Atmospheres as:

"Laffin, M.K., Zender, C., Singh, S., Van Wessem, J., Smeets, P., Reijmer, C., (2021) Climatology and Evolution of the Antarctic Peninsula Föhn Wind-induced Melt Regime from 1979-2018. Journal of Geophysical Research: Atmospheres, 126, e2020JD033682. https://doi.org/10.1029/2020JD033682."

In Chapter 3, I used the same föhn detection algorithm and RACMO2 simulations to identify the contributory role of föhn winds in rapid ice shelf collapse. I found that föhn winds were present at the time of collapse for the Larsen A and B ice shelves which increased surface melt and pushed sea ice away from the calving front. The increased surface melt led to large scale surface melt ponds and hydrofracture cascades. Additionally, föhn winds on the AP pushed sea ice away from the calving front and allowed large period ocean swells to initiate collapse. I also assessed the vulnerability of the remaining ice shelves Scar inlet and Larsen C to collapse from föhn induced surface melt and found that these ice shelves are not affected in the same manner as collapsed ice shelves from föhn winds and therefore are less susceptible to collapse under our current climate. This research was published in The Cryosphere as:

"Laffin, M. K., Zender, C. S., van Wessem, M., and Marinsek, S.: The role of föhn winds in eastern Antarctic Peninsula rapid ice shelf collapse, The Cryosphere, 16, 1369–1381, https://doi.org/10.5194/tc-16-1369-2022, 2022."

In Chapter 4, I expand what I learned on the AP and use RACMO2 simulations to explore the impact, trends, and drivers of föhn and katabatic wind and associated melt on the Greenland (1961-2019) and Antarctic (1981-2019) ice sheets. I found that melt associated with downslope winds (katabatic and föhn) on the Antarctic ice sheet is decreasing while on the Greenland ice sheet melt has increased. Then I explore the wind associated melt trends which generally mirror total melt trends on each ice sheet however, on the Greenland ice sheet wind associated melt has increased less compared to total surface melt. This trend is related to a more negative summer North Atlantic Oscillation

(NAO) which forms a blocking high on the Greenland ice sheet that warms surface temperatures and decreases the wind speed of katabatic winds, ultimately decreasing wind associated melt.

The collective results of my dissertation help us understand how much melt is associated with downslope föhn and katabatic winds compared to total surface melt and how these melt regimes are changing in response to climate change. Föhn winds are prominent drivers of surface melt on the Antarctic peninsula and can negatively impact ice shelf stability. Katabatic winds help to drive surface melt on the periphery of both ice sheets; however with warming surface temperatures the negative buoyancy forces associated with katabatic flow decrease, ultimately limiting the impact of katabatic melt in a warming climate. The results of my dissertation have been shared with the collective scientific community through peer reviewed journals in the hopes that this research will help better constrained surface melt and its drivers.

CHAPTER 2

Climatology and evolution of the Antarctic Peninsula föhn wind-induced melt regime from 1979–2018

Adapted from:

Laffin, M. K., Zender, C. S., Singh, S., Van Wessem, J. M., Smeets, C. J. P. P., & Reijmer, C. H. (2021). Climatology and evolution of the Antarctic Peninsula föhn wind–induced melt regime from 1979–2018. Journal of Geophysical Research: Atmospheres, 126, e2020JD033682. https://doi.org/10.1029/2020JD033682

2.1 Introduction

Antarctic Peninsula (AP) surface melt has increased in the past half-century in response to anthropogenic increases in surface temperature (Barrand et al., 2013). Surface melt-induced firn air depletion and densification contribute to the hydrofracture process thought to have preceded the collapse of Larsen A and B ice shelves off the eastern coast of the AP in 1995 and 2002, respectively (McGrath et al., 2012; Alley et al., 2018; Kuipers Munneke et al., 2014). Ice shelves are the floating extensions of grounded glaciers and apply a buttress force that when lost, allows grounded glacier velocity to increase, and accelerates sea level rise (Rignot, 2004). Recently föhn winds have been identified as contributors to localized surface melt and hydrofracture in all seasons including polar winter at a single weather station on Larsen C ice shelf (Kuipers Munneke et al., 2018).

Föhn winds are warm and dry downslope winds that form on the lee side of mountain ranges like the AP. Elvidge & Renfrew (2016) hypothesized four mechanisms for föhn-warming: 1) Isentropic drawdown where cool moist air is blocked at low levels upwind of mountains, allowing warm dry air aloft to be brought to the surface, 2) release of latent heat from precipitation that changes the lapse rate and warms the surface, 3)

mechanical mixing of the persistent cold boundary layer with warm air aloft, 4) lee-side descending air creates clear skies enhancing radiative heating. Föhn events are highly variable within and between seasons, with the ultimate effect on surface conditions dependent on the large-scale atmospheric flow and orographic forcing (Elvidge et al., 2015). The topographic configuration of the AP (orthogonal to the westerlies) makes föhn conditions possible in all seasons, especially in spring (SON) and fall (MAM), caused by the seasonal shift in the storm track (Cape et al., 2015). Föhn-induced surface melt reduces local albedo and could increase the likelihood of hydrofracture especially near the grounding line which is thought to be a vulnerable hinge-point (Scambos et al., 2000; Lenaerts et al., 2016).

A number of studies focus on the impacts of föhn wind on melt, surface mass balance, and ice shelf stability. Case studies of specific föhn events lasting days or weeks using remote sensing, in situ observations, and airborne measurements highlight their impact on the surface energy budget, mainly focusing on the Larsen C ice shelf (LCIS) (Bozkurt et al., 2018; Elvidge et al., 2016; Cape et al., 2015; Wiesenekker et al., 2018). Regional climate model studies combined with in situ observations have deepened understanding of the spatio-temporal impacts of föhn-induced melt, and reiterate its importance in ice shelf densification and evolution (Datta et al., 2019; Turton et al., 2018; Luckman et al., 2014). Site-specific research shows that föhn-induced surface melt is predominantly limited to the northern AP (Kuipers Munneke et al., 2018; Turton et al., 2018; King et al., 2017). Most recently Elvidge et al., (2020) studied the impact of föhn on the surface energy budget, clarifying previous contradictory findings, while exploring

surface energy budget regimes on the Larsen C Ice Shelf. Föhn is well documented in summer though understudied in winter because large scale field campaigns are primarily conducted in the less harsh summer months (Elvidge et al., 2015).

Despite numerous föhn studies, questions persist regarding how föhn-induced melt affects the spatial melt pattern, especially south of the Larsen C Ice shelf and west of the AP, what fraction of the total melt on the AP is caused by föhn winds, how melt varies through time, and how föhn-induced melt has evolved on the AP. To address these questions we use a novel approach to identify föhn-induced melt events, using in situ meteorological observations to train a Machine Learning algorithm to identify the föhn signature in ERA5 global reanalysis and RACMO2 regional climate model simulations. We use these datasets to extend what we learn at weather stations both spatially and temporally. These records of föhn-induced melt occurrence, both spatial and temporally resolved, are combined with the surface energy budget which allows us to quantify melt when föhn occurs. We identify a föhn-induced melt climatology, and the annual drivers of föhn variability and evolution by assessing the correlation and seasonal variability of meteorological and energy balance variables to föhn-induced melt on the AP.

2.2 Data and Methods

2.2.1 Study Domain

The AP extends 1,300 km north from the Antarctic Continent (Figure 2.1). The AP is covered by a grounded ice sheet and supports three major ice shelves including the fourth-largest Antarctic ice shelf (Larsen C). The spine of the AP, the Antarctic Peninsular mountain range, averages only 50 km wide, and its mean elevation is 2800 m above the

surrounding ocean. This relatively thin and high mountain range is an effective barrier to the prevailing westerlies, segmenting the peninsula into an Antarctic maritime air mass to the west, and a colder continental air mass to the east. However, when the westerlies are strong and the meteorology forces air over the AP mountain range, relatively warm and dry downslope föhn winds can increase the temperature well above the freezing point (Elvidge et al., 2015). The turbulent föhn winds disrupt the polar boundary layer which allows large fluxes of sensible heat and enhanced solar radiation to reach the surface, which are partially offset by increased latent heat exchange, causing melt (Grosvenor et al., 2014; King et al., 2017).

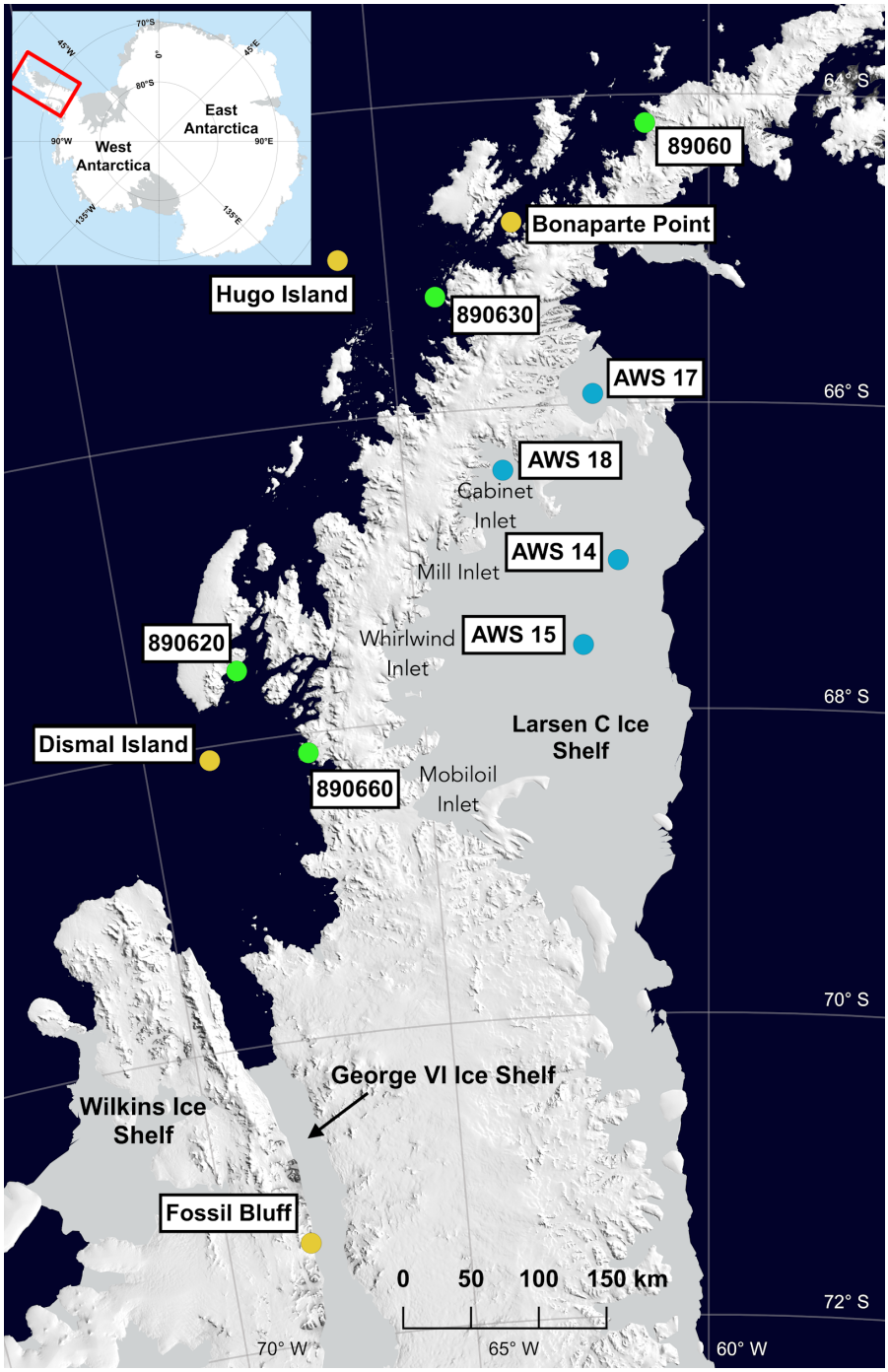

Figure 2.1. MODIS Mosaic overlay of the Antarctic Peninsula with automatic weather station (AWS) names and locations. Ice shelves are shaded grey and the ocean is shaded dark blue ("MODIS Mosaic of Antarctica 2008-2009 (MOA2009) Image Map, Version 1"). AWS color indicates the supporting network; Blue-Institute for Marine and Atmospheric Research (IMAU) at Utrecht University, Green-National Snow and Ice Data Center (NSIDC), Yellow-Antarctic Meteorological Research Center (AMRC) at the University of Wisconsin.

2.2.2 Surface Observations

We obtained in situ observations of hourly meteorological variables from 3 Automatic Weather Station (AWS) networks; the Institute for Marine and Atmospheric Research (IMAU) at Utrecht University, Antarctic Meteorological Research Center (AMRC) at the University of Wisconsin, Madison, and the National Snow and Ice Data Center (NSIDC). These data were processed through the Justified Automatic Weather Station (JAWS) software, which corrects for weather station tilt through time and harmonizes AWS data to be comparable across different networks (https://github.com/jaws/jaws). Meteorological records including wind speed (m/s), air temperature (K), and relative humidity (%) were collected by 12 AWS totaling 47 station-years on the AP (Figure 2.1 and Table 2.1). AWS observations are used as ground truth, useful to evaluate satellite observations and model simulations, and are used to train a Machine Learning (ML) algorithm to detect föhn winds in reanalysis and regional climate model simulations.

Table 2.1. Automatic Weather Station Information
IMAU is Institute for Marine and Atmospheric Research at Utrecht University, AMRC is Antarctic Meteorological Research Center at the University of Wisconsin, Madison, NSIDC is the National Snow and Ice Data Center. T = temperature, RH = relative humidity, W = wind speed, P = surface air pressure, WD = wind from direction, SW↓ = incoming short-wave radiation, SW↑ = outgoing short-wave radiation, LW↓ = incoming long-wave radiation, LW↑ = outgoing long-wave radiation

Station name	Location	Variables observed	Operation years
AWS 18 (IMAU)	66° 24' S, 63° 22' W	T, RH, W, P, WD, SW↓, SW↑, LW↓, LW↑	2015 - 2016
AWS 17 (IMAU)	65° 56' S, 61° 51' W	T, RH, W, P, WD, SW↓, SW↑, LW↓, LW↑	2011 - 2014
AWS 15 (IMAU)	67° 34' S, 62° 09' W	T, RH, W, P, WD, SW↓, SW↑, LW↓, LW↑	2009 - 2014
AWS 14 (IMAU)	67° 01' S, 61° 30' W	T, RH, W, P, WD, SW↓, SW↑, LW↓, LW↑	2009 - 2014
Bonaparte Point (AMRC)	64° 46' S, 63° 03' W	T, RH, W, P, WD	2014 - 2015
Dismal Island (AMRC)	68° 05' S, 68° 49' W	T, RH, W, P, WD	2017 - 2018
Fossil Bluff (AMRC)	71° 19' S, 68° 16' W	T, RH, W, P, WD	2009 - 2011
Hugo Island (AMRC)	64° 57' S, 65° 40' W	T, RH, W, P, WD	2009 - 2010
890600 (NSIDC)	64° 10' S, 64° 10' W	T, RH, W, P, WD	1979 - 1981
890620 (NSIDC)	67° 34' S, 68° 58' W	T, RH, W, P, WD	1988, 2001
890630 (NSIDC)	65° 15' S, 64° 16' W	T, RH, W, P, WD	1986 - 1991
890660 (NSIDC)	68° 07' S, 67° 07' W	T, RH, W, P, WD	1985 - 1997

2.2.3 Föhn Detection

We developed a Föhn Detection Algorithm (FöhnDA) that identifies föhn winds that cause melt. Our approach is similar to previous studies that employ thresholds to identify föhn conditions in hourly AWS data (Turton et al., 2018; Speirs et al., 2013; Cape et al., 2015; Datta et al., 2018; Elvidge et al., 2020), however, we are most interested in föhn-induced melt so we focus on föhns that cause the surface air temperature to rise above the freezing point. The föhn signature is quite distinct from the climatological average and is characterized by high wind speeds, low relative humidity, and increased temperatures, which makes identifying föhn events straightforward in AWS data. This signature is shared by katabatic winds, which allows FöhnDA to identify both wind types. Katabatic winds form when cold dense air drains downslope due to gravity. However, the majority of

wind-induced melt in this region is the direct result of the AP spine interacting with large scale mesocyclones leading to föhn wind.

FöhnDA identifies a föhn-induced melt event using binary classification when three measured fields surpass their empirically derived thresholds. The FöhnDA threshold for air temperature (T) is 0°C, which ensures it captures föhn events that cause surface melt. Thresholds for relative humidity (RH) and wind speed (WS) are more dynamic because high wind speeds and low relative humidity do not guarantee temperatures above freezing, they only aid to identify föhn. FöhnDA uses quantile regression to identify these variable thresholds that take into account the climatology and seasonality at each weather station site. FöhnDA uses two empirically determined thresholds: the 60th percentile wind speed and 30th percentile relative humidity. Thresholds for both wind speed and relative humidity were extensively tested to help improve classification. Varying these thresholds by 10 percent above and below the current values does not produce significantly different results because the main determinant of föhn-induced melt events is a surface temperature above freezing. A föhn melt hour (h) is identified when,

$$\text{FöhnDA}(h)=1 \quad \text{If } T>0°C,\ RH < \text{30th percentile},\ WS > \text{60th percentile}$$

Periods that meet these three criteria are classified as föhn melt events. We apply FöhnDA to all 12 AWS separately to produce the "ground-truth" training data for the ML algorithm to detect föhns that cause melt in reanalysis and climate model simulations. By applying FöhnDA separately at each AWS we obtain ground-truth data that encompass the climatic variability at each AWS site, and form a diverse training dataset.

Finally, all AWS time series were manually quality controlled before analysis. Across all the AWS time series, FöhnDA correctly classified 97% of föhn melt events, relative to manual classification. We also conducted a föhn classification sensitivity study (Table A.1) where we compare our classification results to results from methods in previous studies (Cape et al., 2015; Datta et al., 2019). Since other classification methods aim to identify all (not only melt-inducing) föhn events, we sub-sampled each method's results when temperatures were above freezing and found that FöhnDA replicated these results with less than a 5% error and with minimal false-positive and false-negative scores. We found that FöhnDA has a more sensitive wind speed criteria because the mean 60th percentile wind speed across all AWS sites is 2.85 m/s, which is exceeded during calmer föhn conditions compared to the other methods that employ higher wind speed thresholds (Datta et al, 2019 - >3.5 m/s, Cape et al., 2015 - >5 m/s).

2.2.4 Reanalysis

We used hourly meteorological data of 25 fields (Table A.3) from the European Centre for Medium-Range Weather Forecasts (ECMWF) ERA5 reanalysis (Copernicus Climate Change Service, 2017). These data are available at a horizontal resolution of about 30km or 0.28 degrees globally. ERA5 is created by assimilated satellite and in situ observations into ECMWF's Integrated Forecast System (IFS). When compared with ground-truth AWS observations on the southwestern AP and LCIS, ERA5 mean surface air temperature has a warm bias and ERA5 wind speed is underestimated though overall reproduce surface observations (Tetzner et al., 2019; Bozkurt et al., 2020).

We use sea level pressure to derive four new fields to train our ML algorithm: direction to high and low pressure, and distance to high and low pressure. These are useful to identify the preferred mesoscale flow. Two time-invariant fields, distance to steepest slope and distance to the highest elevation, serve to indicate topographic controls for föhn formation. We use an elliptical search domain with an east/west diameter of 120 km and a north/south diameter of 36 km, to determine the proximity of grid cells to local topography and slope features. This search field allows the ML algorithm to find the relationship between topographic features and föhn winds. Lastly, we create a field called ERA5 FöhnDA which uses our AWS thresholds to detect föhn conditions from ERA5 air temperature, relative humidity, and wind speed.

2.2.5 Atmospheric Model

We accessed the 3-hourly output of 19 fields from the Regional Atmospheric Climate Model 2 (RACMO2), version 2.3p2, with a horizontal resolution of 5.5km (0.05°) focused on the AP. RACMO2 uses the physics package CY33r1 of the ECMWF Integrated Forecast System (IFS) (https://www.ecmwf.int/en/elibrary/9227-part-iv-physical-processes\textit{{ECMWF-IFS, } 2008}) in combination with atmospheric dynamics of the High-Resolution Limited Area Model (HIRLAM), and is evaluated extensively with surface observations located in Dronning Maud Land and the LCIS (van Wessem et al., 2018; Bozkurt et al., 2020). When compared with AWS observations on the LCIS, surface air temperature has a slight warm bias and shortwave/longwave radiation are over/under estimated due to underestimation of clouds and moisture but overall reproduce surface observations (King et al., 2015;

Bozkurt et al., 2020). RACMO2 is forced at the lateral boundaries with ERA-Interim data (Dee et al., 2011) and shows improvement in the surface energy fluxes and near-surface temperature from previous versions compared with AWS observations (van Wessem et al., 2018). Hence RACMO2 provides self-consistent surface melt estimates independent of and intermediate in scale between ERA5 and AWS.

We created seven new fields for RACMO2 analogous to those described above for ERA5: distance to high and low pressure and direction of high and low pressure, distance to the steepest slope and highest elevation, and RACMO2 FöhnDA based on the three thresholds to identify föhn in AWS data.

To evaluate the consistency of ERA5 and RACMO2 meteorologies with in situ data, we intercompare their air temperature, relative humidity, and wind speed products with the nearest AWS observations. Pearson correlation values were calculated using each AWS and their operation years with co-located ERA5 and RACMO2 for the same years (Table A.2). Averaged over all AWSs, Pearson r values for the spatially gridded datasets (RACMO2, ERA5) are weak for relative humidity ($r = 0.31$, $r = 0.25$) largely due to how RACMO2 and ERA5 under-represent moisture and clouds (King et al., 2015). Wind speed correlation is weak for ERA5 ($r = 0.19$) and strong with RACMO2 ($r = 0.74$), likely due to the disparity in each dataset's horizontal resolution. Correlation is strong in both datasets for air temperature ($r = 0.92$, $r = 0.81$). Overall, both datasets portray spatiotemporally diffuse surface conditions relative to AWS, and thus require training to reveal the presence of localized föhn winds (Figure 2.2).

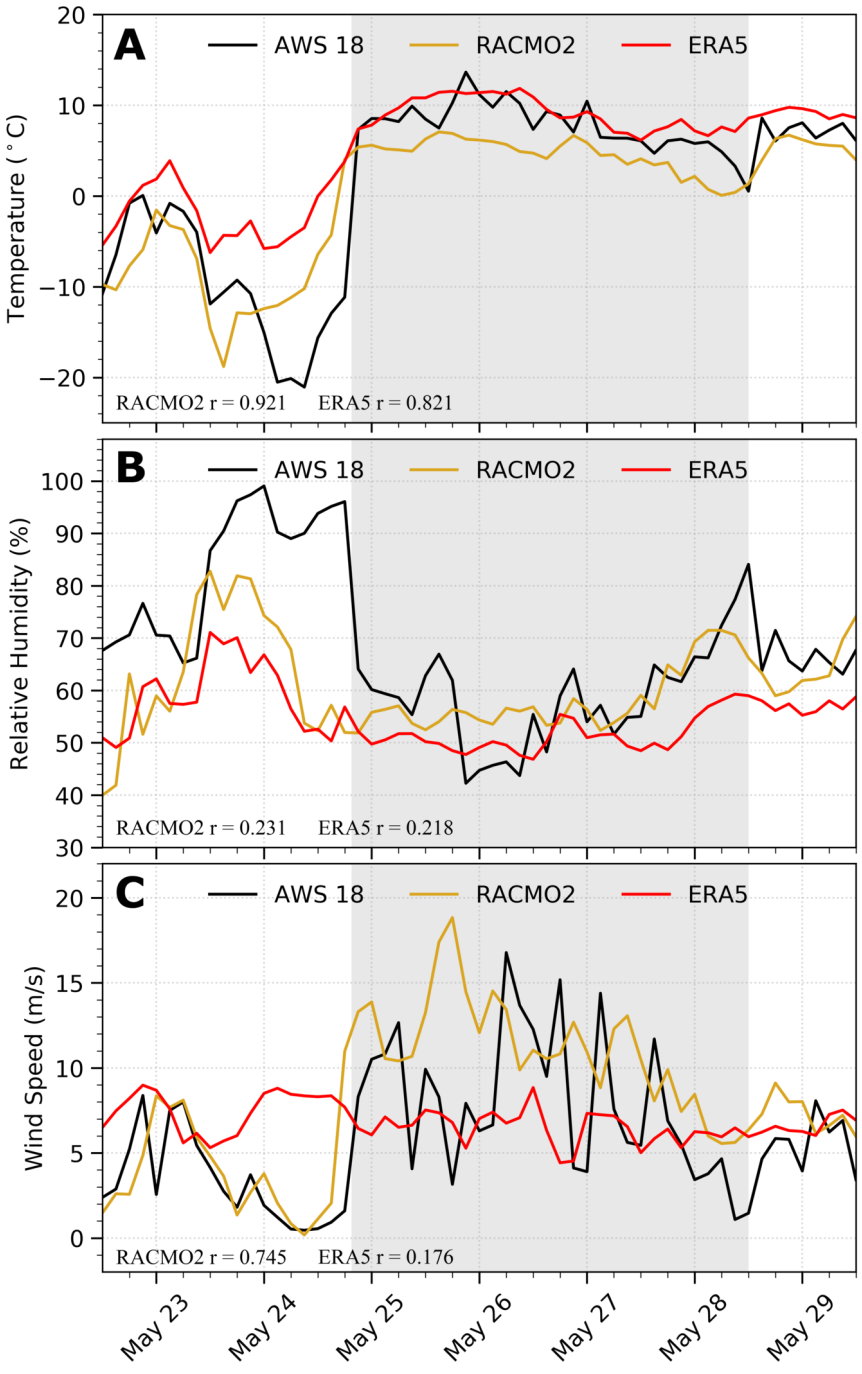

Figure 2.2. AWS 18 data with co-located ERA5 and RACMO2 hindcasts for a föhn wind event (shaded in grey) for (**A**) Air Temperature, (**B**) Relative Humidity, (**C**) Wind Speed, in late May 2016. Pearson correlation values were calculated using AWS 18 (2015-2016) with co-located ERA5 and RACMO2 for the same years.

2.2.6 Machine Learning Model Development and Selection

We first attempted to detect föhn winds that cause melt in ERA5 and RACMO2 without the use of machine learning techniques by using the FöhnDA thresholds discussed above that were tuned for AWS measurements. We call this the baseline model. However, the baseline model identifies less than 50% true positives in both datasets and produces too many false-positive and false-negative föhn classifications to be useful for either gridded dataset. The low accuracy of the baseline model stems from the coarser spatial footprint of the spatially gridded datasets compared to in situ observations, and from biases in ERA5 and RACMO2 mentioned above.

Machine Learning (ML) can largely circumvent the limitations imposed by spatial resolution because it learns from complex parameterized models and large datasets, such as ERA5 and RACMO2. Previous studies have compared expert human classification of föhn events to machine learning classification in the Alps with promising results (Mayr et al., 2018). We use Gradient Boosting Classification (GBC) machine learning because it provides simple and interpretable classification and performs well with atmospheric data (Jin et al., 2019; Sprenger et al., 2017). GBC uses decision trees as weak learners which are added in series. Each tree attempts to minimize the errors of the previous trees creating a strong classifier that provides scientific insight into which atmospheric input features are most important for identifying föhn winds with help from feature attribution techniques, discussed below. We used AWS FöhnDA results as ground-truth data to train two GBC decision tree models (ML-RACMO2 and ML-ERA5) to identify föhn winds that cause melt in ERA5 reanalysis and RACMO2.

For both models, we used 10-fold cross-validation to develop and validate decision trees using the XGBoost package in Python (Chen & Guestrin, 2016). XGBoost or "eXtreme Gradient Boosting" uses an ensemble of prediction models that are added iteratively to correct errors made by the previous model and improves model speed and accuracy while limiting resource costs. We also use the Python package Scikit-learn to identify model accuracy after it is run through XGBoost (https://scikit-learn.org/stable/about.html#citing-scikit-learn). In cross-validation, the model with the highest average accuracy score is considered the best model.

We co-locate AWS with the nearest model grid cell and use FöhnDA results to train a ML model for RACMO2 and a ML model ERA5. We use Bayesian hyperparameter optimization which aims to identify the value of each hyperparameter of a machine learning algorithm that returns the best performance when measured on a validation dataset. The Bayesian optimization approach uses the information from past trials to improve model performance and identify the optimum parameters quickly, instead of manually assigning values to hyperparameters or conducting a grid search. We use the BayesSearchCV class of scikit-optimize, a wrapper of Scikit-learn, where we assign a range of hyperparameter values to test and run the optimization until the model accuracy no longer improves. After this iterative improvement, the trained models were extrapolated across the AP domain of each dataset to create climatologies of föhn wind-induced surface melt occurrence.

2.2.6.1 Model Evaluation

We evaluated the best model according to F1-score (Van Rijsbergen 1979. The F1 score is a function of Precision and Recall, defined as,

$$Precision = \frac{TruePositive}{TruePositive+FalsePositive}$$

$$Recall = \frac{TruePositive}{TruePositive+FalseNegative}$$

$$F1 = 2 \times \frac{Precision \times Recall}{Precision+Recall}$$

Precision is defined as the number of true positives divided by the sum of true and false positives. It represents the proportion of AWS observed föhn melt events that the model predicted. Recall is defined as the number of true positives divided by the sum of true positives and false negatives. It represents the proportion of AWS-observed föhn melt events that were accurately identified by the model. The F1 statistical metric assesses model accuracy using binary classification. It takes into account both false-negative classification and false-positive classification for a range between 0 and 1. A model that correctly classifies all events with only true positive results (i.e., with no false negatives and/or false positives) yields an F1-score of 1.0. Conversely, a model that produces no true positive event classifications, and only false negative and/or false-positive results, yields an F1-score of 0.0.

A second way we evaluate model performance is to compare how well the model classification corroborates AWS-FöhnDA classified föhn events. We compared both ERA5 and RACMO2 classified föhn to 4 weather stations (AWS 14, AWS 15, AWS 17, AWS 18) on the Larsen C ice shelf which measured the majority of AWS-identified föhn events. We

divided FöhnDA-identified föhn-melt events into strong (T > 7°C), moderate(3.5°C < T < 7°C), and weak(T < 3.5°C) events based on air temperature at each AWS site. We compared each model classification to determine the percentage of each event type detected. We acknowledge that ERA5 and RACMO2 output bias, such as the ERA5 warm bias in the AP region, may theoretically lead to more strong and moderate events. However, by using surface observations to inform the ML model, we combat these model biases, because the ML model identifies what the föhn signature looks like in each dataset. Since we classify the föhn melt events using only the AWS temperature, we can directly compare how well each ML model detects these events. This diagnostic provides insight into which events are not captured by the ML models and helps estimate how much föhn-induced melt is not captured.

Last, we learn how the ML models make a prediction based on feature weights determined by Local Interpretable Model-Agnostic Explanations (LIME), a feature attribution technique (Ribeiro et al., 2016). Since ML-learned classifiers are complex, non-linear models, it is difficult to attribute a prediction to input variables. LIME provides a way to identify the importance of input variables for any black-box classifier, by performing perturbations to the inputs, observing the effect on the output, and estimating a feature importance weight for each variable in the input (the normalized importance weights sum to 1.0). To compute an overall ranking of each feature that applies to the whole dataset, we first find the feature importance for points in each of the 10 folds of the data, then aggregate the importance weights of each feature by taking their mean. LIME thus ranks the importance of input variables to provide insight into how much a model uses the given

features to make a classification, and this helps the user to combat model overfitting (Table A.3). More information about LIME can be found at (https://github.com/marcotcr/lime).

2.2.7 Surface Energy Budget and Melt

We calculate the surface energy budget as,

$$M = SW_{net} + LW_{net} + HS + HL \quad (W\ m^{-2})$$

where SW_{net} is the net of downward and upward components of shortwave radiation, LW_{net} is the net of downward and upward components of longwave radiation, and HS and HL are the turbulent fluxes of sensible and latent heat. Our sign convention is that energy fluxes directed toward the surface are positive, so positive net energy warms or melts the surface. When the surface temperature exceeds the freezing point, all excess energy is used to melt the surface. We disregard a ground heat flux as it is small compared to other fluxes (Kuipers Munneke et al., 2012). ERA5 and RACMO2 produce and archive all energy fluxes. We also calculate the surface energy budget for the IMAU AWS that have radiometric instruments and measure SWnet and LWnet, while HS and HL are calculated using the bulk aerodynamic formulas for turbulence (Kuipers Munneke et al., 2012). We compare the estimated energy budgets for AWS that provide radiation fluxes to the ERA5 and RACMO2 surface energy budget in the co-located grid cell.

2.3 Results

2.3.1 Model Accuracy and Performance

The ML models are characterized by the twelve parameters (Table A.4) that produce the most accurate summary statistics (Table 2.2). The three most influential parameters from Table A.4 are: n_estimators which is the number of decision trees used in the forest,

learning_rate which sets a learning speed so the ML models do not overfit or memorize to the training data, and max_depth which sets a maximum for the number of tree splits. More information about the other XGBoost parameters used and how to tune each can be found at (https://xgboost.readthedocs.io/en/latest/index.html).

Table 2.2. Statistics for best model for each dataset
Recall is defined as the number of true positives divided by the sum of true positives and false negatives. It represents the proportion of AWS observed föhn melt events that were accurately identified by the model. Precision is defined as the number of true positives divided by the sum of true and false positives. It represents the proportion of AWS observed föhn melt events the model predicted.

ERA5 model prediction accuracy summary	
F1-score	79.9 ± 3.48
Recall	81.2
Precision	78.6
Improvement in F1-score over baseline model	27.4
RACMO2 model prediction accuracy summary	
F1-score	81.3 ± 3.84
Recall	84.1
Precision	78.5
Improvement in F1-score over baseline model	23.1

Note. The error estimates for F1 score were obtained using one standard deviation of the 10-fold F1 score means.

Both ML models outperform the baseline model in all three accuracy metrics (Table 2.2). Despite fewer features given to the ML algorithm, ML-RACMO2 outperforms ML-ERA5. Moreover, ML-RACMO2 has 33% less training data because it is provided at a 3-hourly timescale.

Table 2.3 provides föhn-melt classification statistics of how much of the föhn-induced in situ melt is caused by strong, moderate, and weak föhn events, and how much of that melt is captured by the ML models for each dataset. Surprisingly, strong events

account for about 7% of melt caused by föhn, while weak events account for about 72% of föhn-induced melt. It is important to identify which events the models capture in order to provide model diagnostics and an accurate melt climatology. Overall the ERA5-based model classifies enough föhn events to capture 90.9% of the AWS-identified föhn melt and the RACMO2-based model captures 94.4% of AWS identified föhn melt.

Both models perform particularly well for events classified by FöhnDA as strong (T >7°C) and moderate (3.5°C < T < 7°C) (Table 2.3). ML-ERA5 correctly identifies all strong events measured by AWS, and 98.9% of the moderate events, while ML-RACMO2 correctly identifies all strong and 95.9% of medium events. Weak (T < 3.5°C) föhn events are harder to classify largely due to the more diffuse föhn-signature in the gridded models. However, ML-ERA5 classifies 87.8% of weak events and ML-RACMO2 classifies 93.5% (Table 2.3). Weak event classification skill is sensitive to AWS location. AWS 18 and 17, closer to the mountain slopes, have a higher weak event classification percentage (AWS 18 ~95%, AWS 17 ~92%), compared to AWS 15 (~74%) and AWS 14(~88%) which are farther downwind. Föhn winds are funneled through local topography that accelerates winds down mountain slopes then flow decelerates downstream from the mountains.

Table 2.3. Classification statistics for each dataset
AWS Classification of strong (T >7°C), moderate (3.5°C < T < 7°C), and weak (T < 3.5°C) averaged annually over all AWS sites. The "Föhn occurrence" column represents how often each AWS classified event occurs. The "Model classified correct" column represents the percentage of each AWS föhn classification the ML model classifies correctly. The "AWS identified föhn melt" column is how much AWS identified melt is caused by each AWS classified event. The "ML melt captured" column identifies how much of the melt identified by AWS is accounted for by the ML model.

ERA5 föhn classification					
AWS Classification	Föhn occurrence		Model classified correct	AWS identified föhn melt	ML melt captured
	ERA5 (hr)	AWS (hr)			
Strong	48 (7.1%)	48 (6.4%)	100.0%	7.1%	7.1%

Moderate	212 (31.3%)	214 (28.6%)	98.9%	20.5%	20.3%
Weak	425 (62%)	483 (64.8%)	87.8%	72.4%	63.5%
			Total föhn-induced melt captured		90.9%

RACMO2 föhn classification					
AWS Classification	Föhn occurrence		Model classified correct	AWS identified föhn melt	ML melt captured
	RACMO2 (hr)	AWS (hr)			
Strong	48 (6.9%)	48 (6.4%)	100.0%	7.1%	7.1%
Moderate	205 (29.1%)	214 (28.6%)	95.9%	20.5%	19.7%
Weak	452 (64%)	483 (64.8%)	93.5%	72.4%	67.7%
			Total föhn-induced melt captured		94.5%

To understand the basis for the ML models classification decisions we examine the feature weights provided by LIME (Table A.3). ML-ERA5's three highest weighted features are air temperature (0.174), distance to highest elevation (0.116), and 10-meter wind gust (0.062). Air temperature and 10-meter wind gust are logical indicators of the warm and windy föhn signature. Distance to highest elevation is also important for classification though may indicate some overfitting because the ML algorithm makes classification decisions based on one time step and does not take into account neighboring grid cells or location. ML-RACMO2's three highest weighted features (RACMO2 FöhnDA - 0.183, Temperature - 0.105, Relative Humidity - 0.072) include all the fields that define the föhn signature in the AWS data. Note that even though the baseline model (RACMO2 FöhnDA) does not produce high accuracy itself, it still improves the ML algorithm for classifying föhn events.

2.3.2 Surface Melt Pattern

Figure 2.3 shows the annual mean föhn-induced surface melt for ERA5 (A) and RACMO2 (B) for the period 1979-2018. Both RACMO2 and ERA5 datasets are conducive to ML use to identify the föhn signature, however, the ERA5 spatial melt pattern is inconsistent with satellite scatterometer observations of melt days and inferred melt, and misses enhanced melt in Mill, Whirlwind, and Mobiloil inlets (Bevan et al., 2018; Trusel et al., 2013). ERA5 is a global dataset that lacks the resolution to properly resolve föhn winds and therefore will not be used for further analysis of föhn wind-induced melt in this study. Below we use only RACMO2 output to analyze föhn-induced melt, which resolves a surface melt pattern more consistent with surface melt satellite observations (Figure 2.3b). The highest föhn-induced melt (52 mm w.e. yr-1) occurs east of the AP on the Larsen C and B ice shelves at the foot of the AP mountains. High localized melt is identified in Cabinet, Mill, Whirlwind, and Mobiloil inlets where föhn winds funnel through topography to form prevalent föhn jets (Elvidge et al., 2015; Elvidge et al., 2020). The inferred melt decreases eastward from the AP mountains across the LCIS as the relatively warm and dry föhn air mixes with the cold polar boundary layer which weakens the warm föhn signature. The northern portion of the LCIS experiences more melt compared to the southern portion. This is expected as the annual mean solar insolation increases equatorward. East of the AP mountains, RACMO2 indicates föhn-induced melt on the Ronne ice shelf (south of 75°S), farther south than previous research has indicated, however, melt quantity is much less than on the LCIS (Turton et al., 2018; Luckman et al., 2014; McGrath et al., 2012).

Surface melt was also inferred west of the AP on the Wilkins, Bach, and George VI ice shelves. Because föhn winds are caused by large-scale cyclonic activity it is not uncommon

to have föhn winds west of the AP spine, despite the westerly prevailing wind. The primary wind direction that leads to wind-induced melt east of the AP comes from the west where air forced over the AP mountains forms föhn winds. On the Wilkins, Bach, and George VI ice shelves, the primary wind direction is also downslope though is from the northeast/east, opposite the prevailing wind direction. This could be an indicator that melt is caused by dense katabatic wind formation, especially on George VI ice shelf where the AP mountains have a long gentle slope which can inhibit föhn formation yet enhance katabatic wind formation. However, without direct observation in these regions, it is difficult to verify the mechanism behind the melt pattern.

To better explore the cause of the spatial melt pattern we examine the spatial pattern of the contribution of the positive energy balance components (sensible heat exchange and shortwave radiation) during föhn-induced melt events (Figure 2.4a, b). We find there are two melt regimes on the AP. East of the AP, surface melt during föhn events is dominated by turbulent sensible heat exchange (66%), while shortwave radiation has a more minor role (34%). This is consistent with strong föhn influence as the prevailing wind is forced over the AP spine. We also find increased sensible heat exchange in the major LCIS inlets compared to regions not impacted by strong föhn jets, previously acknowledged by Elvidge et al., 2020. West of the AP, turbulent sensible heat exchange plays an equal role with solar heating in surface melt. Sensible heat has a more central role in melt in inlets to the north and east on the Wilkins ice shelf, consistent with a northeasterly föhn influence. Farther south on the southern George VI and Bach ice shelves föhn-induced melt is driven

more by clear skies and enhanced solar radiation common during föhn and less by turbulent exchange.

Overall, föhn-induced melt events occur 1.2% of the time spatially averaged over the AP, with increased occurrence East of the AP mountains (Figure 2.4c). Föhn-induced melt accounts for 3.1% of the total annual melt on the AP (Figure 2.4d). The föhn-induced melt percentage compared to the total annual melt is highest East of the AP spine at the base of the mountains, particularly in the major inlets of the LCIS. The average annual föhn-induced melt on LCIS is 3.7% of the total annual melt, however, at locations close to the AP mountains, such as at AWS 18, annual föhn-induced melt percent can reach as high as 17.7%. Even though föhn-induced melt only occurs 5.7% of the time in Cabinet inlet, that represents an average of 16.9% of the total annual melt highlighting the melting power of the föhn mechanism.

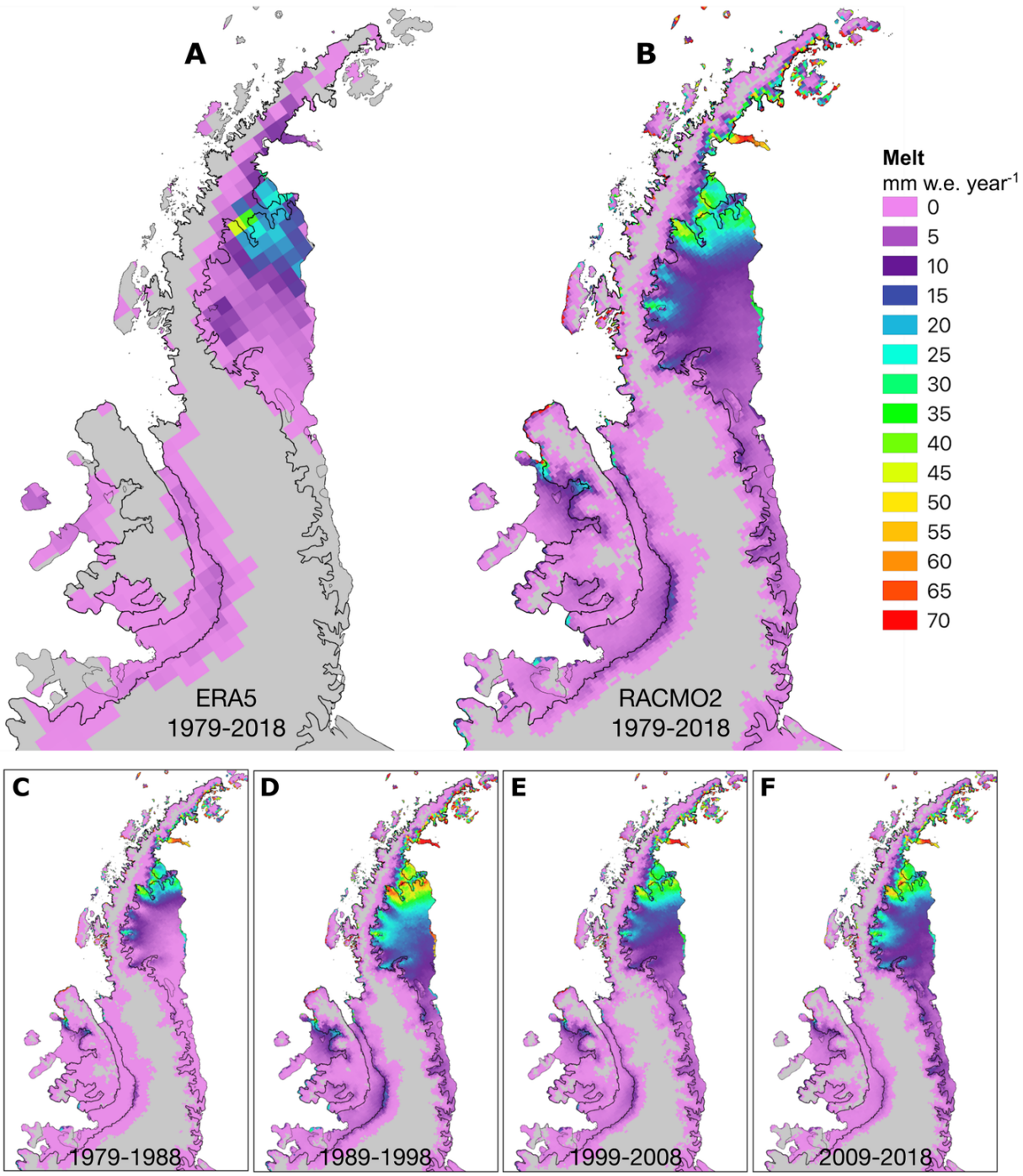

Figure 2.3. ERA5 (**A**) and RACMO2 (**B**) föhn-induced spatial melt patterns averaged from 1979-2018. RACMO2 decadal föhn-induced spatial melt pattern averaged from (**C**) 1979-1988, (**D**) 1989-1998, (**E**) 1999-2008, (**F**) 2009-2018. The thick black line indicates the grounding line from the Antarctic Surface Accumulation and Ice Discharge (ASAID) project (Bindschadler et al., 2011).

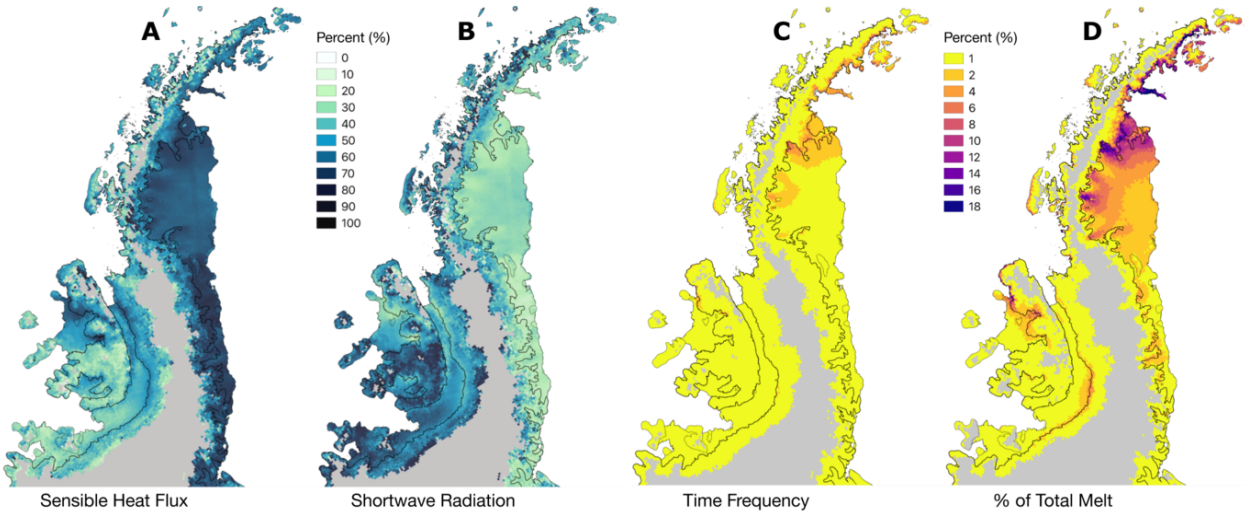

Figure 2.4. Map of the Sensible heat flux (**A**) and Shortwave radiation (**B**) components percent contribution of the positive energy balance during föhn-induced melt events from 1979-2018. (**C**) Map of the annual mean percent of time föhn-induced melt occurs per year from 1979-2018. (**D**) Map of the mean percent of total melt concurrent with föhn winds annually from 1979-2018.

2.3.3 Temporal Variability and Evolution

We find the annual mean föhn-induced melt on the AP is 3.9 Gt yr-1 (Figure 2.5), about 3.1% of total annual-mean AP melt estimated by RACMO2. Annual föhn-induced melt is variable ranging from 2 Gt yr-1 in 1980 to 6.9 Gt yr-1 in 1995 (Figure 2.5a). Föhn-induced melt appears to increase through time (12% increase from 1979-2018) although the trend is not significant at the 95% level of confidence ($p = 0.48$). A significant positive trend was identified for the period 1979-1998, where föhn-induced melt increased at 0.1 Gt y-1, however, this trend stabilized after 1998. These trends can be attributed to the rise in AP surface temperature from 1979-1998, and the decline/stabilization in AP surface temperature from 1998-present (Turner et al., 2016).

There is a clear seasonal cycle for inferred föhn-induced melt consistent with the non-föhn melt season (Figure 2.5b, c). Föhn-induced melt is highest in the summer months (DJF) when surface temperatures and shortwave radiation peak, and lowest in the winter months (JJA). Summer föhn melt constitutes 53.89% of annual föhn-induced melt on the AP. Spring and Fall surface melt contribute less (Spring (SON) 18.98%, Fall (MAM) 22.7%), while winter still experiences surface melt though much less (4.43%) than other seasons. Föhn-induced melt occurrence peaks in fall (MAM) (Figure 2.7a), however, the majority of föhn-induced AP surface melt occurs in summer.

Compared to the Wilkes and George VI ice shelves, LCIS contributes the most föhn-induced melt (69%) to the AP annual total, largely due to its size, low latitude, and eastern position downwind of the AP mountain range compared to other ice shelves. Wilkins and George VI ice shelves constitute much smaller portions of the total inferred AP föhn-induced melt, 3.6% and 3.7%, respectively. Föhn-induced melt has decreased with time on the Wilkes and George VI ice shelves (Figure 2.3c, d, e, f). While these trends are not significant they are consistent with the larger cooling trend in the southwestern AP attributed to changes in sea ice extent and strengthening of the southern jet (Turner et al., 2016; Van Wessem et al., 2015).

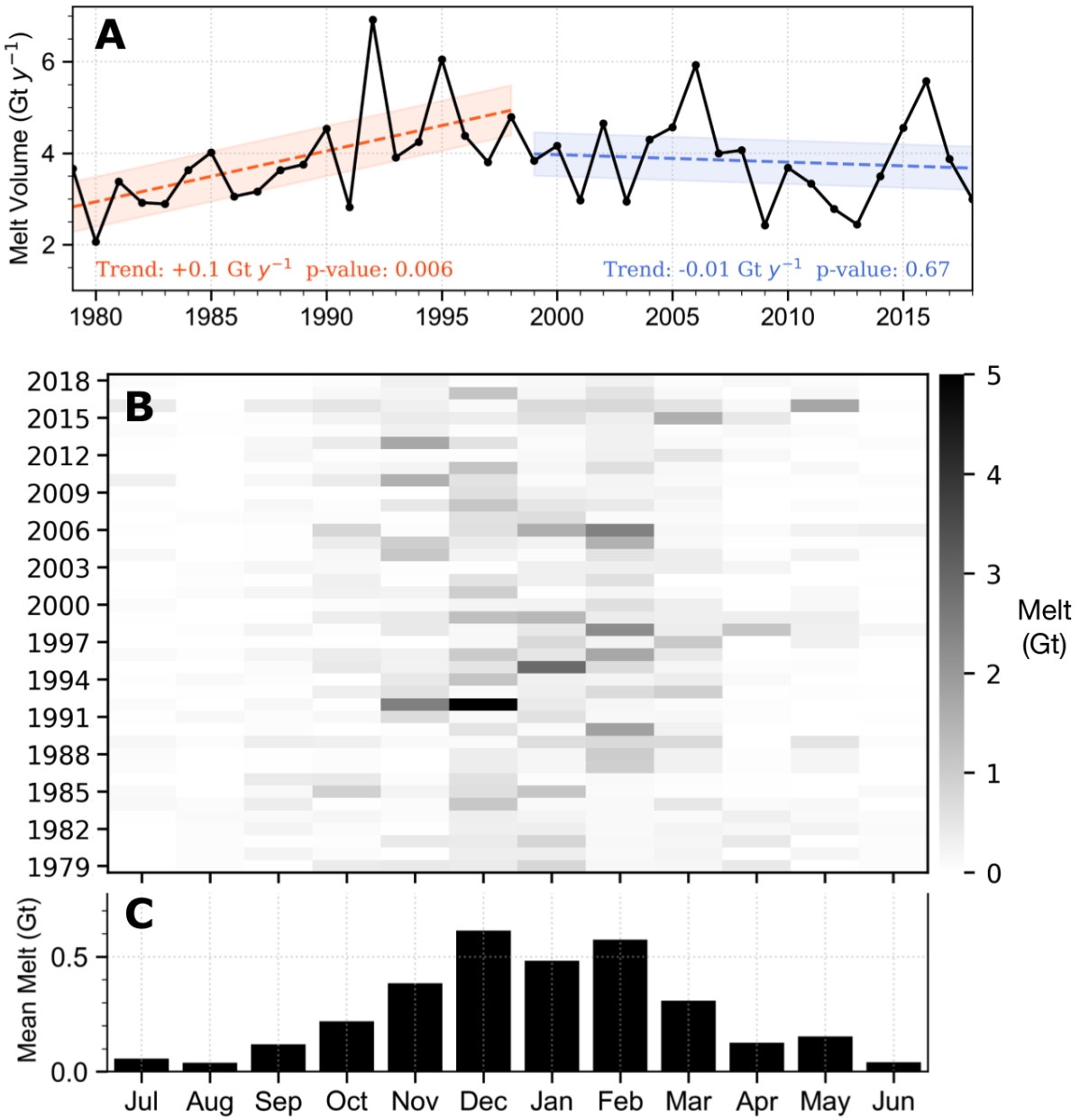

Figure 2.5. (**A**) Annual föhn-induced meltwater volume. The dashed lines indicate the linear trends for the corresponding time, with the 95% confidence limits for the trends indicated by the shaded regions. (**B**) RACMO2 monthly meltwater production concurrent with föhn over the AP. (**C**) Mean monthly (1979-2018) meltwater volume concurrent with föhn winds.

2.3.4 Föhn-induced Melt Regime Evolution

Figure 2.6 shows the energy balance components, föhn occurrence, and meteorological variables related to the annual variability of föhn-induced melt events from 1979-2018. Each of the graphs in Figure 2.6 compares the föhn variable to the time series of föhn-induced surface melt, with the variable trend in color and the correlation (r) and significance level (p-value) shown. Each variable is important when trying to understand the drivers of föhn-induced melt variability through time.

Unsurprisingly, föhn-induced surface melt annual variability is most closely correlated to föhn occurrence, since föhns must be present in order to produce föhn-induced melt (Figure 2.6a). This is in contrast to hourly drivers of surface melt where strong sensible heat exchange and enhanced shortwave radiation drive melt, particularly in LCIS inlets (Elvidge et al., 2020). Descending föhn winds mix the stable polar boundary layer causing clear skies and increased surface temperatures. Despite this föhn mechanism driving melt, sensible heat exchange does not drive the annual variability in föhn-induced melt on the AP. Variability in the strength of the sensible heat flux has no real correlation to föhn-induced surface melt (Figure 2.6f). However, solar radiation, enhanced by the föhn mechanism, has a moderate correlation to föhn-induced melt, which is not unexpected because most melt in this region is driven by shortwave radiation (Figure 2.6b). Föhn occurrence or the number of hours föhn wind occurs AP-wide has a strong positive correlation to surface melt, implying melt variability is not driven by the strength of the föhn wind, but how much time föhn occurs (Figure 2.6a). This point is further illustrated by the moderate correlation of föhn-induced melt to air temperature and small air

temperature variability during föhn, suggesting that föhn strength/temperature response does not change significantly through time and does not explain annual melt variability (Figure 2.6c).

Trends in föhn drivers indicate föhn has evolved through time. We find a long-term reduction in wind speed during föhn-induced melt events, which directly affects sensible and latent heat exchange (Figure 2.6d). We also see increases in shortwave radiation which are larger than the solar output variability. These trends suggest there may be sub-annual or seasonal changes through time that lead to changes in annual mean values. To better understand these seasonal changes we compared the monthly average of the first 20 years (1979-1998) to the second 20 years (1999-2018) (Figure 2.7). We attribute the föhn-induced melt evolution through time to a shift in seasonal föhn occurrence. We find föhn occurrence or the number of hours the AP experiences föhn-induced melt events exhibits a seasonal cycle that has changed through time. Figure 2.7 shows the seasonal distribution of föhn occurrence. Föhn-induced melt occurrence has a bimodal distribution and peaks during the spring and fall when the storm track shifts poleward/equatorward (Figure 2.7a). Figure 2.7b shows the monthly difference in föhn occurrence between the first 20 years (1979-1998) and the second 20 years (1999-2018). We identify large decreases in föhn occurrence in July (-34%), September (-40%), March (-13%), and April (-20%) and increased föhn occurrence in October (+21%), November (+11%), and December (+25%).

Seasonal changes in föhn-induced melt occurrence drive the change in föhn-induced melt regime on the AP. Figures 2.7c, d, e, and f show the seasonal variability in daily melt

rate (C), wind speed (D), sensible heat exchange (E), and shortwave radiation (F) during föhn-induced melt events. Föhn-induced melt rate has a similar seasonal pattern compared to solar radiation, with a high melt rate correlated with high solar radiation. Föhn winds are strongest in the winter when vertical temperature gradients are largest due to the consistent strong polar boundary layer inversion. Since sensible heat exchange is proportional to wind speed, we see increased sensible heat exchange during winter, when föhn winds are strongest. When we compare these seasonal patterns with seasonal changes in föhn occurrence we get a clear picture of the changing AP föhn-induced melt regime. The AP experiences less föhn-induced melt events in the months when solar radiation and melt rate are low and wind speed and sensible heat exchange are high. Conversely, more melt events occur when solar radiation and melt rate is high, and when wind speed and sensible heat exchange are low. These seasonal föhn occurrence changes affect the annual mean of föhn drivers and lead to the annual trends shown in Figure 2.6.

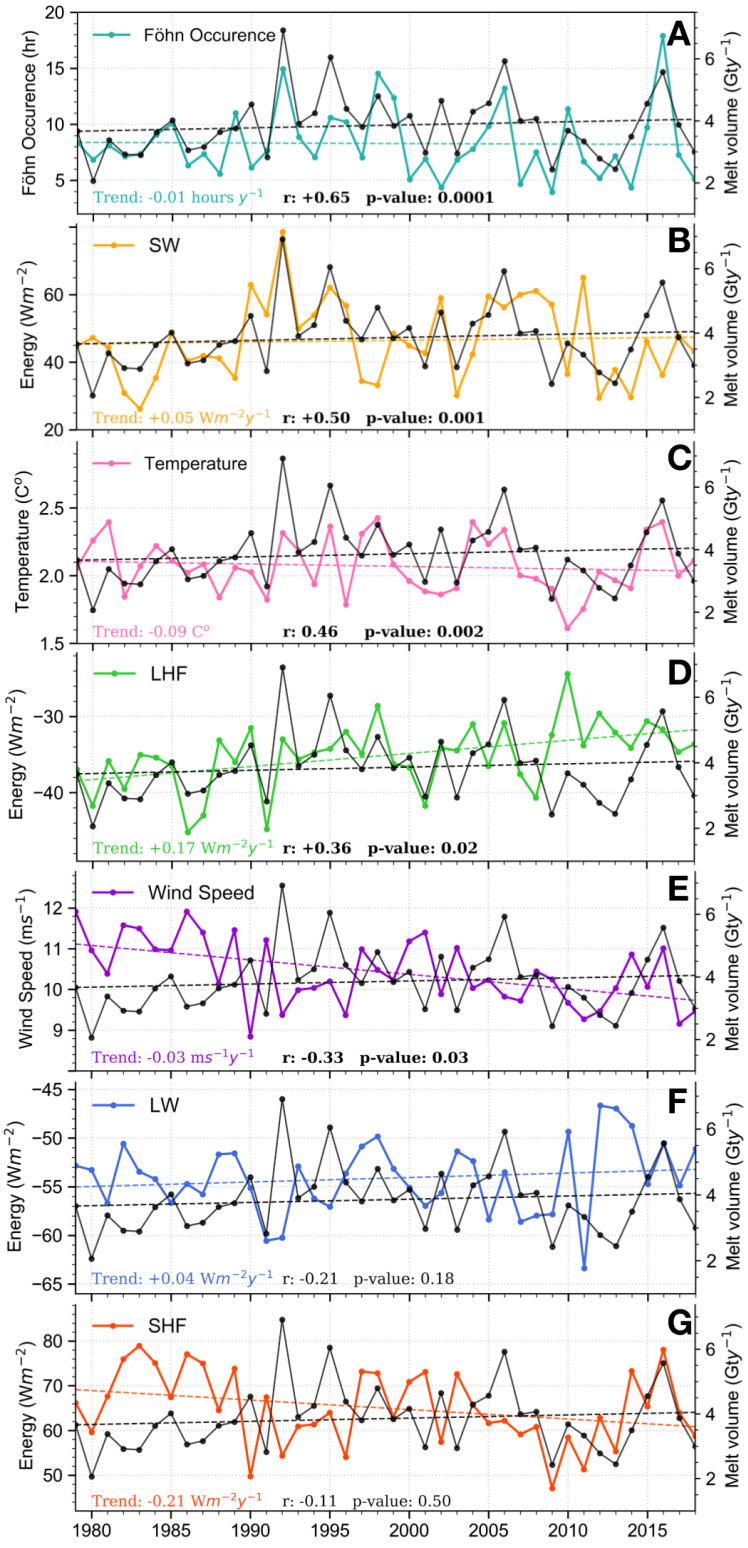

Figure 2.6. Time series of annual föhn-induced melt (right axis, black line) compared to: (**A**) föhn-induced melt occurrence, (**B**) shortwave radiation (SW), (**C**) air temperature, (**D**)

latent heat flux (LHF), (**E**) wind speed, (**F**) longwave radiation (LW), (**G**) sensible heat flux (SHF). Dashed lines in each panel represent the linear trend. R values show the correlation between melt and the corresponding variable and were calculated using the Pearson correlation. P-values were considered significant at the 95% significance level (< 0.05). Bold r and p-values are statistically significant.

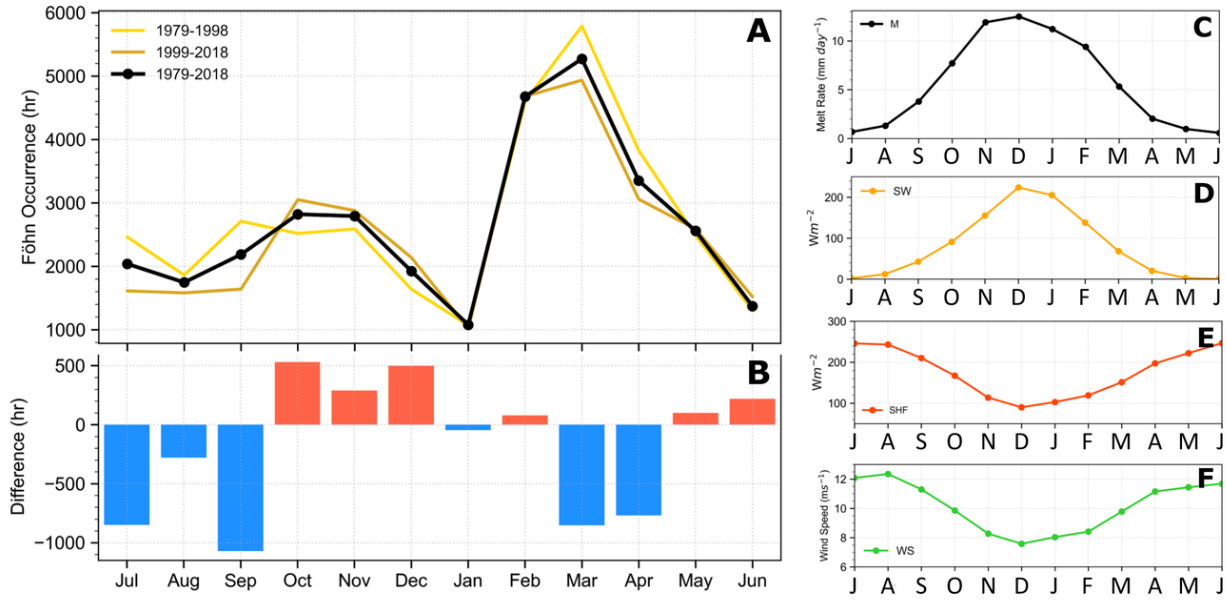

Figure 2.7. (**A**) Monthly föhn-induced melt occurrence averaged over the AP. (**B**) Monthly difference in föhn-induced melt occurrence between the first 20 years (1979-1998) and the last twenty years (1999-2018). (**C**) Monthly föhn-induced melt rate (M). (**D**) Monthly shortwave radiation (SW) during föhn melt events. (**E**) Monthly sensible heat flux (SHF) during föhn melt events. (**F**) Monthly average wind speed (WS) during föhn melt events.

2.4 Discussion

We extracted the föhn-induced surface melt climatology for the AP from 1979 to 2018, using a novel machine learning method to identify the föhn signature in both regional climate model simulations and in satellite-based reanalyses. Building on many other studies that use variable thresholds to identify föhn, we have added the additional step of using thresholds on AWS surface observations to inform a ML model what the föhn signature looks like in these datasets. Both RACMO2 and ERA5 datasets are amenable to machine learning. It is important to note that ERA5 does not resolve föhn winds, as these

winds are small scale (5-20 km), especially in regions with föhn jets like Cabinet, Mill, Whirlwind, and to some extent Mobil Oil inlets (Elvidge et al., 2015). However, when we use ML informed by AWS observations, the model detects the combined changes in meteorological variables that indicate föhn presence. This means that to some extent, ERA5 represents föhn winds on the overall sense with warm, dry, and windy conditions that occur over the entire region when föhn occurs. In other words, when wind is moving from west to east, for example, over the AP mountains, the LCIS region at large will likely experience an increase in temperature, reduction in relative humidity, and increase in wind speed, which is identified by the ML algorithm, even though ERA5 does not explicitly resolve föhn events.

Our model performance was consistent with previous studies in identifying the föhn-induced melt spatial pattern and meltwater volume in RACMO2 model output (Kuipers Munneke et al., 2018; Datta et al., 2019). Although Datta et al., (2019) surface meltwater volume is slightly larger than our study (4.1 Gt yr-1 vs 3.9 Gt yr-1), this can be attributed to regional climate model differences, specifically grid-cell spatial resolution (Datta et al., 2019 7.5km vs. This study at 5.5km). Additionally, our estimates of polar night föhn induced melt agree with Kuipers Munneke et al., 2018 at AWS 18 (~23% of total melt), however, our melt volume at AWS 18 is higher (+15.2%) than RACMO2, likely due to model physics and resolution.

Our investigation into the drivers of long-term (annual) föhn-induced melt variability points to föhn-occurrence (total number of hours of föhn) and enhanced shortwave radiation as the primary drivers of melt. What is surprising is that sensible heat

exchange has the weakest correlation to annual föhn-induced melt variability. This result contrasts with short-term (hourly) drivers of melt, when sensible heat is the main driver especially when shortwave radiation is limited (Kuipers Munneke et al., 2018; Elvidge et al., 2020). Locally, the influence of föhn and subsequent strength of the sensible heat exchange is primarily a function of how close a location is to the AP mountains and whether a föhn jet is present. If a location is between föhn jets or farther east on the LCIS, the sensible heat signature is less pronounced owing to a stronger shortwave radiation (cloud-clearing effect) influence (Elvidge et al., 2020). Because of this relationship, when all föhn-induced melt events are averaged annually on the AP, shortwave radiation and föhn-occurrence become the primary drivers of melt variability. Although, more research is still needed in regards to how effectively föhn winds reduce cloudiness and whether models over-represent the cloud-clearing effect and under-represent moisture during föhn (King et al., 2015; Elvidge et al., 2020).

We show that the föhn-induced melt regime has changed through time and attribute it to seasonal changes in föhn occurrence. The seasonal change in föhn occurrence may be driven by a more positive Southern Annular Mode (SAM) or Antarctic Oscillation, the defining mode of climatic variability in the AP region. A positive SAM index represents a constriction of the westerly winds toward Antarctica. Most notably the austral spring (SON) and summer (DJF) SAM index has become more positive, which shifts the storm track southward over the AP which may cause more föhn events to occur in the region (Lubin et al., 2008). Reduced föhn occurrence in the period 1999-2018 in winter and fall is more difficult to attribute yet seems to be caused by decreased surface temperature trends

identified on the AP (Turner et al., 2016). This means that there may be the same number of föhn events, though the föhn events that cause surface temperature to increase above freezing and lead to melt have decreased.

2.5 Conclusions

We identify föhn-induced melt events over the AP from 1979-2018 by using AWS surface observations to train two machine learning (ML) models to detect the föhn signature in RACMO2 and ERA5 datasets. Our ML algorithms, trained by AWS observations, performed well compared to manual classification and previous study methods. The surface melt pattern for both datasets conforms to previous work using satellite scatterometry data and model output, although ERA5 lacks the spatial resolution to resolve melt in fine-scale AP inlets such as Mill and Mobiloil. We have identified new föhn-induced melt on the Wilkes, Bach, and George VI ice shelves, consistent with eastward föhn or katabatic winds. Föhn wind-induced melt accounts for 3.1% of the total melt on the AP and can be as high at 18% close to the mountains where the winds funnel through mountain canyons to form föhn jets. Föhn-induced surface melt does not significantly increase from 1979-2018, despite a more positive Southern Annular Mode, however, a significant increase and subsequent decrease/stabilization occurred from 1979-1998 and 1999-2018, consistent with the AP warming and cooling trends during the same time periods. Föhn-induced melt occurrence and enhanced shortwave radiation drive annual variability in melt, suggesting föhn occurrence and the cloud-clearing effect of downslope wind are more important than föhn strength. We also find that the seasonality of föhn-induced melt events has evolved, driven by changes in seasonal föhn occurrence, with increased

occurrence in summer, and decreased occurrence in fall, winter, and early spring. While surface temperature trends on the AP have been attributed to natural variability, changes in the SAM which affects föhn-induced surface melt occurrence, have been attributed to anthropogenic causes. This highlights the importance of further monitoring of the föhn-induced melt drivers, trends, and variability.

Acknowledgments

MKL was supported by the National Science Foundation (NRT-1633631) and NASA AIST (80NSSC17K0540). CSZ gratefully acknowledges support from the DOE BER ESM and SciDAC programs (DE-SC0019278, LLNL-B639667, LANL-520117). JMVW acknowledges support by PROTECT and was partly funded by the NWO (Netherlands Organisation for Scientific Research) VENI grant VI.Veni.192.083. We thank the Institute for Marine and Atmospheric Research (IMAU) at Utrecht University, the Antarctic Meteorological Research Center (AMRC) at the University of Wisconsin-Madison, and National Snow and Ice Data Center (NSIDC) for providing Automatic Weather Station data. We thank the European Centre for Medium-Range Weather Forecasts (ECMWF) for providing ERA5 reanalysis data and the Institute for Marine and Atmospheric research Utrecht (IMAU) for providing RACMO2 output. We also thank the reviewers, whose suggestions greatly improved the manuscript. ERA5 reanalysis data are freely available through the European Centre for Medium-Range Weather Forecasts (https://www.ecmwf.int/en/forecasts/datasets/reanalysis-datasets/era5). RACMO2 model data are available by request at https://www.projects.science.uu.nl/iceclimate/models/antarctica.php, however, a subset

(2001-2018) of the data are hosted online at https://zenodo.org/record/3677642#.X-pXAFNKjUI. IMAU AWS data are available at https://www.projects.science.uu.nl/iceclimate/aws/publications.php. Antarctic Meteorological Research Center (AMRC) AWS data are available at http://amrc.ssec.wisc.edu/aws/api/form.html. NSIDC AWS data are available at https://nsidc.org/data/nsidc-0190. The authors declare no conflict of interest.

CHAPTER 3

The role of föhn winds in Antarctic Peninsula rapid ice shelf collapse

Adapted from:

Laffin, M. K., Zender, C. S., Singh, S., Van Wessem, J. M., Smeets, C. J. P. P., & Reijmer, C. H. (2021). Climatology and evolution of the Antarctic Peninsula föhn wind–induced melt regime from 1979–2018. Journal of Geophysical Research: Atmospheres, 126, e2020JD033682. https://doi.org/10.1029/2020JD033682

3.1 Introduction

Ice shelves, the floating extensions of grounded glaciers, subdue the discharge of grounded ice into the global ocean (Rignot et al., 2004; Scambos et al., 2004; Gudmundsson et al., 2013; Borstad et al., 2016). Re-examination of past ice shelf collapse events can help to shed light on the mechanisms of collapse and improve the understanding of ice shelf dynamics for future projections of sea-level rise (Rignot et al., 2004; Gudmundsson et al., 2013; Borstad et al., 2016). The final collapses of the Larsen A (LAIS) in 1995 and the Larsen B (LBIS) ice shelves in 2002 have been attributed to decreased structural integrity brought on by a combination of factors. Most notably, regional atmospheric warming (Scambos et al., 2000; Mulvaney et al., 2012), extended melt seasons (Scambos et al., 2003), multi-year firn pore space depletion (Kuipers Munneke et al., 2014; Trusel et al., 2015), melt pond flooding (Glasser and Scambos (2008); Trusel et al., 2013; Leeson et al., 2020), crevasse expansion through hydrofracture (Scambos et al., 2003; Banwell et al., 2013; Pollard et al., 2015; Alley et al., 2018; Banwell et al., 2019; Robel and Banwell, 2019), glacier structural discontinuities (Glasser et al., 2008), basal melt (Pritchard et al., 2012; Rignot et al., 2013; Depoorter et al., 2013; Schodlok et al., 2016; Adusumilli et al., 2018), warm

melt-water intrusion (Braun et al., 2009), melting of the ice melange within rifts conducive to rift propagation (Larour et al., 2021), and regional sea ice loss allowing ocean swell flexure stress on the calving front (Banwell et al., 2017; Massom et al., 2018).

While the list of mechanisms that can destabilize ice shelves is extensive, a conceptual model for rapid ice shelf collapse proposed by Massom et al., (2018) identifies 4 essential prerequisites for sudden collapse: (1) extensive surface flooding and hydrofracture; (2) reduced sea ice or fast ice at the ice shelf front; (3) outer margin or terminus fracturing and rifting; and (4) initial calving trigger at the ice shelf margin. They theorize waves led to calving front damage and small calving events that breached the “compressive arch'' of stability of both ice shelves proposed by Doake et al., (1998). At the same time the ice shelves were covered in extensive surface melt lakes that were unlikely to drain horizontally because of the relatively flat surface (Banwell et al., 2014). Satellite observations and ice shelf stability model studies determined the LBIS was covered with >2750 melt lakes that were on average 1 meter deep before collapse (Glasser and Scambos (2008); Banwell et al., 2013). Ice shelves inundated with surface melt lakes are susceptible to disintegration through a process known as hydrofracture, where meltwater applies outward and downward pressure to the walls and tip of crevasses that can propagate through the ice shelf (Scambos et al., 2003; Banwell et al., 2013; Bell et al., 2018; Lhermitte et al., 2020). Furthermore, melt lakes that rapidly drain by hydrofracture can create fracture patterns that split ice shelves into sections with aspect ratios that support unstable rollover, and hydrofracture cascades that begin when melt lakes drain and/or calving occurs at the ice shelf terminus (Scambos et al., 2003; Banwell et al., 2013; Burton et al., 2013; Robel and

Banwell, 2019). The combination of ocean swell stress on the calving front and extensive melt ponds led to large-scale hydrofracture cascades that proposed by Massome et al., (2018) ultimately caused the rapid collapse of the LBIS and possibly the LAIS.

In addition to a lack of sea ice and extensive melt ponds, meteorological and satellite observations identify clear skies and warm west/northwest föhn wind at the time of collapse (Figure 3.1c-f) (Rott et al., 1998; Rack and Rott (2004); Cape et al., 2015; Massom et al., 2018). Föhn winds form when relatively cool moist air is forced over a mountain barrier, often leading to precipitation on the windward side of the barrier that dries the air mass (Grosvenor et al., 2014; Elvidge et al., 2015). As the now drier air descends the leeward slope it warms adiabatically and promotes melt directly through sensible heat exchange, and indirectly by the associated clear skies that allow additional shortwave radiation to reach the surface in non-winter months (Turton et al., 2017, 2018; Kuipers Munneke et al., 2018; Elvidge et al., 2020; Laffin et al., 2021). Föhn winds and their capacity to cause surface melt have been studied extensively on the AP. Observations and model studies on the LCIS confirm the föhn mechanism that enhances sensible heat and shortwave radiation and alters local albedo which can increase surface melt rates upwards of 50% compared to non-föhn conditions (Cape et al., 2015; Elvidge et al., 2015; King et al., 2015, 2017; Kuipers Munneke et al., 2012, 2018; Bevan et al., 2017; Lenaerts et al., 2017; Datta et al., 2019; Kirchgaessner, et al., 2021; Laffin et al., 2021, Wang et al., 2021). Late season föhn melt reduces firn pore space, and thus pre-conditions ice shelves to form melt ponds and are responsible for the increased firn density pattern east of the AP mountains on the LCIS (Holland et al., 2011; Kuipers Munneke et al., 2014; Datta et al., 2019). Föhn

melt climatology studies have aimed to identify how much melt is caused by föhn and the locations most affected and found föhn winds account for up to 17 % of melt and are concentrated in the LCIS inlets (Turton et al., 2017; Datta et al., 2019; Laffin et al., 2021). Pressure gradient differences across the AP range lead to föhn winds that funnel through mountain gaps as highly concentrated föhn jets, particularly in inlets east of the AP range (Luckman et al., 2014; Elvidge et al., 2015; Kuipers Munneke et al., 2012; Grosvenor et al., 2014). In addition to enhancing surface melt rates, föhn winds exert force on sea/fast ice and drag it away from the calving front, thereby exposing the front to ocean waves (Bozkurt et al., 2018). Climatic studies of the Larsen B embayment indicate that föhn winds were coincident with collapse (Rack and Rott (2004); Leeson et al., 2017). However, it is unknown if concentrated föhn jets spilled onto the former LAIS and LBIS and, if so, whether those föhn winds contributed to their collapse. The questions, therefore, arise: 1) To what extent did föhn-induced melt contribute to the surface melt budget on each eastern AP ice shelf?; 2) Did föhn winds and associated melt play a role in triggering the collapses of the LAIS and LBIS?; 3) What are the implications of föhn-induced melt for the remaining eastern AP ice shelves?

To address these questions we consider three metrics: Section 3.1 explores the total annual surface melt quantity induced by föhn winds and how melt is spatially distributed across each ice shelf; Section 3.2 identifies the coincidence of föhn-induced melt preceding and during the collapse events, and the estimated melt-lake depth in response to melt events.; Section 3.3 identifies the contribution of föhn melt to the climatological surface liquid water budget comparing collapsed and extant ice shelves on the eastern AP. By

constructing a timeline of melt and melt mechanisms and comparing melt metrics with collapsed and extant ice shelves, we can identify the contributory factors to collapse.

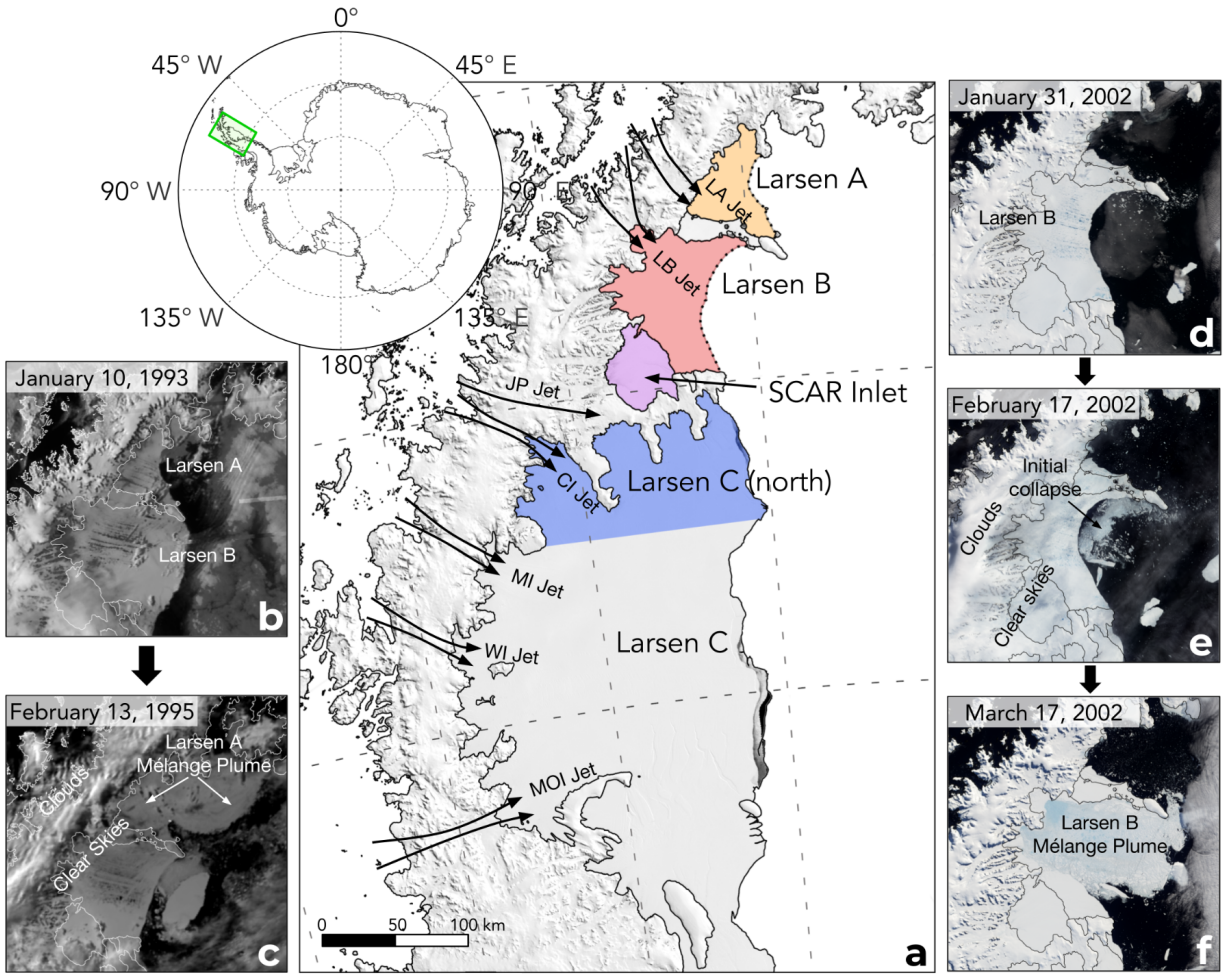

Figure 3.1. Map of the northern Antarctic Peninsula (**a**) showing locations of collapsed ice shelves (LAIS-January 25, 1995, LBIS-February 9, 2002), extant ice shelves (SCAR inlet and LCIS), and föhn jets (Larsen A jet (LA jet), Larsen B jet (LB jet), Jason Peninsula jet (JP jet), Cabinet inlet jet (CI jet), Mill inlet jet (MI jet), Whirlwind inlet jet (WI jet), Mobil Oil inlet jet (MOI jet)) with a MODIS Mosaic overlay. The colored regions indicate how this study separates ice shelves for climatic analysis. The dotted lines show the former extent of the Larsen A and Larsen B ice shelves at the time of collapse. Panels (**b**)-(**f**) are satellite images of the collapses of the LAIS and LBIS. (**b**) AVHRR (Advanced Very High-Resolution Radiometer) image of the northern AP two years before the collapse of the LAIS showing melt lakes on the surface of both ice shelves. (**c**) AVHRR image after the collapse of the LAIS. (**d**) NASA provided MODIS (Moderate Resolution Imaging Spectroradiometer) image showing the LBIS days before collapse began. (**e**) MODIS image showing a föhn wind event (clouds over the western AP, clear skies over the ice shelves) along with the initial collapse of the LBIS. (**f**) MODIS image of the complete collapse of the LBIS.

3.2 Data and methods

3.2.1 Regional Climate Model 2 Simulation (RACMO2)

We base our analysis on 3-hourly output from simulations by the Regional Atmospheric Climate Model 2 (RACMO2), version 2.3p2, with a horizontal resolution of 5.5km (0.05°) focused on the AP from 1979-2018. RACMO2 uses the physics package CY33r1 of the ECMWF Integrated Forecast System (IFS) (https://www.ecmwf.int/en/elibrary/9227-part-iv-physical-processes\textit{{ECMWF-IFS, } 2008}) in combination with atmospheric dynamics of the High-Resolution Limited Area Model (HIRLAM). When RACMO2 surface simulations are compared with AWS observations on the LCIS, surface air temperature has a slight warm bias likely because of model resolution and shortwave/longwave radiation are over/under estimated due to underestimation of clouds and moisture but overall reproduce surface observations (King et al., 2015; Leeson et al., 2017; Bozkurt et al., 2020; Laffin et al., 2021) .

3.2.2 Föhn wind detection

We use the Föhn Detection Algorithm (FöhnDA) that identifies föhn winds that cause melt using 12 Automatic Weather Stations (AWS) on the AP previously developed and detailed in Laffin et al., (2021). FöhnDA identifies föhn-induced melt events using binary classification Machine Learning when 10 meter air temperature (T) is greater than 0°C, which ensures it captures föhn events that cause surface melt. Thresholds for relative humidity (RH) and wind speed (WS) are more dynamic because high wind speeds and low relative humidity do not guarantee temperatures above freezing, they only aid to identify föhn. FöhnDA uses quantile regression to identify these variable thresholds that take into account the

climatology and seasonality at each AWS site. FöhnDA uses two empirically determined thresholds: the 60th percentile wind speed and 30th percentile relative humidity which are 2.85 m/s and 79% averaged at all AWS locations. We co-locate AWS with the nearest model grid cell and use FöhnDA results to train a ML model that detects föhn winds in RACMO2 output. Our ML model improves the accuracy of föhn detection by over 23% when compared to the simple binary classification method applied to RACMO2 output as described above. A sensitivity study detailed in Laffin et al., (2021) compares previous föhn detection methods (Cape et al., 2015; Datta et al., 2019) and shows that FöhnDA allows us to use in situ observations from AWS and expand föhn detection with RACMO2 output to regions and times when AWS observations are not available (Figure B.1) (Table B.1).

Föhn jet locations were identified using wind direction and strength during föhn events (Figure 3.2a) and by the surface melt pattern during föhn (Figure 3.3b). The RACMO2 topography pixel size is 5.5 km which is sufficient to produce the föhn jets identified on the LCIS (Elvidge et al., 2015), and allows for new föhn jet identification on the LAIS and LBIS despite lack of direct observation. However, föhn winds funneled through local canyons and mountain gaps smaller than 5.5 km are not directly simulated. Therefore, we consider RACMO2 simulated estimates of surface melt caused by föhn winds to be conservative and likely greater in regions where föhn winds are funneled and concentrated.

3.2.3 Ice shelf intercomparison analysis

We split the ice shelves into areas shown in Figure 3.1a (Larsen A, Larsen B, SCAR inlet, Larsen C (north), and Larsen C) and take the average of all model grid cells annually to create a climatology of surface melt, melt rate, melt hours, surface temperature. We use a

two-tailed t-test statistic to identify if the mean surface temperature and mean surface melt of both ice shelves are statistically different from one another at the 95% confidence interval. We compare all ice shelves to the LBIS because it was the most recent collapse event and is adjacent to collapsed and existing ice shelves. Qualitatively similar results are obtained when comparing all ice shelves to the LAIS.

To compare ice shelf liquid water budgets we use a liquid-to-solid ratio (LSR) as a crude proxy for available firn air content and can be estimated as,

$$LSR = \frac{Total\ liquid\ water\ (snowmelt + liquid\ precipitation)}{Total\ solid\ precipitation\ (snow)} \quad (3.1)$$

where areas with LSR < 1 represent an ice shelf that receives more solid precipitation than liquid water and is therefore less likely to saturate with liquid water and form melt lakes than areas with LSR > 1.

3.2.4 Sea ice concentration analysis

We used 3-hourly meteorological data of sea ice concentration from the European Center for Medium-Range Weather Forecasts (ECMWF) ERA5 reanalysis (Copernicus Climate Change Service, 2017). These data are available at a horizontal resolution of about 30 km or 0.28°. ERA5 is created by assimilated satellite and in situ observations into ECMWF's Integrated Forecast System (IFS). We compare sea ice concentration to the occurrence of föhn wind events to identify how föhn winds impact sea ice concentration. We measure the mean sea ice concentration of the ocean 90km directly east of each ice shelf (Larsen A, Larsen B, and Larsen C) in the Weddell Sea. We explore the relationship of summer föhn

wind occurrence and summer (DJF) sea ice concentration using a statistical pearson correlation method. When föhn winds are present we compare the mean of all sea ice concentration pixels in the designated ice shelf region for all years from 1979 to 2018.

3.3 Results

3.3.1 Föhn jets and melt

Using RACMO2 historical simulations, informed by a Machine Learning algorithm (FöhnDA) that is trained with AWS observations (Laffin et al., 2021), we identify seven recurring föhn jets or "gap winds" that lead to high surface melt rates on the eastern AP ice shelves (Figure 3.2a). Four of these jets (CI, MI, WI, MOI) have been studied using airborne observations and model simulations (Grosvenor et al., 2014; Elvidge et al., 2015). The remaining three jets (LA, LB, and JP) are, to our knowledge, identified here for the first time. Overall, winds from the west and northwest direction lead to increased surface melt rates that can be up to 53% higher than melt when the wind is from other directions (Figure 3.2c) (van den Broeke (2005)). Additionally, the degree to which föhn winds impact surface melt on each ice shelf varies depending on föhn jet existence, location, and wind strength (Wiesenekker et al., 2018). These variations in föhn jet location may provide insight into why SCAR inlet and the LCIS remain intact while the LAIS and LBIS have collapsed other than the significant difference in annual surface temperature (Cook and Vaughan (2009); Bozkurt et al., 2020; Carrasco et al., 2021).

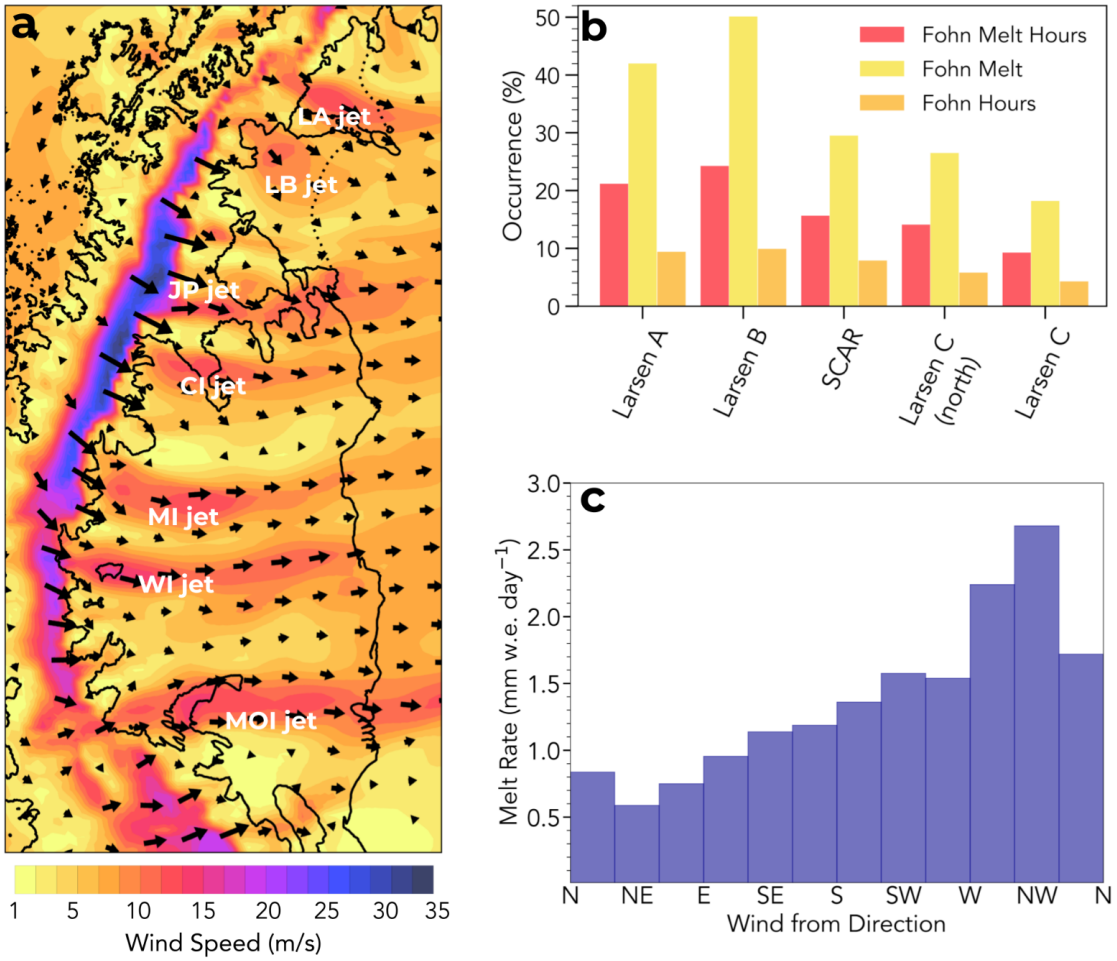

Figure 3.2. (**a**) The northern AP showing the RACMO2-simulated wind speed and direction vectors on January 24, 1995, just before the collapse of the LAIS. Föhn jet locations are indicated with names. (**b**) RACMO2 annual average föhn melt hour percent of total melt hours, föhn melt percent of total melt for each ice shelf from, and percent of total hours föhn winds occur from 1980-2002. (**c**) RACMO2 melt rate as a function of wind direction averaged for all ice shelf regions on the AP from 1980-2002.

Surface melt production is more pronounced under the influence of föhn jets, particularly for the LA and LB jets which produce 35.7% and 31.8% more melt respectively compared to regions not in the path of a föhn jet on each ice shelf (Figure 3.3). Föhn-induced surface melt accounts for 42% of the total annual melt between 1979 and 2002 on the LAIS and 51% of total melt on the LBIS but only represents 21% and 25% of total melt hours on the LAIS and LBIS (Figure 3.2b, 3.3c). In locations directly influenced by

föhn jets, the mean annual föhn-induced melt was as high as 61% on the LAIS and 57% on the LBIS of total annual melt. By contrast, föhn-induced melt accounts for only 25% of 1979-2002 total melt on SCAR inlet and 17% on the LCIS. SCAR inlet is not directly impacted by a föhn jet, but still experiences clear skies and weak föhn influence from the overall descending air during föhn events. The LCIS is affected by numerous föhn jets (CI, MI, WI, MOI), accounting for up to 40% of the total annual melt in Cabinet and Whirlwind inlets, decreasing with distance east of the AP mountains. The stark contrast in surface melt amount and fraction caused by föhn winds on collapsed vs. intact ice shelves implicates föhn melt as a contributor to the LAIS and LBIS collapses. A clearer picture of the role of föhns emerges after we examine föhn-induced melt extent and timing.

The spatial distribution and extent of surface melt influence ice shelf stability. Surface melt and melt lakes near the ice shelf terminus can lead to calving front collapse and structural instability for the remaining portion of the ice shelf (Depoorter et al.,2013; Pollard et al., 2015). Consistent with this mechanism, the LA and LB föhn jets impact a large spatial area of the LAIS and LBIS, and reach the ice shelf calving fronts (Figure 3.3b). SCAR Inlet lacks a strong föhn jet/influence and does not regularly experience large-scale melt lakes even during high melt years (Figure 3.1b-f). This helps explain why SCAR Inlet is still intact, despite decreased sea ice buttress force and major structural changes observed after the collapse of the LBIS (Borstad et al., 2016; Qiao et al., 2020). LCIS on the other hand is impacted by four major jets and regularly experiences föhn-induced melt lakes, particularly in Cabinet inlet. However, the vast size of the LCIS limits the amount of föhn-induced melt at the terminus. The föhn melt mechanism breaks down by mixing with cold air which

reduces the intensity of the föhn jets from their peak at the base of the AP mountains to the calving front (Figure 3.3b) (Elvidge et al., 2016; Turton et al., 2018). Having established that föhn winds significantly enhanced surface melt overall (Cape et al., 2015; Elvidge et al., 2015; Datta et al., 2019) and at the crucial calving front of LAIS and LBIS, we now examine the timing of föhn-induced melt events relative to collapse.

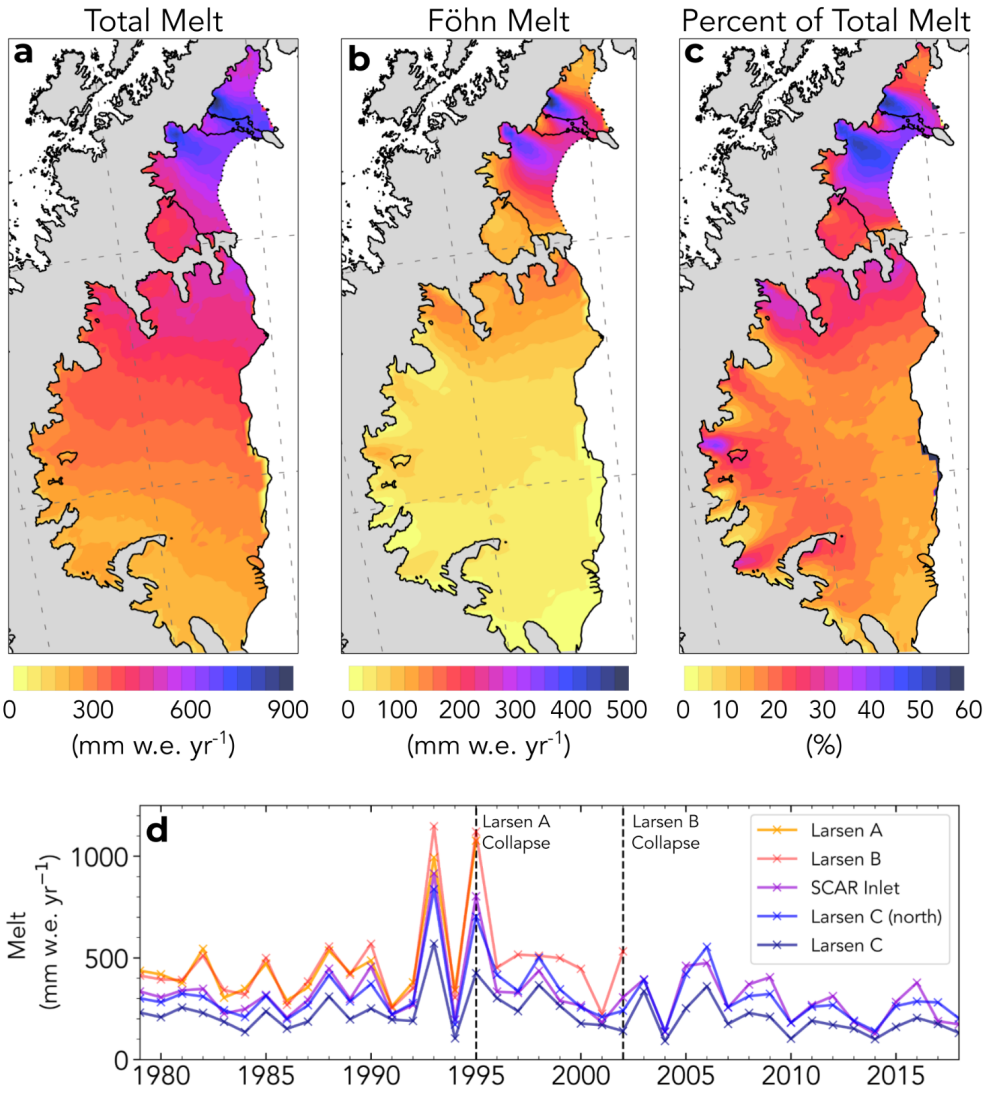

Figure 3.3. (**a**) RACMO2 average annual melt from 1980-2002. (**b**) RACMO2 average annual föhn wind-induced melt from 1980-2002. (**c**) RACMO2 percent of total melt concurrent with föhn wind from 1980-2002. (**d**) RACMO2 time series of the mean annual surface melt on each ice shelf from 1979-2018. Dashed vertical lines indicate the year in which each ice shelf collapsed. Note: The Larsen B graph often overlaps the Larsen A curve.

3.3.2 Coincidence of föhn winds with collapse

3.3.2.1 LAIS

Three föhn wind events occurred on LAIS between January 18 and 27, 1995, overlapping with the initial phase of the LAIS collapse that began on January 25 (Figure 3.4b) (Rott et al., 1998). These föhn events helped contribute to the collapse of the ice shelf in two ways: (1) Enhanced surface melt rates caused by the LA jet led to extensive melt lakes across the ice shelf that possibly promoted large-scale hydrofracture cascades because of the rapid (days to weeks) nature of collapse (Banwell et al., 2013); (2) The west/northwest wind direction actively pushed or melted sea ice and fast ice away from the calving front, allowing ocean waves to reach the ice shelf terminus (Rott et al., 1996; Massom et al., 2018). The föhn wind events prior to and during collapse lasted an average of 3 days each and produced increased surface melt greater than any other 9-day period from 1979-2018, with mean cumulative melt of 268.5 mm w.e. or 25.2% of the total annual melt in the 1994/95 melt season. Total melt during the 1994/95 melt season was 127% higher than an average year (474 mm w.e./yr) and the 9-day föhn wind event produced 57% of the total melt of an average melt year. Therefore this 9-day föhn-induced melt event and melt year are clearly anomalous in the observational record. We also identify a negative correlation between the occurrence of föhn winds and sea ice concentration on all eastern AP ice shelves (Figure 3.5a), that is more correlated with föhn wind occurrence than air temperature (Figure 3.5b). When föhn winds occur on the AP, sea ice concentration decreases which is consistent with other wind types in Antarctica (katabatic winds) that form perennial wintertime polynya (Figure 3.5c-e)(Bromwich, 1984; Bozkurt et al., 2018;

Wang et al., 2021). At the start of the 9-day föhn event, sea ice concentration east of the LAIS was at or near 100% but by the time collapse began, sea ice concentration dropped significantly (Figure 3.5d-e).

We next examine the contribution of föhn-generated melt to other observables implicated in the collapse, namely surface liquid water, melt lake depth, and melt lake extent (Scambos et al., 2003). We estimate the spatial extent and depth of melt lakes prior to collapse on the LAIS using satellite images of melt lake surface area combined with model-simulated available liquid water volume. The cumulative spatial melt pattern between January 18 and 27, 1995 identifies significant melt on the LAIS ranging from 157-356 mm w.e. (Figure B.2a), varying spatially with the influence of the LA jet. Satellite imagery of the LAIS during the collapse in progress show melt lakes were present (Figure B.3) however because the collapse had already begun, it is likely many of the lakes had drained or had been altered so estimating melt lake extent is not possible. However, Advanced Very High-Resolution Radiometer (AVHRR) imagery on December 8, 1992, provides high-resolution cloudless images of the ice shelf taken at the end of a similar föhn-induced melt event during a year when melt was comparable to the 1994/95 melt season, therefore we consider this melt lake extent analogous to the 1994/95 melt season (Figure 3.4a). We find the melt lake surface area was likely between 5.1%-10.8% (103 km2 - 219 km2) of the total LAIS surface area (Figure B.2b). Melt lake surface area is likely underestimated because the image was taken early in the 1992/93 melt season and does not easily identify small lakes or river systems. Liquid water pooling on the ice surface is modulated by the local topography. If we assume all the available surface liquid water

during the 9-day melt period, minus evaporation, runoff, and refreeze, forms lakes that cover the same estimated surface area as the 1992/93 melt season, we can estimate melt lake depth during the initial collapse. We find mean melt lake depth to be between 1.38-6.86 meters depending on lake location and föhn influence, which exceeds the average lake depth of the LBIS lakes prior to collapse (1m) (Banwell et al., 2014) and the modeled lake depth (5m) that could lead to large-scale hydrofracture cascades, especially under the influence of the LA jet (Banwell et al., 2013).

3.3.2.2 LBIS

A föhn wind event coincided with the initial LBIS collapse on February 9, 2002, with two events just prior to collapse and three additional events before complete collapse by March 17, 2002 (Figure 3.4c). Föhn events in the LBIS 2001/02 melt season were relatively short, averaging less than 24 hours per event, and produced melt rates 27% higher than non-föhn melt that year and 39% of the average föhn melt rate in all other years (Figure 3.4e). Similar to the LAIS collapse the off-coast wind direction and enhanced surface melt rates during the föhn wind event helped push sea ice away from the calving front and contributed to surface melt lakes that led to hydrofracture and collapse (Figure 3.5a) (Massom et al., 2018). Additionally, previous high melt rate föhn events such as those in the 1992/93 and 1994/95 melt seasons likely preconditioned the LBIS through firn densification to support melt lake formation, discussed in section 3.3.

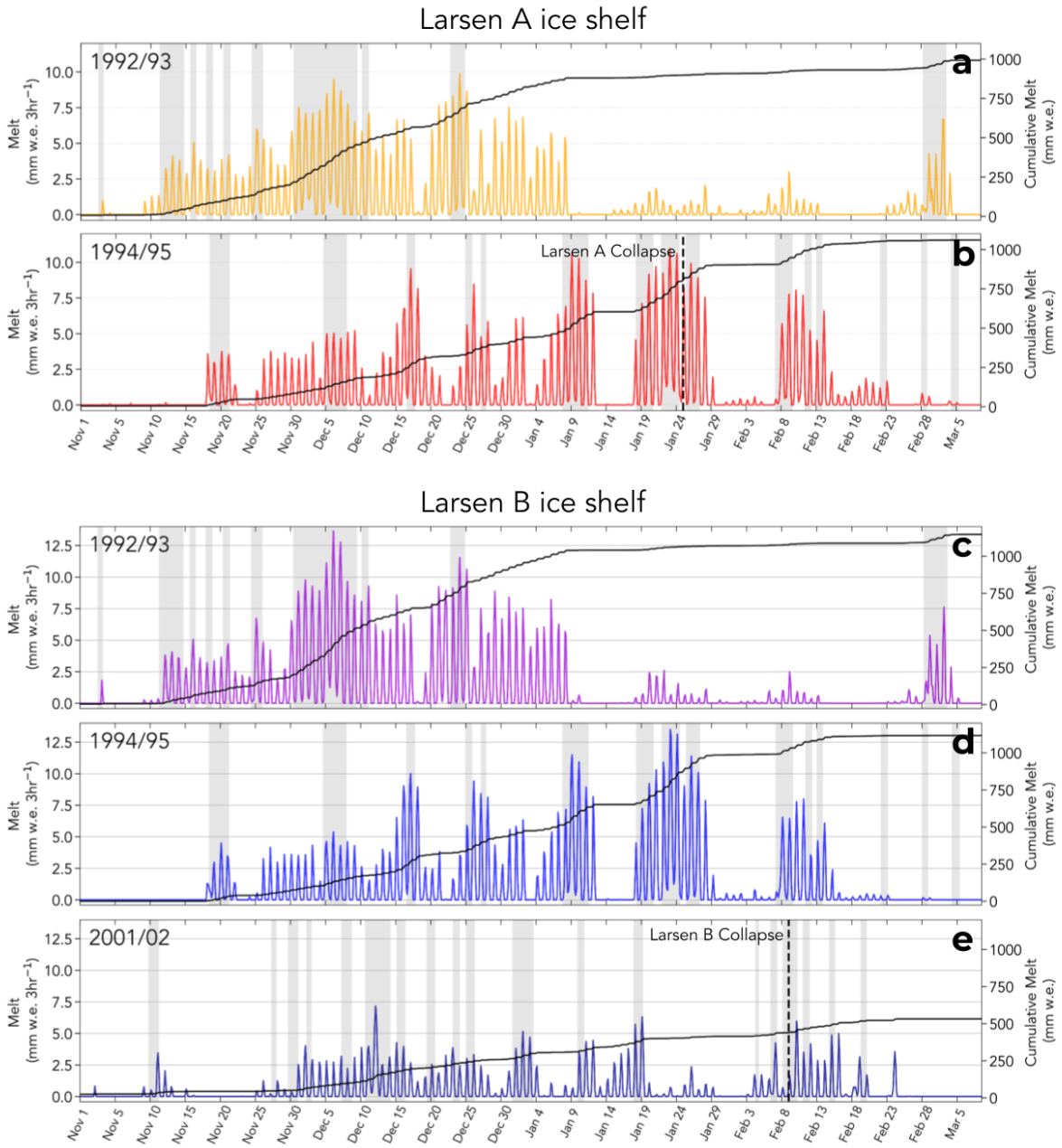

Figure 3.4. RACMO2 time series of surface melt production and cumulative melt during the Antarctic melt season averaged over the indicated ice shelf. Grey shading indicates the presence of föhn winds. (**a**) 1992/1993 LAIS. (**b**) 1994/1995 LAIS. (**c**) 1992/1993 LBIS. (**d**) 1994/1995 LBIS. (**e**) 2001/2002 LBIS. Note: Surface melt that occurs after the collapse events indicated by the dashed vertical lines in (**b**) and (**e**) are estimates of melt quantity if the ice shelves did not disintegrate.

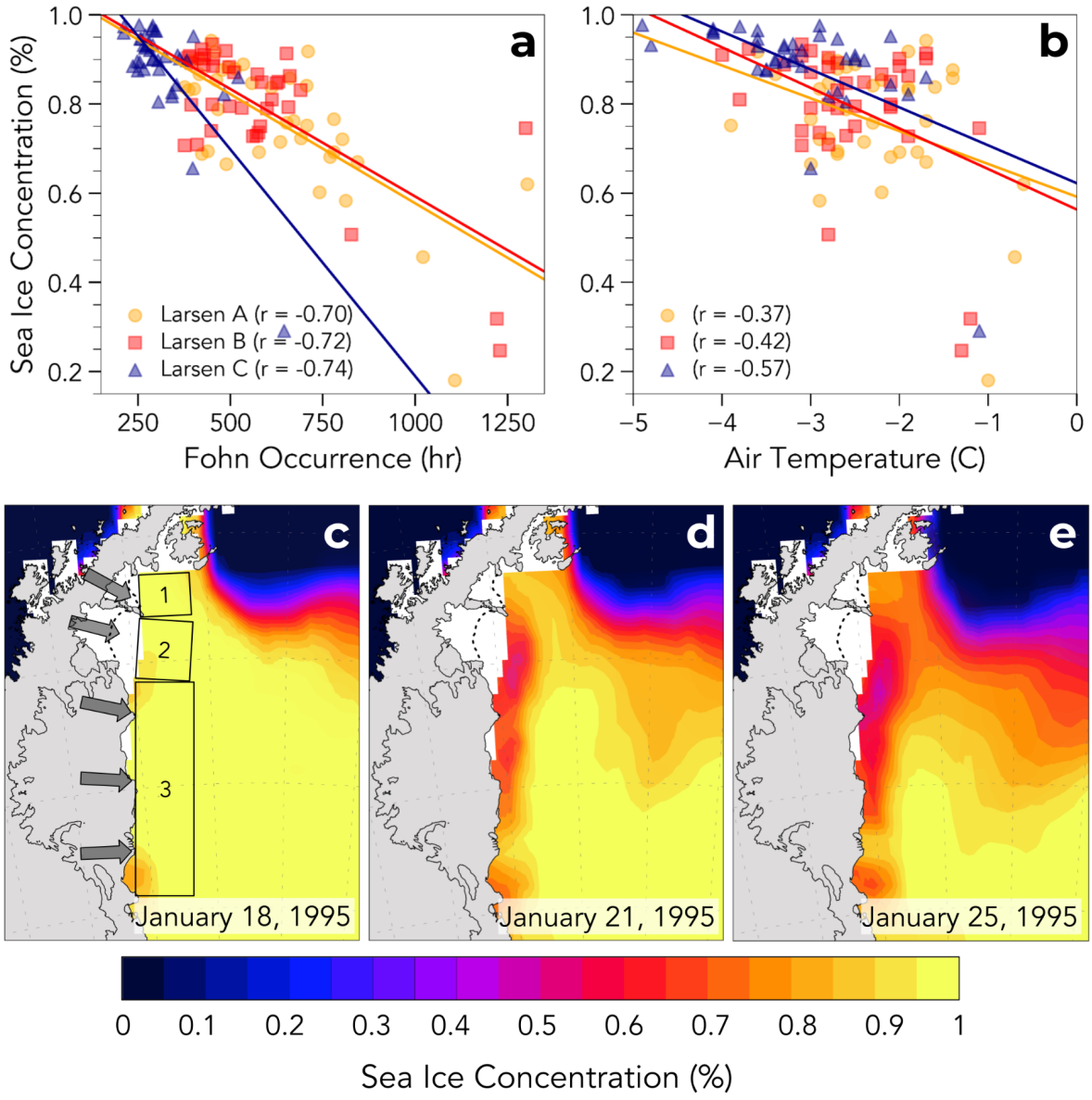

Figure 3.5. (**a**) Scatter plot of ERA5 summer (DJF) sea ice concentration and RACMO2 identified föhn occurrence hours on each ice shelf from 1979-2018. (**b**) Scatter plot of ERA5 summer (DJF) sea ice concentration and RACMO2 mean summer air temperature on each ice shelf from 1979-2018. ERA5 sea ice concentration at the start of a 9-day föhn melt event (**c**), the middle of the event (**d**), and on the day of initial phase of the LAIS collapse (**e**). Grey arrows indicate the mean föhn wind direction and the numbered boxes indicate the sea ice study region associated with the adjacent ice shelf for the correlation analysis (LAIS (1), LBIS (2), LCIS (3)).

3.3.3 Föhn melt and the surface liquid water budget

To better understand the role that föhn winds play in eastern AP ice shelf surface melt and stability we intercompare melt climatologies and the surface liquid water budget of all eastern AP ice shelves (Larsen A, Larsen B, SCAR inlet, Larsen C). A comparison of collapsed with intact ice shelves yields a clearer picture of the effects föhn winds have on ice shelf stability. We identify whether annual surface melt production, melt rate, melt hours, and surface temperature variables from 1980-2002 are significantly different from the LBIS (Figure 3.6 and corresponding two-tailed t-test statistics in Table B.2). We compare to LBIS because it was centered between other ice shelves and was the most recent to collapse. Total surface melt production on every ice shelf except LAIS differs significantly from LBIS melt (Mean annual melt over the ice shelf area; LAIS-476 mm w.e., LBIS-479 mm w.e., SCAR-353 mm w.e., Larsen(north)-336 mm w.e., LCIS-238 mm w.e.) (Figure 3.6a), which is expected when we consider the latitudinal location and mean annual air temperature (Figure 3.6d) (Table B.2). However, when föhn-induced melt is subtracted from total melt, the mean annual surface melt production on SCAR inlet and Larsen C (north) are not statistically different from the LBIS (LAIS-337 mm w.e., LBIS-321 mm w.e., SCAR-286 mm w.e., Larsen(north)-278 mm w.e., LCIS-203 mm w.e.) (Figure 3.6b). In other words, with the exception of föhn-induced melt (Figure 3.6c), melt production on SCAR Inlet and LCIS are statistically indistinguishable at the 95% confidence interval from LBIS melt production. Föhn wind-induced surface melt impacted collapsed ice shelves significantly more than SCAR inlet and the LCIS which further defines föhn melt as an important contributor to LAIS and LBIS melt budget.

Our analysis of firn density or available firn pore space identifies significant differences in ice shelves that have collapsed (LAIS, LBIS) and those that remain intact (SCAR inlet, LCIS). The liquid-to-solid ratio (LSR) is a crude proxy for available firn air content with extant ice shelves (SCAR inlet, LCIS) have an LSR just above 1 for the period 1980-2002 if all surface melt is included (Figure 3.7a). The LSR for LAIS and LBIS is also just above 1 for this period, though only if föhn-induced surface melt is excluded (Figure 3.7b). When surface melt caused by föhn wind is included, LSR exceeds 1.5 throughout extensive regions, including the ice shelf margins, of the LAIS and LBIS. Thus the collapsed ice shelves experienced climatological LSRs significantly larger than the SCAR inlet and the LCIS, mainly due to föhn-induced melt. It is important to note that there is evidence that the LCIS experiences regions of firn densification through melt processes, however these regions are mostly focused close to the AP mountains, likely formed from the location of föhn jets (Hubbard et al., 2016). This result suggests that föhn-induced melt helped precondition the LAIS and LBIS to produce extensive melt lakes by long-term firn densification.

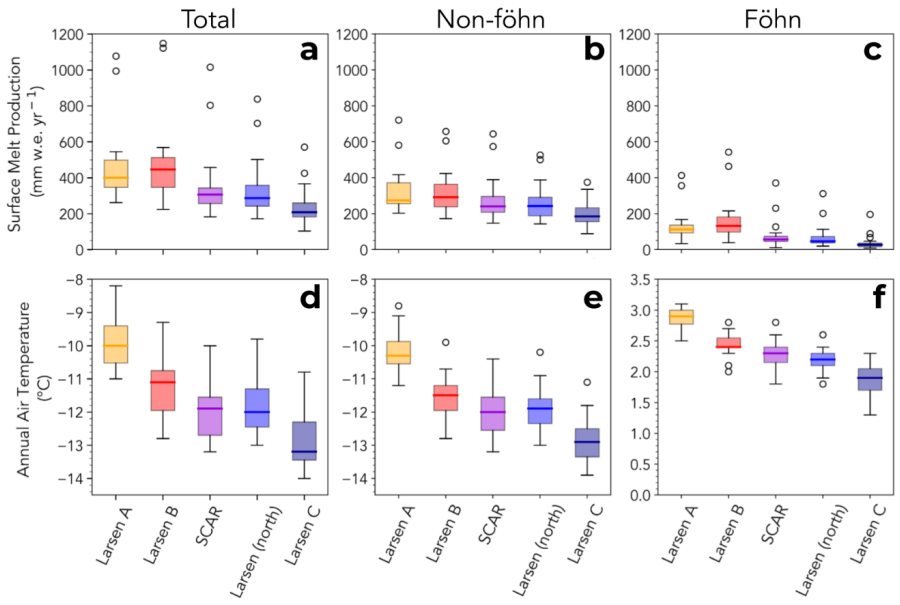

Figure 3.6. Box and whisker plots intercompare ice shelves with RACMO2-simulations from 1980-2002. Annual surface melt production (**a**) all melt, (**b**) non-föhn melt, (**c**) föhn-induced melt. (**d**) Mean annual air temperature, (**e**) air temperature without föhn winds, (**f**) air temperature during föhn winds. Note: the LAIS estimates are hypothetical after 1995, but are still resolved in the model simulations.

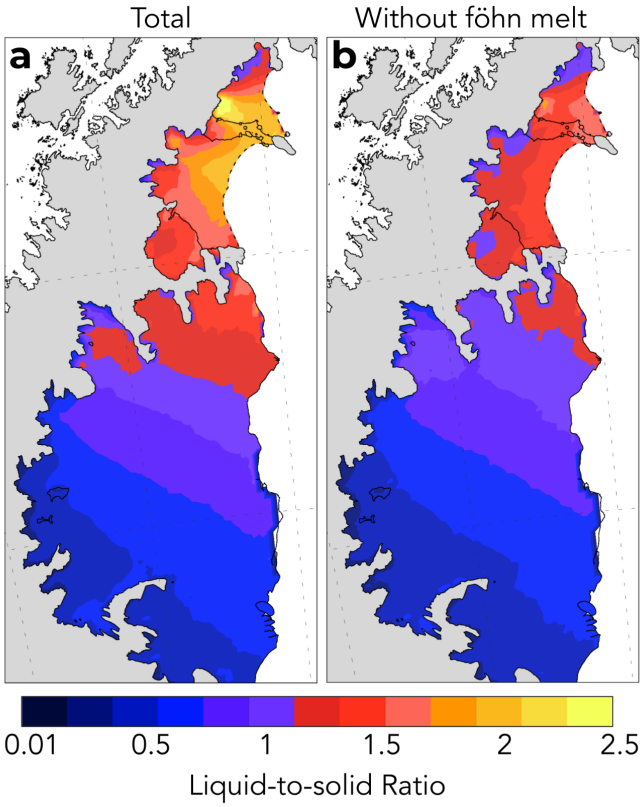

Figure 3.7. RACMO2 firn liquid-to-solid ratio or mean annual liquid water divided by mean annual frozen precipitation from 1979-2002 for (**a**) total melt and (**b**) all liquid water except föhn-induced melt. Note: the LAIS estimates are hypothetical after 1995, but are still resolved in the model simulations.

3.4 Discussion

The north/south temperature gradient present on the eastern AP ice shelves contributes to the differences in the ice shelf melt regime (Figure 3.6). Warmer ice shelves can be more vulnerable to long-term thinning and retreat that accelerate disintegration (Scambos et al., 2003; Morris and Vaughan, 2003). However, the temperature gradient alone does not explain the substantial increase in surface melt on the LAIS and LBIS relative to more southerly ice shelves. Only with the addition of föhn-induced surface melt (Figure 3.6c) do the LAIS and LBIS stand out significantly from the other eastern AP ice shelves (Figure 3.6a,b). Temperature gradient however, could explain why föhn wind events cause less melt on more southern ice shelves and may cause super melt events on collapsed ice shelves because temperature is already elevated on more northern ice shelves prior to the effect föhn has on temperature. With that in mind, we have examined liquid water processes on the spatio-temporal scales pertinent to AP ice shelf stability. For instance, the structural flow discontinuities or suture zones, where tributary glaciers merge together to form an ice shelf, are mechanically weak points that impact stability (Sandhager et al., 2005; Glasser and Scambos (2008); Glasser et al., 2009). These suture zones are further weakened through lateral shear depending on the difference in tributary glacier flow. All ice shelves in the region are composed of numerous outflow glaciers sutured together, and

while some studies suggest this is a major contributor to ice shelf instability, only two of the ice shelves have collapsed (Borstad et al., 2016; Glasser and Scambos, 2008). Further research suggests that marine accretion of ice on the bottom of the ice shelves, specifically LCIS, may stabilize these suture zones, which may be why SCAR inlet has remained intact despite major rift formation (McGrath et al., 2014; Borstad et al., 2016).

The timing of surface melt and melt enhanced by föhn winds within the melt season may also provide insight into the fate of LAIS and LBIS, including why neither ice shelf collapsed in the anomalously strong 1992/93 melt season (Figure 3.3d). Pore space within the upper snow and firn layers buffers surface melt before lakes begin to form (Polashenski et al., 2017). Late season melt is more likely to form surface melt lakes because meltwater from the preceding fall, winter, and spring has partially or completely filled available pore space. On both the LAIS and LBIS, 92% of surface melt during the 1992/93 melt season occurred before January 9th when there was more pore space to buffer the anomalous surface melt than at the onsets of their collapses in late January 1995 and early February 2002, respectively (Figure 3.4a, c). Melt lakes were present on both ice shelves throughout the 1992/93 melt season, though melt production slowed dramatically after mid-January, 1993 (Scambos et al., 2000). The high melt rates in late November and early December 1992 on the LAIS were perhaps too early in the melt season, and after too many years of nominal melt, to form substantial melt lakes and trigger hydrofracture that season. Nevertheless, the 1992/93 melt could have preconditioned the shelf for collapse in January 1995. The LBIS collapse began in February 2002 after the surface melt had returned to nominal, 1980s levels for six years. How much pore space had recovered during those six

years is unknown, and an important question for future research. Satellite images of surface melt lakes indicate 11% of the ice shelf was covered in melt lakes prior to collapse (Glasser and Scambos (2008)). However, the preceding melt year (2000/2001) had low melt and high precipitation, which added additional snow and water mass to the unstable ice shelf (Leeson et al., 2017).

Another possible reason collapse of the LAIS and LBIS did not occur in the 92/93 melt season or other years prior to collapse was a possible misalignment of the four prerequisites for rapid collapse theorized by Massom et al., (2018). An AVHRR image of the LAIS taken on December 8, 1992, just after a series of major föhn wind events that lead to 252 mm w.e. of surface melt in the 8 days prior to the image (Figure 3.4a), show significant melt lakes across the LAIS, which make hydrofracture cascades possible. However, in the same image, sea ice/melange are shown to be at the calving front, protecting the front from long period ocean swells that could trigger collapse. It may have been to early in the melt season to have substantial gaps in sea ice, the ocean temperature may have been to cold, ocean circulation could have help stabilize the sea ice at the front, the föhn winds speed could have been to weak to push the ice away or may have been in the wrong direction, all of which could have not allowed a proper trigger for collapse even though substantial melt ponds were present. Even if there were years or instances that sea ice extent was low and substantial melt lakes were present, there could have been a lack of long period ocean swells that are thought to trigger collapse.

Regardless of other possible contributors to ice shelf instability not considered here (e.g., basal melting), föhn-induced surface melt and associated melt lakes, and the off-coast

wind direction likely played an important role in pushing the LAIS and LBIS past a structural tipping point. The estimated surface melt lake depth caused by the 9-day föhn melt event on the LAIS surpassed a melt lake depth identified by modeled and satellite-derived lake depths before the collapse of the LBIS (Banwell et al., 2013; Banwell et al., 2014). The LAIS was likely the same thickness (200m) or thinner at the time of collapse so the estimate of critical surface lake depth for the LBIS that is applied to the LAIS may reflect an upper limit of melt lake depth of stability for the LAIS. Melt lake depth is likely underestimated because our estimation only accounts for melt during the 9-day melt event. Melt before this time period already exceeded an average melt year by 23% (118 mm w.e.) so melt lakes probably already existed.

3.5 Conclusions

The converging lines of evidence in these results show that observed and inferred föhn-driven melt is present in sufficient amounts, and at the right locations and times, to cause extensive surface melt lakes, while the off-coast föhn wind direction pushed sea ice away from the calving front. The fact that the LAIS and LBIS collapsed catastrophically within weeks and not through long-term thinning and retreat like other ice shelves (Prince Gustav, Wordie) suggests sudden disintegration is anomalous and requires forcings to match vulnerabilities (Scambos et al., 2003). We conclude that föhn winds and the associated surface melt played a significant role in the collapses of the LAIS and LBIS, while extant eastern AP ice shelves are not likely to collapse from föhn-induced melt and hydrofracture in today's current climate. We have come to these conclusions with the following forms of evidence:

- First, both the LAIS and LBIS are impacted by powerful melt-inducing föhn jets that affect a large spatial portion of each ice shelf and reach the ice shelf terminus. Surface melt and melt lakes near the ice shelf terminus can lead to calving front collapse and structural instability for the remaining portion of the ice shelves (Depoorter et al., 2013; Pollard et al., 2015). SCAR inlet and the LCIS are either not directly affected by a föhn jet, are too vast to have any significant effect near the terminus, or are too far south to experience major melt events.
- Second, strong föhn winds were present prior to and during collapse for the LAIS and LBIS. A series of three föhn events on the LAIS lasted nine days total and produced over 25% of the total annual melt for the 1994/95 melt season, while föhn was present prior to and during the collapse of the LBIS which enhanced surface melt rates. Enhanced melt, filled new and existing melt lakes above the melt lake depth observed on the LBIS (1m) and modeled lake depth (5m) that could trigger large-scale hydrofracture cascades. The föhn winds on both ice shelves actively pushed/melted sea ice away from the calving front allowing long period ocean swells to trigger large-scale hydrofracture cascades on the LBIS and possibly LAIS, exacerbated by extensive surface melt that originated from the ice shelf terminus.
- Third, in the absence of föhn wind-induced melt, the surface liquid budgets of collapsed and intact ice shelves are climatically similar, which points to föhn winds as a driver of increased surface melt and extensive melt lakes on collapsed ice shelves. The additional föhn induced-melt on the LAIS and LBIS compared to intact

ice shelves helped precondition the LAIS and LBIS to produce extensive melt lakes by long-term firn densification.

This research clarifies the roles of föhn-induced melt for collapsed and extant ice shelves on the eastern AP. Future analyses of these ice shelf collapse events using advanced firn density models coupled with ice-ocean-atmospheric coupled simulations may be useful to better understand the role of surface melt in ice shelf instability. Further, the AP föhn wind regime has remained stable over the past half-century (Laffin et al., 2021) which points to enhanced surface temperatures and increased liquid phase precipitation as more important contributors to the future surface liquid budget on remaining ice shelves and is an important area of future research (Bozkurt et al., 2020; Bozkurt et al., 2021). However, changes in climate drivers such as the Southern Annular Mode (SAM), which influences the north-south movement of the westerlies in the region, may alter the temperature and föhn occurrence that will likely enhance surface melt in locations farther south, and therefore make more southern ice shelves more vulnerable (Abram et al., 2014; Zheng et al., 2013; Lim et al., 2016;). Nevertheless, this research highlights a new understanding behind föhn melt mechanisms for ice shelf collapse and suggests that SCAR inlet and the LCIS may remain stable so long as surface liquid water from melt and precipitation remains within historical bounds.

Acknowledgments

MKL was supported by the National Science Foundation (NRT-1633631) and NASA AIST (80NSSC17K0540). CSZ gratefully acknowledges support from the DOE BER ESM and

SciDAC programs (DE-SC0019278, LLNL-B639667, LANL-520117). JMVW acknowledges support by PROTECT and was partly funded by the NWO (Netherlands Organisation for Scientific Research) VENI grant VI.Veni.192.083. We thank Dr. Helmut Rott for generously providing detailed in-person observations of the LAIS months before collapse. We also thank the Institute for Marine and Atmospheric research Utrecht (IMAU) for providing RACMO2 output. RACMO2 model data are available by request at https://www.projects.science.uu.nl/iceclimate/models/antarctica.php, however, a subset (2001-2018) of the data are hosted online at https://zenodo.org/record/3677642#.X-pXAFNKjUI. This work utilized the infrastructure for high-performance and high-throughput computing, research data storage and analysis, and scientific software tool integration built, operated, and updated by the Research Cyberinfrastructure Center (RCIC) at the University of California, Irvine (UCI). The RCIC provides cluster-based systems, application software, and scalable storage to directly support the UCI research community. https://rcic.uci.edu

CHAPTER 4

The contribution of föhn and katabatic winds to ice sheet surface melt in Greenland and Antarctica

4.1 Introduction

The Greenland (GIS) and Antarctic ice sheets (AIS) hold enough water to raise global sea levels by 65.4m (GIS-7.4m, AIS-58m) and have already contributed to 18.4mm (GIS-10.8 ± 0.9mm, AIS-7.6 ± 3.9mm) of sea level rise since 1992 (Rignot et al., 2008; Hanna et al., 2013; The IMBIE team, (2018, 2020)). Recent mass loss from the GIS has been primarily attributed to surface melt and runoff due to warmer air temperatures (Noël et al., 2014; Fettweis et al., 2017; Straneo et al., 2013) and increased isolation due to reduced summer cloud cover (Fettweis et al., 2013; Tedesco et al., 2013; Hofer et al., 2017; Noël et al., 2019). Mass loss from the AIS has been attributed to increased surface runoff and acceleration of marine-terminating glaciers primarily from regional increased air and ocean temperatures that have cause thinning, retreat, and collapse of marine-terminating glaciers and ice shelves (Rignot et al., 2004, 2014; Scambos et al., 2004; Konrad et al., 2018; Bozkurt et al., 2020, Auger et al., 2021). Surface melt and subsequent runoff are responsible for more than 80% of mass loss acceleration since the 1990s on the GIS (Enderlin et al., 2014; Andersen et al., 2015; Fettweis et al., 2017), and contribute to decreased ice shelf stability and collapse on ice shelves surrounding the AIS, which help to buttress grounded ice (Massom et al, 2018; Laffin et al., 2022).

On the margins of the GIS and AIS directionally consistent katabatic winds, and föhn winds mainly focused on the Antarctic Peninsula (AP), enhance surface melt rates (Lenaerts

et al., 2017; Datta et al., 2019; Laffin et al., 2021, 2022; Wang et al., 2021). Katabatic winds originate in the cold, high, and dry ice sheet interior where relatively dense surface air drains downslope towards warmer regions. The polar highs coupled with the very cold and sloped ice sheets, make katabatic winds a consistent force on both ice sheet margins and some of the strongest and most persistent winds on Earth (Bromwich 1988; Parish and Cassano, (2003)). Föhn winds form when relatively cool moist air, forced over a mountain barrier, releases latent heat and precipitates during ascent. The warmer, drier air descending the leeside slope and compresses to create warm and dry gusty winds (Elvidge and Renfrew (2016)). Both wind mechanisms reduce atmospheric moisture and inhibit cloud formation which increases surface insolation and heating (Vihma et al., 2011; Mioduszewski et al., 2016). The strong winds turbulently mix the stable polar boundary layer, enhance sensible heat exchange, and accelerate surface melt (Nylen et al., 2004; Vihma et al., 2011; King et al., 2017; Kuipers Munneke et al., 2018 Laffin et al., 2021; Wang et al., 2021).

The effect of föhn and katabatic winds on surface processes has been studied extensively on both the GIS and AIS. Observational and model studies have identified impacts of downslope winds on surface temperatures (Parish and Bromwich, (1986); Nylan et al., 2004), the surface energy budget (Kuipers Munneke et al., 2012, 2018, Laffin et al., 2021; Le Toumelin et al., 2021), surface mass balance including enhanced surface melt (Kuipers Munneke et al., 2012, 2018, Laffin et al., 2021), coastal precipitation (Grazioli et al., 2017), snow mass transport (Grazioli et al., 2017; Palm et al., 2017), ice shelf stability (Laffin et al., 2022), and sea ice and polynya formation with attendant impacts on ocean

currents and biological productivity (Davis and McNider, (1997), Cape et al., 2014; Wenta and Cassano, 2020). Additionally, winds faster than 5-8m/s can cause blowing snow that reflects shortwave radiation and enhances sublimation that limit surface melt (Grazioli et al., 2017; Le Toumelin et al., 2021), or expose bare ice that triggers the snow-ice albedo feedback (Leanarts et al., 2017).

Despite extensive research, the contribution of downslope wind associated melt compared to total melt, extent to which downslope wind regimes have changed, and how those changes have affected total melt and melt trends is unclear. Here we use RACMO2 simulations of the GIS from 1961-2019 and AIS from 1981-2019 to quantify melt associated with föhn and katabatic winds, and how the wind regimes on each ice sheet have responded to anthropogenic forcings. Section 2 describes the data and methods. Section 3 summarizes the total melt, mechanisms for melt, and melt trends related to climate change. Section 4 summarizes the main findings and discusses the implications of the study in relation to the current understanding of surface melt on the GIS and AIS.

4.2 Data and Methods

4.2.1 Regional Climate Model 2 Simulations (RACMO2)

We base our GIS and AIS analysis on 3-hourly output from simulations by the Regional Atmospheric Climate Model 2 (RACMO2), version 2.3p2, with a horizontal resolution of 5.5km (0.05°) focused on the GIS from 1961-2019 and 27.5km (0.25°) focused on the AIS from 1981-2019. RACMO2 uses the physics package CY33r1 of the European Centre for Medium-Range Weather Forecasts-Integrated Forecast System (ECMWF-IFS, 2008) in combination with atmospheric dynamics of the High-Resolution Limited Area

Model (HIRLAM). When compared with AWS observations on the surface air temperature has a slight warm bias and downwelling shortwave/longwave radiation are over/under estimated due to underestimation of clouds and moisture but overall reproduce surface observations (Noël et al., 2018; Bozkurt et al., 2020; King et al., 2015; Laffin et al., 2021). RACMO2 is forced at the lateral boundaries with ERA-Interim data (Dee et al., 2011) and shows improvement in the surface energy fluxes and near-surface temperature from previous versions compared with AWS observations (Van Wessem et al., 2018; Bozkurt et al., 2020)

4.2.2 Downslope wind detection

We identify föhn and katabatic winds using a downslope direction method previously used for other katabatic and föhn wind identification studies (Parish and Cassano, (2003); Wang et al., 2021). We associate katabatic and föhn wind with melt that occurs when the wind direction is aligned with the topography surface slope while surface melt occurs. We identify katabatic flow on the GIS when the wind direction is within -10 degrees to the left and 60 degrees to the right of the downslope direction. The Coriolis force can steer katabatic flow in the northern hemisphere to the right by up to 60 degrees (van den Broeke et al., 1993; Wenta and Cassano, (2020)). Mesoscale meteorological pressure gradients and differential heating of ice and land from albedo differences can enhance katabatic flow (Klein and Heinemann, (2002)) and steer it in either direction. The Coriolis force steers in the opposite direction in the southern hemisphere where katabatic flow will be -60 degrees to the left and 10 degrees to the right of the AIS topographic downslope direction. This method is also useful for identifying föhn winds which primarily occur on

the AP and Marie Byrd Land of the AIS (Nylan et al., 2004; Speirs et al., 2010; Elvidge et al., 2015, 2016; Laffin et al., 2022). Traditionally, föhn winds are identified by their meteorological signatures of warmth, dryness, and gustiness (Cape et al., 2015; Datta et al., 2019; Elvidge et al., 2020; Turton et al., 2018; Laffin et al., 2021), however this downslope method also identifies föhn winds because on the leedside of the mountains they are funneled through topography as they descend and so mirror topographic slopes (Elvidge et al., 2016).

4.3 Results

4.3.1 GIS katabatic melt regime

Surface melt associated with the katabatic downslope wind direction (which accounts for Coriolis steering) occurs primarily on the periphery of the GIS (Figure 4.1a). Overall, surface melt coincident with katabatic winds accounts for 27.5 ± 4.5% of the total annual surface melt and can reach as high as 98.6% (Figure 4.1b). The Katabatic-associated surface melt maximizes in the western portion of the ice sheet at 1910 ± 5.2 mm w.e. yr^{-1} or 64 ± 5.2% of total melt. Prior to the 1990s surface melt associated with downslope winds was stable, however after the 1990s melt increased by 14 Gt/yr (10.3 ± 2.5%) with the largest melt increases in the months of June (1.8% yr^{-1}) and July (1.6% yr^{-1}) (Figure 4.2, Figure C.1). Over the same period, total surface melt increased by 183 Gt/yr (34 ± 5.8%) indicating downslope wind associate melt is increasing less and likely affected by increased surface temperatures that inhibit katabatic formation.

The surface energy fluxes that dominate surface melt production associated with katabatic winds are shortwave radiation and sensible heat exchange (Wang et al., 2021).

Shortwave absorption constitutes 86 ±11% of the positive energy balance components during melt associated with katabatic flow (Figure 4.3). However, this distribution is not uniform over the entire GIS. 79% of the katabatic associated melt area surface melt on the southern GIS (south of 72°N) is driven (>50% of the positive energy balance components) by shortwave absorption, with sensible heat flux making up the other 21% (Figure 4.3a). On the northern portion of the GIS, katabatic associated surface melt is primarily driven by the sensible heat flux over 70% of the melt area. These results are inconsistent with Wang et al., 2021 because they considered the sub-monthly melt timescales, and showed that sensible heat drives the melt variability, while shortwave absorption supplies most of the absolute power.

In the ablation zone on the GIS periphery, where topographic slope and wind speed are greatestest, sensible heat transfers more melt energy to the surface, but does not over power shortwave absorption as a main driver of melt for the southern GIS (Figure 4.3b). We also confirm the increase in shortwave absorption and sensible heat during downslope winds when melt occurs (Kuipers Munneke et al., 2012, 2018; King et al., 2015; Wang et al., 2021). However, when melt is absent, katabatic winds stronger than 5-9 m/s (depending on snow type) can create blowing snow that act as low level clouds that can reduce the amount of shortwave absorption at the ice surface along with upper and mid-level clouds (Palm et al., 2017; Xie et al., 2021) (Figure 4.3b). Additionally, blowing snow also sublimates in the dry katabatic air further reducing air temperature, essentially protecting the ice surface from melt (Palm et al., 2017).

Surface melt associated with katabatic flow generally increases through the simulation period (1961-2019), however katabatic-associated melt increases after the 1990s (Figure 4.1c,d, Figure C.1). While katabatic-associated melt increased by 10.3% from 1991-2019 relative to 1961-1990 (Figure 4.2, Figure C.1), the western GIS ablation zone downslope wind speeds slowed on average by 0.37 m/s (6.4%) over the same period. The North Atlantic Oscillation (NAO) helps explain this apparent conundrum. The negative phase of the summer NAO causes a blocking high to form over the GIS which becomes more negative after 1994. This supports the formation of katabatic winds and clear skies (Fettweis et al., 2013; Mioduszewski et al., 2016; Tedesco et al., 2013). Negative summer NAO also corresponds with warmer surface temperature that increases surface melt, though decreases the formation of katabatic winds.

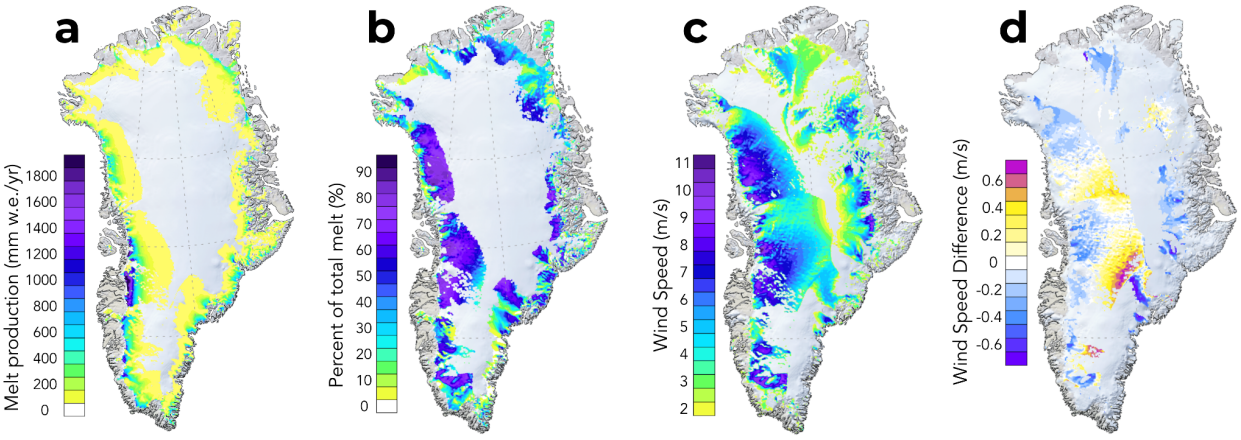

Figure 4.1. (**a**) Annual average surface melt pattern associated with katabatic downslope winds from 1961-2019. (**b**) Percent of the total annual melt associated with katabatic winds from 1961-2019. (**c**) Average wind speed during downslope katabatic winds. (**d**) Multi-decadal difference in wind speed during down slope wind computed as 1991-2019 mean minus 1961-1990 mean.

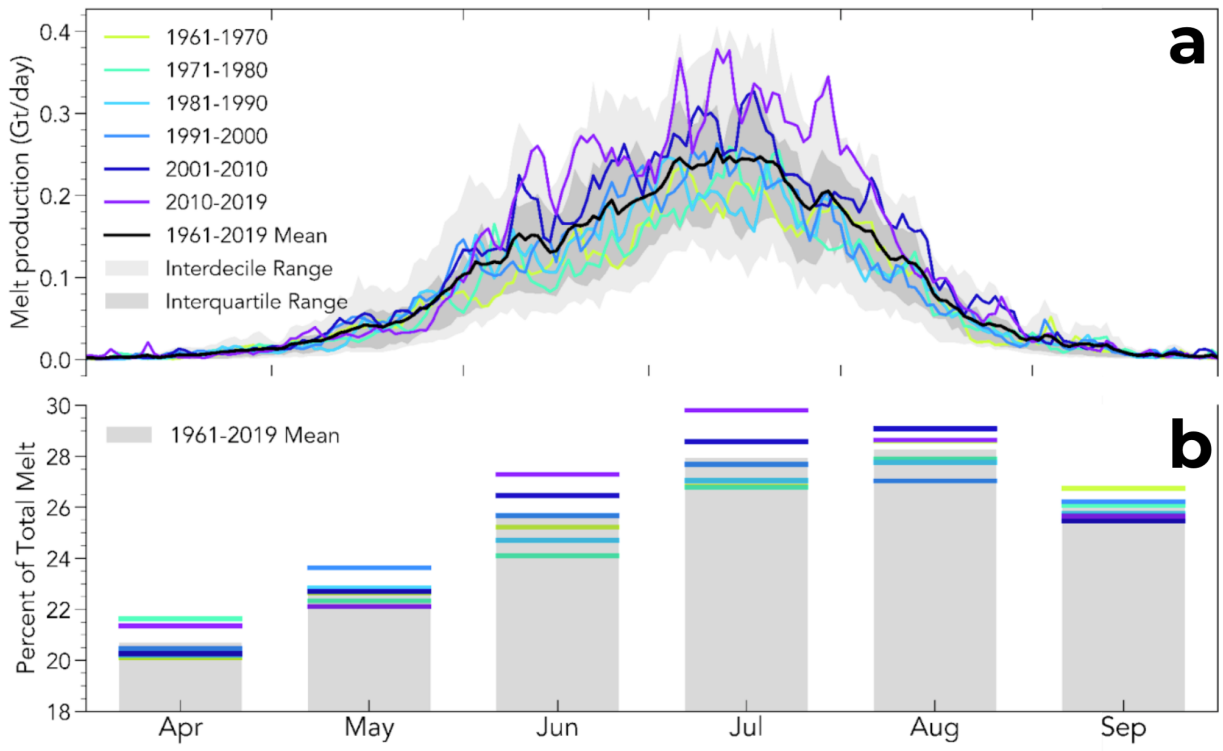

Figure 4.2 (**a**) Time series of RACMO2 surface melt production associated with katabatic winds on the GIS, averaged by decade from 1961-2019. (**b**) Percent of total melt on the GIS, averaged monthly and by decade from 1961-2019.

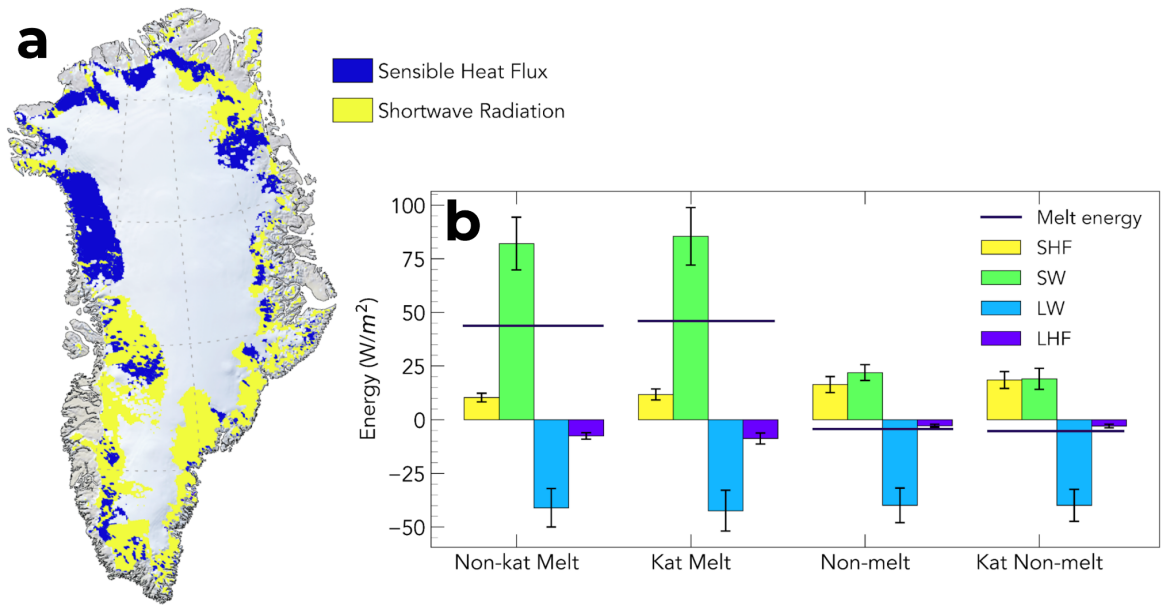

Figure 4.3 (**a**) Spatial pattern of the primary (>50%) positive energy balance components during melt associated with downslope winds averaged from 1961-2019. (**b**) Average energy balance during melt not associated with downslope winds (Non-kat Melt), melt associated with downslope winds (Kat-Melt), no melt and no downslope winds (Non-melt), no melt associated with downslope winds (Kat Non-melt).

4.3.2 AIS katabatic melt regime

Surface melt associated with the katabatic downslope wind direction (steered to the left by the Coriolis effect) occurs primarily on the periphery of the AIS and its ice shelves which represents 19.7 ± 3.8% of total surface melt (Figure 4.4a). The ice shelves (Abbot(1), Amery(2), Shackleton(3), Totten(4)) that often experience katabatic flow also experience enhanced summer surface melt during these events. The Totten and Shackleton ice shelf melt associated with downslope wind constitutes 81 ± 3.7% and 55 ± 2.5% of their respective total surface melt amounts (Figure 4.4b). The greatest AIS climatological surface melt rate (412 mm w.e. yr^{-1}) occurs on the western AP due to infrequent yet powerful föhn winds (Cape et al., 2015; Datta et al., 2019; Laffin et al., 2021, 2022). Surface melt is underestimated in this region because the RACMO2 model resolution (27.5km) does not resolve sub-grid scale föhn winds that are funneled through topography (Laffin et al., 2021). However, this model resolution is able to simulate an overall föhn effect that shows increased surface melt at the base of the AP mountains as observed in previous research (Elvidge et al., 2015; Datta et al., 2019; Laffin et al., 2021, 2022). The mean surface melt declined by 5.8 Gt yr^{-1} (27.8 ± 5.3%) from the first 20 years (1981-2000) to the second (2001-2019), consistent with previous research of total melt (Figure 4.5, Figure C.1)(Trusel et al., 2013). Total melt over the same time period declined by 5.8 Gt/yr (-31.8 ± 5.3%), which is less than wind associated melt because wind associate melt on the AIS excluding

the AP is consistent representing 15 Gt/yr (-15.4 ± 2.4%) of wind associated melt. Föhn-winds cause surface melt on the AP that represents 64.3 ± 6.4% of total melt and varies significantly depending on the phase of the SAM and thus drives the AIS-wide melt trend (Turner et al., 2016; Laffin et al., 2021, 2022).

Overall shortwave absorption constitutes 76 ± 9% of the positive energy balance components during melt associated with föhn and katabatic flow on the AIS (Figure 4.6). This distribution is not uniform over the entire AIS. The surface energy balance, similar to the GIS, also indicates increased solar and sensible heat during melt associated with katabatic flow, and reduced shortwave absorption during katabatic flow that does not cause melt likely due to cloud shadowing and to blowing snow can block shortwave radiation and sublimate (Figure 4.4c,d). Unlike the GIS there has been no AIS-wide trend in katabatic wind speed in recent decades Nevertheless, the AIS and most of its ice shelves are losing mass at an accelerating rate (Rignot et al., 2013). Warmer atmospheric temperatures and a more positive Southern Annular Mode (SAM) help explain accelerating melt on the AP (Turton et al., 2020).

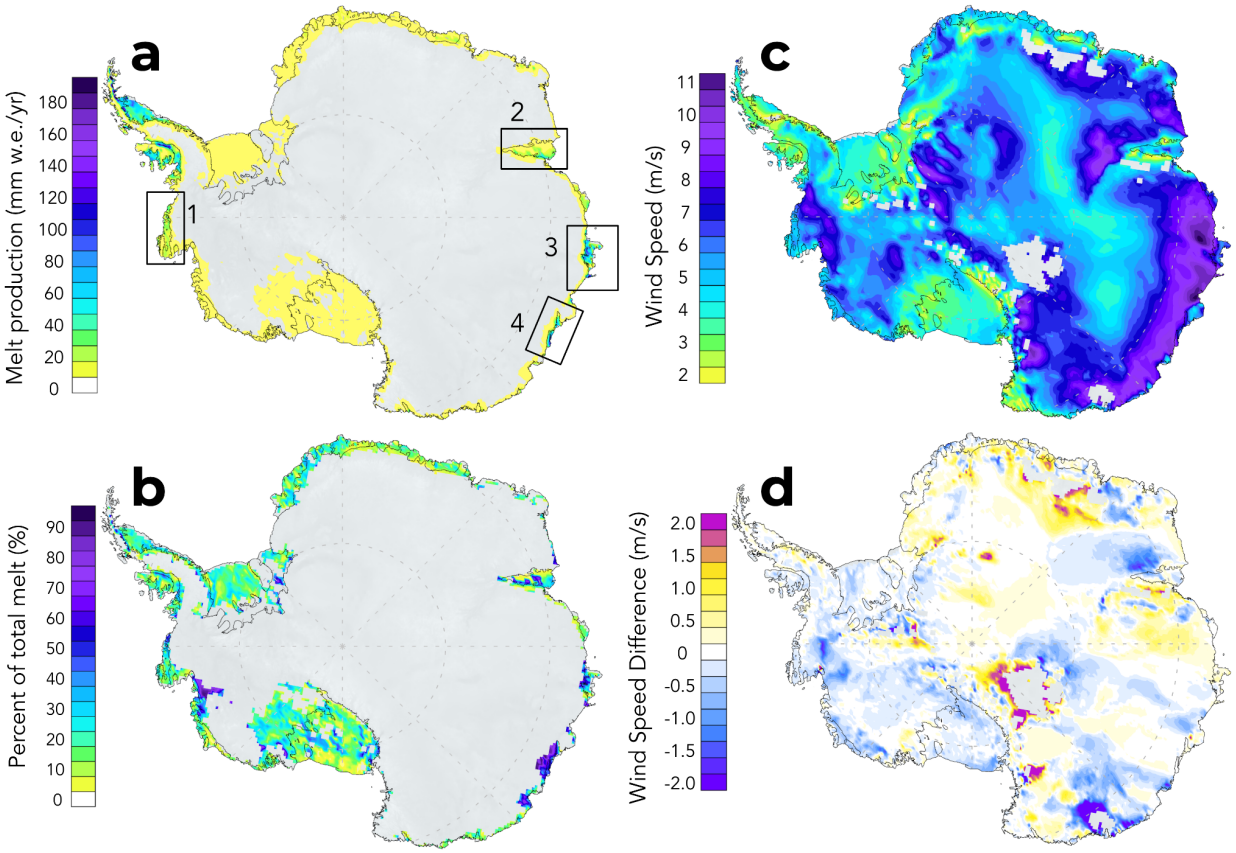

Figure 4.4 (**a**) Annual average surface melt pattern associated with katabatic downslope winds from 1981-2019. Numbered rectangular regions indicate ice shelves; 1-Abbot, 2-Amery, 3-Shackleton, 4-Totten (**b**) Percent of the total annual melt associated with katabatic winds from 1981-2019. (**c**) Average wind speed during downslope katabatic winds. (**d**) Difference in wind speed during down slope wind from the average of 2001-2019 minus the average of 1981-2000.

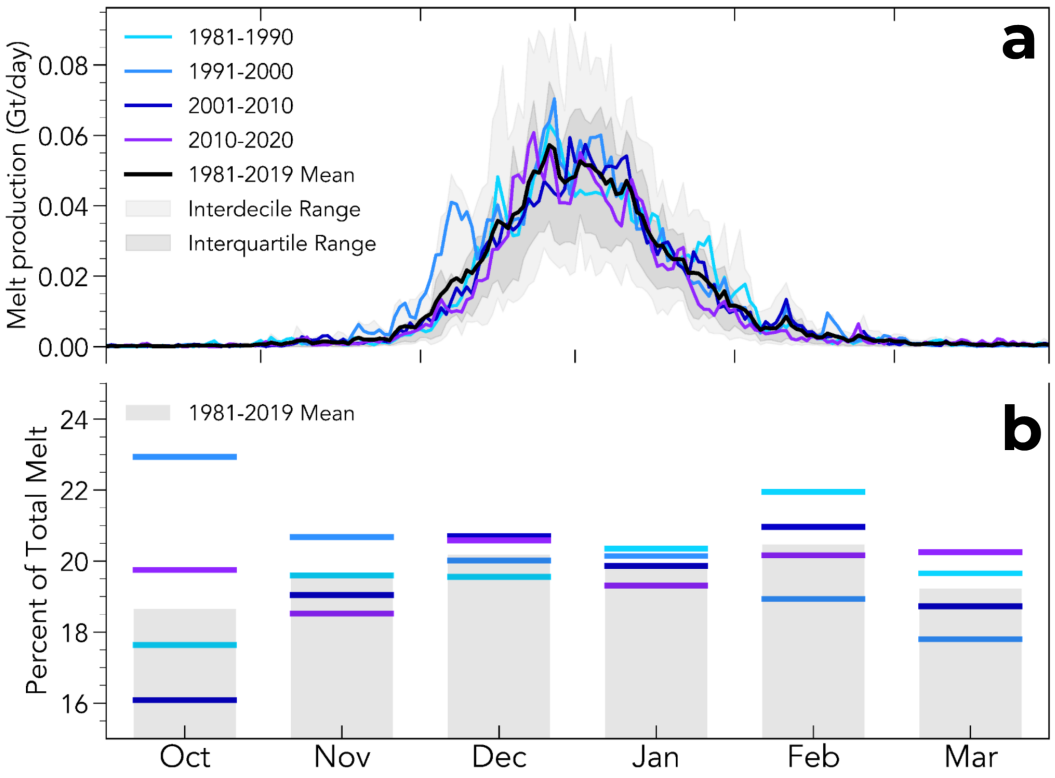

Figure 4.5 (**a**) Time series of RACMO2 surface melt production associated with katabatic winds on the AIS, averaged by decade from 1981-2019. (**b**) Percent of total melt on the AIS, averaged monthly and by decade from 1981-2019.

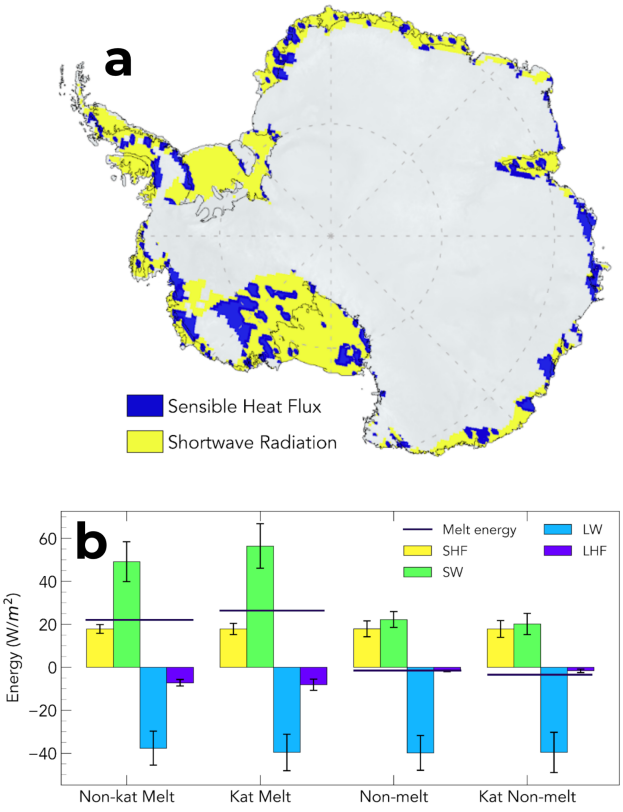

Figure 4.6 (**a**) Spatial pattern of the primary (>50%) positive energy balance components during melt associated with downslope winds averaged from 1961-2019. (**b**) Average energy balance during melt not associated with downslope winds (Non-kat Melt), melt associated with downslope winds (Kat-Melt), no melt and no downslope winds (Non-melt), no melt associated with downslope winds (Kat Non-melt).

4.4 Discussion and Summary

We use RACMO2 simulations of the GIS from 1961-2019 and AIS from 1981-2019 to examine how much melt is associated with föhn and katabatic (downslope) winds, and how the wind regimes, associated melt, and total melt on each ice sheet have responded to recent climate change. Results reveal that surface melt associated with downslope winds is significant on both the GIS and AIS, and constitutes a climatological average of 19.7% and 27.5% of total surface melt respectively. The western GIS and AP in particular experience

significant melt associated with katabatic and föhn winds. Overall the AIS has experienced a decrease of 31.8% in downslope wind-associated melt since 1999 mostly due to reduced föhn generated melt on the AP (Laffin et al., 2021). Since 1995 the GIS has experienced an increase of 10.3% in melt associated with downslope winds which is a smaller increase than total melt (34%).

The increasing trend in GIS melt associated with downslope winds began in the 1990s with the majority occurring after 2006, however the relative increase in melt (10.3%) is smaller than that of total melt (34%). This melt increase is associated with the negative phase of the summer NAO which leads to persistent high pressure blocking over the GIS (Fettweis et al., 2013; Tedesco et al., 2013). The resulting clear skies allow radiative cooling of the ice surface and promote downslope katabatic flow. However, the blocking high also increases surface insolation which increases air temperatures and reduces the katabatic wind speeds illustrated in Figure 4.1d. In the ablation zone this blocking has slowed downslope wind speeds yet increased melt because of increased solar surface absorption. In the accumulation zone of the central GIS, winds have accelerated since 1995, likely because the anticyclonic rotation of the blocking high now aligns with the shallow downslope direction and does not indicate an increase in katabatic wind strength.

There are clear differences between the GIS and AIS downslope wind associated melt regimes. The relative importance of the positive energy balance components during katabatic and föhn winds (shortwave absorption (SW) and sensible heat flux (SHF)) differ between the GIS (SW-89%, SHF-11%) and AIS (SW-74%, SHF-26%) for three reasons; 1) the GIS receives more shortwave radiation due to its location closer to the equator, 2) the

GIS is warmer than the AIS and requires less positive energy balance to trigger melt, 3) the AIS wind associated melt regime is primarily driven by the AP föhn winds which can significantly enhance sensible heat fluxes compared to katabatic winds (Figure 4.3b, 4.6b). The GIS wind associated melt trend has increased 10.3% in the past 20 years while on the AIS it has decreased 32%. The wind associated melt on the AIS has decreased along with total melt, however the variability in föhn wind associated melt in the past 20 years helps explain the total melt decrease, because the majority of surface melt on the AIS occurs on the AP (Turner et al., 2016). In contrast the GIS wind associated melt regime has increased through time, though more slowly than total surface melt. The enhanced surface temperatures on the GIS affect the buoyancy of air at the surface, which makes it less dense which decreases the velocity of katabatic flow. Downslope associated surface melt has increased because surface temperatures have increased, however the downslope winds are weaker leading to decreased wind associated melt.

Over the past 20 years wind associated melt has decreased 31.8% on the AIS while total melt decreased 15.4% due to decreased föhn-induced melt on the Antarctic Peninsula which drives the overall melt trend for the AIS. Wind associated melt has increased 10.3% on the GIS but less than total melt 34% because of a more negative NAO and summer blocking over the GIS which ultimately leads to warming surface temperatures that inhibit katabatic wind speed. Surface melt is a key contributor to sea level rise through direct runoff and can cause ice shelf instability which indirectly affects sea level rise through buttress force of grounded glaciers. How surface melt associated with downslope winds has

changed through time will help clarify how these wind and associated melt regimes will change as the polar regions continue to experience the results of climate change.

Acknowledgments

MKL was supported by the National Science Foundation (NRT-1633631) and NASA AIST (80NSSC17K0540). CSZ and WW gratefully acknowledges support from the DOE BER ESM and SciDAC programs (DE-SC0019278, LLNL-B641620, LANL-520117). JMVW acknowledges support by PROTECT and was partly funded by the NWO (Netherlands Organisation for Scientific Research) VENI grant VI.Veni.192.083. We also thank the Institute for Marine and Atmospheric research Utrecht (IMAU) for providing RACMO2 output. RACMO2 model data are available by request at https://www.projects.science.uu.nl/iceclimate/models/antarctica.php, however, a subset (2001-2018) of the data are hosted online at https://zenodo.org/record/3677642#.X-pXAFNKjUI. This work utilized the infrastructure for high-performance and high-throughput computing, research data storage and analysis, and scientific software tool integration built, operated, and updated by the Research Cyberinfrastructure Center (RCIC) at the University of California, Irvine (UCI). The RCIC provides cluster-based systems, application software, and scalable storage to directly support the UCI research community. https://rcic.uci.edu

CHAPTER 5

Conclusions

5.1 Summary of Results

The goal of my dissertation was to better understand the contributory role of föhn and katabatic winds and associated melt on the GIS and AIS, and if melt trends have changed through time. Our understanding of ice sheet dynamics and sea level rise hinge upon understanding every contributor to surface mass balance. I first created a machine learning algorithm to identify when and where föhn winds occur on the AP. Then, I used what was learned on the AP and researched the effect of föhn winds on ice sheet stability and applied all that was learned to understand downslope wind associated melt on the GIS and AIS.

In Chapter 2, I examined how föhn-induced melt affects the spatial melt pattern of the Antarctic Peninsula (AP), especially south of the Larsen C ice shelf and west of the AP, what fraction of the total melt on the AP is caused by föhn winds, and whether melt trends and it's drivers evolved through time on the AP. To do so, I use in situ meteorological observations to train a Machine Learning algorithm to identify the föhn signature in ERA5 global reanalysis and RACMO2 regional climate model simulations. I found that machine learning is a useful and accurate way to identify when and where föhn winds occur on the AP. I also found that föhn winds are a significant driver of surface melt on the eastern and western ice shelves of the AP and melt trends mirror those of air temperature through time. This research provided a valuable proof of concept for the machine learning algorithm

using weather stations and model simulations and helped to better identify the drivers of melt on the AP.

In Chapter 3, I used the same föhn detection algorithm and RACMO2 simulations to identify the contributory role of föhn winds in rapid ice shelf collapse. I found that föhn winds were present at the time of collapse for the Larsen A and B ice shelves which increased surface melt and pushed sea ice away from the calving front. The increased surface melt led to large scale surface melt ponds and hydrofracture cascades. Additionally, föhn winds on the AP pushed sea ice away from the calving front and allowed large period ocean swells to initiate collapse. I also assessed the vulnerability of the remaining ice shelves Scar inlet and Larsen C to collapse from föhn induced surface melt and found that these ice shelves are not affected in the same manner as collapsed ice shelves from föhn winds and therefore are less susceptible to collapse under our current climate.

In Chapter 4, I expand what I learned on the AP and use RACMO2 simulations to explore the impact, trends, and drivers of föhn and katabatic wind and associated melt on the Greenland (1961-2019) and Antarctic (1981-2019) ice sheets. I found that melt associated with downslope winds (katabatic and föhn) on the Antarctic ice sheet has decreased while on the Greenland ice sheet melt has increased. Then I explore the wind associated melt trends which generally mirror total melt trends on each ice sheet however, on the Greenland ice sheet wind associated melt has increased less compared to total surface melt. This trend is related to a more negative summer North Atlantic Oscillation (NAO) which forms a blocking high on the Greenland ice sheet that warms surface

temperatures and decreases the wind speed of katabatic winds, ultimately decreasing wind associated melt.

The collective results of my dissertation help us understand how much melt is associated with downslope föhn and katabatic winds compared to total surface melt and how these melt regimes have changed in the past 60 years. Föhn winds are prominent drivers of surface melt on the Antarctic peninsula and can negatively impact ice shelf stability. Katabatic winds help to drive surface melt on the periphery of both ice sheets; however with warming surface temperatures the negative buoyancy forces associated with katabatic flow decrease, ultimately limiting the impact of katabatic melt in a warming climate. The results of my dissertation will help provide a better understanding of the climate system and its effect on sea level rise through time with the hopes to better constrain the role of melt in the climate system.

5.2 Research Perspectives and Future Directions

5.2.1 Machine Learning and Earth System Science

The machine learning (ML) fohn detection algorithm developed in Chapter 2 provides a new and valuable use for ML in Earth system science. We use automatic weather stations to inform an ML model how föhn winds affect meteorological variables in regional climate model simulations. Using weather stations to teach the ML model ensures the laws of thermodynamics are conserved from a physical standpoint while providing valuable insight for research perspectives. The use of ML in Earth system science continues to expand because these systems often occur in distinguishable patterns that ML algorithms

can easily identify, however, the importance of model evaluation should not be overlooked to ensure the rigorous standard of scientific research.

The past few decades have provided an exponential increase in Earth-related observations which is why ML has become more popular in Earth system science research. However, ML used to model the Earth system can be flawed. When it comes to physically based systems the importance of conserving physical properties cannot be overstated. If an ML algorithm is only provided data that does not include either a loss function or observations that maintain the physical constraints of the system, then the ML algorithm results can become unphysical. It is easy to train a model and get a result by identifying a pattern in data but representing physical constraints when using ML helps to provide validity in the scientific results and research and should be a focus for researchers.

The importance of ML that is physically constrained is illustrated by a comparison of two different ML models aimed to map the topography below the Greenland and Antarctic ice sheets. One previous study attempts to increase the accuracy and roughness of the bed topography of Antarctica using a GAN (Generative Adversarial Network) ML model (Leong and Horgan, 2020). Results for this model slightly increased accuracy of the bed topography compared to limited radar observations, however when extrapolating this model to regions not used in the training data, obvious, non-physical artifacts were observed. Additionally the roughness increased but did not reflect observations. The GAN used for this model was not constrained by physics, it was only provided data without context to make decisions that ultimately impacted the physical validity of the model.

Our new method, done in collaboration with Dr. Mathieu Morlighem and Dr. Emri

Neftci takes a different approach that uses a deep neural network to map the bed topography of Greenland and Antarctica (Morlighem et al., 2022). Our method provides the ML model with satellite observations of surface height, flow speed, and flow direction which reflect basal features. We also incorporate a loss function that takes into account the surface mass balance that penalizes any model prediction that does not conserve mass. This ensures that our model is informed by physics and provides a more realistic model of the bed topography. Most importantly it improves upon the previous bed topography model and does not create topography patterns or roughness that are inconsistent with true features.

Additionally the use of model evaluation techniques, specifically when ML is used for scientific research, is important to guide a model's physical fidelity while also ensuring that the model does not over or underfit observational data. ML for industry often is only evaluated using one technique or not at all. To ensure the ethical efficacy of ML models is science, adopting more than one model evaluation technique provides a more strict standard. Though ML has become increasingly popular, the vast majority of peer reviewers are not familiar with ML model development or evaluation which can hinder their ability to properly assess a ML model's efficacy. Continued use of ML in Earth system science will only help to provide continued scientific progress as long as models are rigorously tested and evaluated and those who are part of the peer review process understand proper ML model development and evaluation techniques for processes with physical constraints.

5.2.2 Föhn winds and ice sheet stability

In Chapter 3 we show that föhn winds on the eastern Antarctic Peninsula (AP) played a critical role in the collapse of the Larsen A and B ice shelves. It is important to put these results in context in terms of global ice shelf stability. The föhn wind regime on the AP is anomalous with respect to wind associated melt quantity. On the two collapsed ice shelves of the eastern AP, Larsen A and B, föhn wind-induced melt represented up to 60% of the total annual melt in regions influenced by föhn jets. No other ice shelves on either the GIS or AIS receive wind associated melt that represents such a large portion of total melt. So, while Chapter 3 concludes that enhanced surface melt on the ice shelves and the northwesterly wind direction pushing sea ice away from the calving front provides a better understanding of the collapse of Larsen A and B, it may not necessarily clarify whether additional ice shelves are susceptible to collapse in the future.

Chapter 3 however, sheds light on the limits of surface melt and the many interconnected systems that drive ice shelf stability. Surface melt for example has been theorized to directly impact ice shelf stability through hydrofracture, yet plenty of ice shelves experience firn densification that supports surface melt ponds, and continue to be stable. Previous model studies and the results from Chapter 3 show that ice shelves with a thickness similar to Larsen A and B, become susceptible to collapse when surface melt lakes reach depths of 3 meters or more, over at least 15% of the total surface area (Banwell et al., 2013, 2014). Understanding the limits of ice shelf thickness, hydrofracture susceptibility, and meltwater shear loads, makes it possible to create dynamical ice models that use these limits to better understand instability, which would be a valuable future direction of this research. Additionally, we can expand on this understanding, and couple the many systems

that affect stability such as sea ice and wave action to take future models a step farther in understanding ice shelf stability.

Recent work published by Wille et al., 2022, identified the role of atmospheric rivers in ice shelf stability, where the transport of warm and moist subtropical air through atmospheric rivers leads to enhanced surface temperatures and melt. On the AP atmospheric rivers can cause intense föhn wind events that lead to enhanced surface melt rates (Bozkurt et al., 2018). This was the case during the collapse of the Larsen A ice shelf in 1995, however only a small number of studies evaluate this relationship on an even smaller number of atmospheric rivers. Future research is needed to better understand how often atmospheric rivers lead to föhn events, if these events have increased, and how climate change will alter moisture transport and atmospheric rivers as future temperatures increase.

Finally, one question still unanswered is why the Larsen A and B ice shelves did not collapse prior to 1995 and 2002, considering föhn winds and associated melt were likely present prior to the 1970's. I theorize that a "perfect storm" of global warming impacts, föhn winds, a lack of sea ice, and large ocean waves occurred at the same time to cause collapse. Prior to the collapse of both ice shelves, enhanced surface and basal melt (due to global warming) thinned the ice shelves. Long-term thinning, enhanced surface temperatures, strong föhn events, little sea ice, and strong storms that produce large period ocean swells may have never occurred simultaneously during the lifetimes of Larsen A and B. In this context, sudden ice shelf collapse seems to be almost inevitable because the ice shelves may never have been weaker. As ice dynamical models become more complex,

future research will be able to use our understanding and quantification of föhn-induced melt to partition how important föhn winds were/are to collapse. By using future predictions of temperature increases, and by subtracting the impact of föhn winds, future research can test how long it would take for the Larsen A and B ice shelves to slowly recede and disintegrate without the impact of föhn winds, lack of sea ice, and ocean swells,, which may ultimately shed light on the role of föhn winds and ice shelf stability.

5.2.3 Wind associated melt on the GIS and AIS

In Chapter 4 we quantify katabatic wind associated melt and the long term melt trends for the GIS and AIS. It is clear that katabatic associated melt plays a significant role in the surface melt regime of the GIS and a less significant role on the AIS. When considering the total surface melt on the GIS representing about 7 mm of global sea level rise, katabatic associated melt represents about 2.5 mm of global sea level rise without considering the dynamical changes. Contrast that with katabatic associated melt on the AIS which has significantly less total surface melt constituting about 1 mm global sea level rise of which katabatic associated melt only constitutes 0.2 mm sea level rise without considering dynamical alterations. Even if the ice dynamical changes associated with surface melt, which is hard to quantify currently, is added to the contribution of katabatic associated melt to sea level rise, mass loss on the AIS is significantly over-shadowed by the impact of warm ocean water and basal melt that alters ice dynamics on the ice shelves surrounding the AIS. The importance of identifying all mechanisms for mass-loss should not be overlooked, though katabatic associated melt is clearly a significant driver of mass-loss on the GIS.

Future research may help to provide more answers as to how surface melt associated with katabatic winds on the GIS and AIS will change with climate. Currently katabatic associated melt trends on the GIS suggest that the contribution of total melt that katabatic associated melt currently represents will decrease. However, surface temperatures will warm on the GIS which will reduce the strength of katabatic flow. However, warmer temperatures could also increase katabatic associated melt by making it easier for katabatic flow to cause melt even with decreased katabatic flow strength. Additionally, future research studies are necessary to understand how the steepening of the ice sheet margins for both the GIS and AIS will affect the formation of katabatic flow.

REFERENCES

Abram, N. J., Mulvaney, R., Vimeux, F., Phipps, S. J., Turner, J. and England, M. H.: Evolution of the Southern Annular Mode during the past millennium, Nat. Clim. Chang., 4(7), 564–569, doi:10.1038/nclimate2235, 2014.

Adusumilli, S., Fricker, H. A., Siegfried, M. R., Padman, L., Paolo, F. S. and Ligtenberg, S. R. M.: Variable Basal Melt Rates of Antarctic Peninsula Ice Shelves, 1994–2016, Geophys. Res. Lett., 45(9), 4086–4095, doi:10.1002/2017GL076652, 2018.

Alley, K. E., Scambos, T. A., Miller, J. Z., Long, D. G. and MacFerrin, M.: Quantifying vulnerability of Antarctic ice shelves to hydrofracture using microwave scattering properties, Remote Sens. Environ., 210, 297–306, doi:10.1016/j.rse.2018.03.025, 2018.

Andersen, M. L., Stenseng, L., Skourup, H., Colgan, W., Khan, S. A., Kristensen, S. S., Andersen, S. B., Box, J. E., Ahlstrøm, A. P., Fettweis, X. and Forsberg, R.: Basin-scale partitioning of Greenland ice sheet mass balance components (2007-2011), Earth Planet. Sci. Lett., 409, 89–95, doi:10.1016/j.epsl.2014.10.015, 2015.

Auger, M., Morrow, R., Kestenare, E., Sallée, J. B. and Cowley, R.: Southern Ocean in-situ temperature trends over 25 years emerge from interannual variability, Nat. Commun., 12(1), doi:10.1038/s41467-020-20781-1, 2021.

Banwell, A. F., Caballero, M., Arnold, N. S., Glasser, N. F., Cathles, L. Mac and MacAyeal, D. R.: Supraglacial lakes on the Larsen B ice shelf, Antarctica, and at Paakitsoq, West Greenland: A comparative study, Ann. Glaciol., 55(66), 1–8, doi:10.3189/2014AoG66A049, 2014.

Banwell, A. F., MacAyeal, D. R. and Sergienko, O. V.: Breakup of the Larsen B Ice Shelf triggered by chain reaction drainage of supraglacial lakes, Geophys. Res. Lett., 40(22), 5872–5876, doi:10.1002/2013GL057694, 2013.

Banwell, A. F., Willis, I. C., Macdonald, G. J., Goodsell, B. and MacAyeal, D. R.: Direct measurements of ice-shelf flexure caused by surface meltwater ponding and drainage, Nat. Commun., 10(1), doi:10.1038/s41467-019-08522-5, 2019.

Banwell, A. F., Willis, I. C., MacDonald, G. J., Goodsell, B., Mayer, D. P., Powell, A. and MacAyeal, D. R.: Calving and rifting on the McMurdo Ice Shelf, Antarctica, Ann. Glaciol., 58(75), 78–87, doi:10.1017/aog.2017.12, 2017.

Bell, R. E., Banwell, A. F., Trusel, L. D. and Kingslake, J.: Antarctic surface hydrology and impacts on ice-sheet mass balance, Nat. Clim. Chang., 8(12), 1044–1052, doi:10.1038/s41558-018-0326-3, 2018.

Bevan, S. L., Luckman, A., Hubbard, B., Kulessa, B., Ashmore, D., Kuipers Munneke, P., O'Leary, M., Booth, A., Sevestre, H. and McGrath, D.: Centuries of intense surface melt on Larsen C Ice Shelf, Cryosphere, doi:10.5194/tc-11-2743-2017, 2017.

Bevan, S. L., Luckman, A. J., Kuipers Munneke, P., Hubbard, B., Kulessa, B. and Ashmore, D. W.: Decline in Surface Melt Duration on Larsen C Ice Shelf Revealed by The Advanced Scatterometer (ASCAT), Earth Sp. Sci., 5(10), 578–591, doi:10.1029/2018EA000421, 2018.

Borstad, C., Khazendar, A., Scheuchl, B., Morlighem, M., Larour, E. and Rignot, E.: A constitutive framework for predicting weakening and reduced buttressing of ice shelves based on observations of the progressive deterioration of the remnant Larsen B Ice Shelf, Geophys. Res. Lett., 43(5), 2027–2035, doi:10.1002/2015GL067365, 2016.

Bozkurt, D., Rondanelli, R., Marín, J. C. and Garreaud, R.: Foehn Event Triggered by an Atmospheric River Underlies Record-Setting Temperature Along Continental Antarctica, J. Geophys. Res. Atmos., doi:10.1002/2017JD027796, 2018.

Bozkurt, D., Bromwich, D. H., Carrasco, J., Hines, K. M., Maureira, J. C. and Rondanelli, R.: Recent Near-surface Temperature Trends in the Antarctic Peninsula from Observed, Reanalysis and Regional Climate Model Data, Adv. Atmos. Sci., 37(5), 477–493, doi:10.1007/s00376-020-9183-x, 2020.

Bozkurt, D., Bromwich, D. H., Carrasco, J. and Rondanelli, R.: Temperature and precipitation projections for the Antarctic Peninsula over the next two decades: contrasting global and regional climate model simulations, Clim. Dyn., doi:10.1007/s00382-021-05667-2, 2021.

Braun, M. and Humbert, A.: Recent retreat of wilkins ice shelf reveals new insights in ice shelf breakup mechanisms, IEEE Geosci. Remote Sens. Lett., 6(2), 263–267, doi:10.1109/LGRS.2008.2011925, 2009.

Bromwich, D. H. and Kurtz, D. D.: Katabatic wind forcing of the Terra Nova Bay polynya., J. Geophys. Res., 89(C3), 3561–3572, doi:10.1029/JC089iC03p03561, 1984.

Bromwich, D. H.: An Extraordinary Katabatic Wind Regime at Terra Nova Bay, Antarctica, Mon. Weather Rev., 117 [online] Available from: https://journals.ametsoc.org/doi/abs/10.1175/1520-0493(1989)117%3C0688:AEKWRA%3E2.0.CO%3B2, 1988.

Burton, J. C., Cathles, L. Mac and Wilder, W. G.: The role of cooperative iceberg capsize in ice-shelf disintegration, Ann. Glaciol., 54(63), 84–90, doi:10.3189/2013AoG63A436, 2013.

Cape, M. R., Vernet, M., Skvarca, P., Marinsek, S., Scambos, T. and Domack, E.: Foehn winds link climate-driven warming to ice shelf evolution in Antarctica, J. Geophys. Res., doi:10.1002/2015JD023465, 2015.

Cape, M. R., Vernet, M., Kahru, M. and Spreen, G.: Polynya dynamics drive primary production in the Larsen A and B embayments following ice shelf collapse, J. Geophys. Res. Ocean., 119(1), 572–594, doi:10.1002/2013JC009441, 2014.

Carrasco, J. F., Bozkurt, D. and Cordero, R. R.: A review of the observed air temperature in the Antarctic Peninsula. Did the warming trend come back after the early 21st hiatus?, Polar Sci., 28, doi:10.1016/j.polar.2021.100653, 2021.

Cook, A. J. and Vaughan, D. G.: Ice shelf changes on the Antarctic Peninsula Overview of areal changes of the ice shelves on the Antarctic Peninsula over the past 50 years Ice shelf changes on the Antarctic Peninsula, TCD, 3, 579–630 [online] Available from: www.the-cryosphere-discuss.net/3/579/2009/, 2009.

Datta, R. T., Tedesco, M., Fettweis, X., Agosta, C., Lhermitte, S., Lenaerts, J. T. M. and Wever, N.: The Effect of Foehn-Induced Surface Melt on Firn Evolution Over the Northeast Antarctic Peninsula, Geophys. Res. Lett., 2018GL080845, doi:10.1029/2018GL080845, 2019.

Davis, A. M. J. and Mcnider, R. T.: The Development of Antarctic Katabatic Winds and Implications for the Coastal Ocean, J. Atmos. Sci., 54, 1248–1261, 1997.

Dee, D. P., Uppala, S. M., Simmons, A. J., Berrisford, P., Poli, P., Kobayashi, S., Andrae, U., Balmaseda, M. A., Balsamo, G., Bauer, P., Bechtold, P., Beljaars, A. C. M., van de Berg, L., Bidlot, J., Bormann, N., Delsol, C., Dragani, R., Fuentes, M., Geer, A. J., Haimberger, L., Healy, S. B., Hersbach, H., Hólm, E. V., Isaksen, L., Kållberg, P., Köhler, M., Matricardi, M., Mcnally, A. P., Monge-Sanz, B. M., Morcrette, J. J., Park, B. K., Peubey, C., de Rosnay, P., Tavolato, C., Thépaut, J. N. and Vitart, F.: The ERA-Interim reanalysis: Configuration and performance of the data assimilation system, Q. J. R. Meteorol. Soc., 137(656), 553–597, doi:10.1002/qj.828, 2011.

Depoorter, M. A., Bamber, J. L., Griggs, J. A., Lenaerts, J. T. M., Ligtenberg, S. R. M., Van Den Broeke, M. R. and Moholdt, G.: Calving fluxes and basal melt rates of Antarctic ice shelves, Nature, 502(7469), 89–92, doi:10.1038/nature12567, 2013.

Doake, C. S. M., Corr, H. F. J., Rott, H., Skvarca, P. and Young, N. W.: Breakup and conditions for stability of the northern Larsen Ice Shelf, Antarctica, Nature, 391, 778–780, 1988.ECMWF: IFS Documentation CY33R1 - Part IV: Physical Processes, in IFS Documentation CY33R1, vol. 4., 2009.

Elvidge, A. D., Kuipers Munneke, P., King, J. C., Renfrew, I. A. and Gilbert, E.: Atmospheric Drivers of Melt on Larsen C Ice Shelf: Surface Energy Budget Regimes and the Impact of Foehn, J. Geophys. Res. Atmos., 125(17), doi:10.1029/2020JD032463, 2020.

Elvidge, A. D. and Renfrew, I. A.: The causes of foehn warming in the lee of mountains, Bull. Am. Meteorol. Soc., doi:10.1175/BAMS-D-14-00194.1, 2016.Elvidge, A. D., Renfrew, I. A., King, J. C., Orr, A. and Lachlan-Cope, T. A.: Foehn warming distributions in nonlinear and linear flow regimes: A focus on the Antarctic Peninsula, Q. J. R. Meteorol. Soc., doi:10.1002/qj.2489, 2016.

Elvidge, A. D., Renfrew, I. A., King, J. C., Orr, A., Lachlan-Cope, T. A., Weeks, M. and Gray, S. L.: Foehn jets over the Larsen C Ice Shelf, Antarctica, Q. J. R. Meteorol. Soc., 141(688), 698–713, doi:10.1002/qj.2382, 2015.

Enderlin, E. M., Howat, I. M., Jeong, S., Noh, M. J., Van Angelen, J. H. and Van Den Broeke, M. R.: An improved mass budget for the Greenland ice sheet, Geophys. Res. Lett., 41(3), 866–872, doi:10.1002/2013GL059010, 2014.

Fettweis, X., Box, J. E., Agosta, C., Amory, C., Kittel, C., Lang, C., Van As, D., Machguth, H. and Gallée, H.: Reconstructions of the 1900-2015 Greenland ice sheet surface mass balance using the regional climate MAR model, Cryosphere, 11(2), 1015–1033, doi:10.5194/tc-11-1015-2017, 2017.

Glasser, N. F. and Scambos, T. A.: A structural glaciological analysis of the 2002 Larsen B ice-shelf collapse, J. Glaciol., 54(184), 3–16, doi:10.3189/002214308784409017, 2008.

Glasser, N. F., Kulessa, B., Luckman, A., Jansen, D., King, E. C., Sammonds, P. R., Scambos, T. A. and Jezek, K. C.: Surface structure and stability of the Larsen C ice shelf, Antarctic Peninsula., 2009.

Grazioli, J., Madeleine, J. B., Gallée, H., Forbes, R. M., Genthon, C., Krinner, G. and Berne, A.: Katabatic winds diminish precipitation contribution to the Antarctic ice mass balance, Proc. Natl. Acad. Sci. U. S. A., 114(41), 10858–10863, doi:10.1073/pnas.1707633114, 2017.

Grosvenor, D. P., King, J. C., Choularton, T. W. and Lachlan-Cope, T.: Downslope föhn winds over the antarctic peninsula and their effect on the larsen ice shelves, Atmos. Chem. Phys., 14(18), 9481–9509, doi:10.5194/acp-14-9481-2014, 2014.

Gudmundsson, G. H.: Ice-shelf buttressing and the stability of marine ice sheets, Cryosphere, 7(2), 647–655, doi:10.5194/tc-7-647-2013, 2013.

Hanna, E., Navarro, F. J., Pattyn, F., Domingues, C. M., Fettweis, X., Ivins, E. R., Nicholls, R. J., Ritz, C., Smith, B., Tulaczyk, S., Whitehouse, P. L. and Jay Zwally, H.: Ice-sheet mass balance and climate change, Nature, 498(7452), 51–59, doi:10.1038/nature12238, 2013.

Heinemann, G.: The KABEG'97 field experiment: An aircraft-based study of Katabatic wind dynamics over the Greenland ice sheet, Boundary-Layer Meteorol., doi:10.1023/A:1002009530877, 1999.

Heinemann, G., Glaw, L. and Willmes, S.: A Satellite-Based Climatology of Wind-Induced Surface Temperature Anomalies for the Antarctic, Remote Sens., 11(13), 1539, doi:10.3390/rs11131539, 2019.

Hofer, S., Tedstone, A. J., Fettweis, X. and Bamber, J. L.: Decreasing cloud cover drives the recent mass loss on the Greenland Ice Sheet, Meteorology [online] Available from: https://www.science.org, 2017.

Holland, P. R., Corr, H. F. J., Pritchard, H. D., Vaughan, D. G., Arthern, R. J., Jenkins, A. and Tedesco, M.: The air content of Larsen Ice Shelf, Geophys. Res. Lett., doi:10.1029/2011GL047245, 2011.

Hubbard, B., Luckman, A., Ashmore, D. W., Bevan, S., Kulessa, B., Kuipers Munneke, P., Philippe, M., Jansen, D., Booth, A., Sevestre, H., Tison, J. L., O'Leary, M. and Rutt, I.: Massive subsurface ice formed by refreezing of ice-shelf melt ponds, Nat. Commun., 7, doi:10.1038/ncomms11897, 2016.

JOSEPH JOHN MURPHY: The Greenland Foehn, Nature, 16, 340–341 [online] Available from: https://www.nature.com/articles/016340b0, 1877.

King, J. C., Gadian, A., Kirchgaessner, A., Kuipers Munneke, P., Lachlan-Cope, T. A., Orr, A., Reijmer, C., van den Broeke, M. R., van Wessem, J. M. and Weeks, M.: Validation of the summertime surface energy budget of Larsen C Ice Shelf (Antarctica) as represented in three high-resolution atmospheric models, J. Geophys. Res., 120(4), 1335–1347, doi:10.1002/2014JD022604, 2015.

King, J. C., Kirchgaessner, A., Bevan, S., Elvidge, A. D., Kuipers Munneke, P., Luckman, A., Orr, A., Renfrew, I. A. and van den Broeke, M. R.: The Impact of Föhn Winds on Surface Energy Balance During the 2010–2011 Melt Season Over Larsen C Ice Shelf, Antarctica, J. Geophys. Res. Atmos., doi:10.1002/2017JD026809, 2017.

Kirchgaessner, A., King, J. C. and Anderson, P. S.: The Impact of Föhn Conditions Across the Antarctic Peninsula on Local Meteorology Based on AWS Measurements, J. Geophys. Res. Atmos., 126(4), doi:10.1029/2020JD033748, 2021.

Klein, T. and Heinemann, G.: Interaction of katabatic winds and mesocyclones near the eastern coast of Greenland, Meteorol. Appl., 9(4), 407–422, doi:10.1017/S1350482702004036, 2002.

Konrad, H., Shepherd, A., Gilbert, L., Hogg, A. E., McMillan, M., Muir, A. and Slater, T.: Net retreat of Antarctic glacier grounding lines, Nat. Geosci., 11(4), 258–262, doi:10.1038/s41561-018-0082-z, 2018.

Kuipers Munneke, P., Luckman, A. J., Bevan, S. L., Smeets, C. J. P. P., Gilbert, E., van den Broeke, M. R., Wang, W., Zender, C., Hubbard, B., Ashmore, D., Orr, A., King, J. C. and Kulessa, B.: Intense Winter Surface Melt on an Antarctic Ice Shelf, Geophys. Res. Lett., doi:10.1029/2018GL077899, 2018.

Kuipers Munneke, P., Picard, G., Van Den Broeke, M. R., Lenaerts, J. T. M. and Van Meijgaard, E.: Insignificant change in Antarctic snowmelt volume since 1979, Geophys. Res. Lett., doi:10.1029/2011GL050207, 2012.

Kuipers Munneke, P., Van Den Broeke, M. R., King, J. C., Gray, T. and Reijmer, C. H.: Near-surface climate and surface energy budget of Larsen C ice shelf, Antarctic Peninsula, Cryosphere, 6(2), 353–363, doi:10.5194/tc-6-353-2012, 2012.

Laffin, M. K., Zender, C. S., Singh, S., Van Wessem, J. M., Smeets, C. J. P. P. and Reijmer, C. H.: Climatology and Evolution of the Antarctic Peninsula Föhn Wind-Induced Melt Regime From 1979–2018, J. Geophys. Res. Atmos., 126(4), doi:10.1029/2020JD033682, 2021.

Laffin, M. K., Zender, C. S., van Wessem, M. and Marinsek, S.: The role of föhn winds in eastern Antarctic Peninsula rapid ice shelf collapse, Cryosph., 16(4), 1369–1381, doi:10.5194/tc-16-1369-2022, 2022.

Larour, E., Rignot, E., Poinelli, M. and Scheuchl, B.: Physical processes controlling the rifting of Larsen C Ice Shelf, Antarctica, prior to the calving of iceberg A68, Proc. Natl. Acad. Sci. U. S. A., 118(40), doi:10.1073/pnas.2105080118, 2021.

Le Toumelin, L., Amory, C., Favier, V., Kittel, C., Hofer, S., Fettweis, X., Gallee, H. and Kayetha, V.: Sensitivity of the surface energy budget to drifting snow as simulated by MAR in coastal Adelie Land, Antarctica, Cryosphere, 15(8), 3595–3614, doi:10.5194/tc-15-3595-2021, 2021.

Leeson, A. A., Forster, E., Rice, A., Gourmelen, N. and van Wessem, J. M.: Evolution of Supraglacial Lakes on the Larsen B Ice Shelf in the Decades Before it Collapsed, Geophys. Res. Lett., 47(4), doi:10.1029/2019GL085591, 2020.

Leeson, A. A., Van Wessem, J. M., Ligtenberg, S. R. M., Shepherd, A., Van Den Broeke, M. R., Killick, R., Skvarca, P., Marinsek, S. and Colwell, S.: Regional climate of the Larsen B embayment 1980-2014, J. Glaciol., 63(240), 683–690, doi:10.1017/jog.2017.39, 2017.

Lenaerts, J. T. M., Lhermitte, S., Drews, R., Ligtenberg, S. R. M., Berger, S., Helm, V., Smeets, C. J. P. P., Broeke, M. R. V. Den, Van De Berg, W. J., Van Meijgaard, E., Eijkelboom, M., Eisen, O. and Pattyn, F.: Meltwater produced by wind-albedo interaction stored in an East Antarctic ice shelf, Nat. Clim. Chang., doi:10.1038/nclimate3180, 2017.

Lhermitte, S., Sun, S., Shuman, C., Wouters, B., Pattyn, F., Wuite, J., Berthier, E. and Nagler, T.: Damage accelerates ice shelf instability and mass loss in Amundsen Sea Embayment, Sci. Libr. Ser., 117, doi:10.1073/pnas.1912890117/-/DCSupplemental.y, 2020.

Lim, E. P., Hendon, H. H., Arblaster, J. M., Delage, F., Nguyen, H., Min, S. K. and Wheeler, M. C.: The impact of the Southern Annular Mode on future changes in Southern Hemisphere rainfall, Geophys. Res. Lett., 43(13), 7160–7167, doi:10.1002/2016GL069453, 2016.

Luckman, A., Elvidge, A., Jansen, D., Kulessa, B., Kuipers Munneke, P., King, J. and Barrand, N. E.: Surface melt and ponding on Larsen C Ice Shelf and the impact of föhn winds, Antarct. Sci., doi:10.1017/S0954102014000339, 2014.

Massom, R. A., Scambos, T. A., Bennetts, L. G., Reid, P., Squire, V. A. and Stammerjohn, S. E.: Antarctic ice shelf disintegration triggered by sea ice loss and ocean swell, Nature, 558(7710), 383–389, doi:10.1038/s41586-018-0212-1, 2018.

McGrath, D., Steffen, K., Holland, P. R., Scambos, T., Rajaram, H., Abdalati, W. and Rignot, E.: The structure and effect of suture zones in the Larsen C Ice Shelf, Antarctica, J. Geophys. Res. Earth Surf., 119(3), 588–602, doi:10.1002/2013JF002935, 2014.

Melchior Van Wessem, J., Jan Van De Berg, W., Noël, B. P. Y., Van Meijgaard, E., Amory, C., Birnbaum, G., Jakobs, C. L., Krüger, K., Lenaerts, J. T. M., Lhermitte, S., Ligtenberg, S. R. M., Medley, B., Reijmer, C. H., Van Tricht, K., Trusel, L. D., Van Ulft, L. H., Wouters, B., Wuite, J. and Van Den Broeke, M. R.: Modelling the climate and surface mass balance of polar ice sheets using RACMO2 - Part 2: Antarctica (1979-2016), Cryosphere, 12(4), 1479–1498, doi:10.5194/tc-12-1479-2018, 2018.

Mioduszewski, J. R., Rennermalm, A. K., Hammann, A., Tedesco, M., Noble, E. U., Stroeve, J. C. and Mote, T. L.: Atmospheric drivers of greenland surface melt revealed by self-organizing maps, J. Geophys. Res., 121(10), 5095–5114, doi:10.1002/2015JD024550, 2016.

Morris, E. M. and Vaughan, D. G.: Spatial and Temporal Variation of Surface Temperature on the Antarctic Peninsula and the Limit of Viability of Ice Shelves, Antarct. Res. Ser., 79, 61–68, doi:10.1029/079ARS05, 2003.

Mulvaney, R., Abram, N. J., Hindmarsh, R. C. A., Arrowsmith, C., Fleet, L., Triest, J., Sime, L. C., Alemany, O. and Foord, S.: Recent Antarctic Peninsula warming relative to Holocene climate and ice-shelf history, Nature, 489(7414), 141–144, doi:10.1038/nature11391, 2012.

Munneke, P. K., Ligtenberg, S. R. M., Van Den Broeke, M. R. and Vaughan, D. G.: Firn air depletion as a precursor of Antarctic ice-shelf collapse, J. Glaciol., 60(220), 205–214, doi:10.3189/2014JoG13J183, 2014.

Murphy, B. F., and I. S. (1993): An analysis of strong wind events simulated in a GCM near Casey in the Antarctic, Mon. Weather Rev., (121), 522–534, n.d.Nicolas, J. P., Wang, S., Bromwich, D. H., Zou, X. and Montenegro, A.: West Antarctic surface melt event of January 2016 facilitated by föhn warming, Q. J. R. Meteorol. Soc., doi:10.1002/qj.3460, 2018.

Noël, B., Van De Berg, W. J., Lhermitte, S. and Van Den Broeke, M. R.: Rapid ablation zone expansion amplifies north Greenland mass loss. [online] Available from: http://advances.sciencemag.org/, 2019.

Nylen, T. H., Fountain, A. G. and Doran, P. T.: Climatology of katabatic winds in the McMurdo dry valleys, southern Victoria Land, Antarctica, J. Geophys. Res. Atmos., 109(D3), n/a-n/a, doi:10.1029/2003JD003937, 2004.

Palm, S. P., Kayetha, V., Yang, Y. and Pauly, R.: Blowing snow sublimation and transport over Antarctica from 11 years of CALIPSO observations, Cryosphere, 11(6), 2555–2569, doi:10.5194/tc-11-2555-2017, 2017.

Parish, T. R. and Cassano, J. J.: Forcing of the Wintertime Antarctic Boundary Layer Winds from the NCEP–NCAR Global Reanalysis, n.d.Parish, T. R. and Cassano, J. J.: The Role of Katabatic Winds on the Antarctic Surface Wind Regime, 2003.

Parish, T. R. and Bromwich, D. H.: The Inversion Wind Pattern over West Antarctica, Mon. Weather Rev., 114 [online] Available from: https://journals.ametsoc.org/doi/10.1175/1520-0493%281986%29114%3C0849%3ATIWPOW%3E2.0.CO%3B2, 1986.

Polashenski, C., Golden, K. M., Perovich, D. K., Skyllingstad, E., Arnsten, A., Stwertka, C. and Wright, N.: Percolation blockage: A process that enables melt pond formation on first year Arctic sea ice, J. Geophys. Res. Ocean., 122(1), 413–440, doi:10.1002/2016JC011994, 2017.

Pollard, D., DeConto, R. M. and Alley, R. B.: Potential Antarctic Ice Sheet retreat driven by hydrofracturing and ice cliff failure, Earth Planet. Sci. Lett., 412, 112–121, doi:10.1016/j.epsl.2014.12.035, 2015.

Pritchard, H. D., Ligtenberg, S. R. M., Fricker, H. A., Vaughan, D. G., Van Den Broeke, M. R. and Padman, L.: Antarctic ice-sheet loss driven by basal melting of ice shelves, Nature, 484(7395), 502–505, doi:10.1038/nature10968, 2012.

Qiao, G., Li, Y., Guo, S. and Ye, W.: Evolving instability of the scar inlet ice shelf based on sequential landsat images spanning 2005-2018, Remote Sens., 12(1), doi:10.3390/RS12010036, 2020.

Rack, W. and Rott, H.: Pattern of retreat and disintegration of the Larsen B ice shelf, Antarctic Peninsula, Ann. Glaciol. , 39, 505–510 [online] Available from: https://www.cambridge.org/core., 2004.

Rignot, E., Jacobs, S., Mouginot, B. and Scheuchl, B.: Ice-Shelf Melting Around Antarctica, Science (80-.)., 341(6143), 263–266, doi:10.1126/science.1237966, 2013.

Rignot, E., Casassa, G., Gogineni, P., Krabill, W., Rivera, A. and Thomas, R.: Accelerated ice discharge from the Antarctic Peninsula following the collapse of Larsen B ice shelf, Geophys. Res. Lett., 31(18), doi:10.1029/2004GL020697, 2004.

Rignot, E., Mouginot, J., Morlighem, M., Seroussi, H. and Scheuchl, B.: Widespread, rapid grounding line retreat of Pine Island, Thwaites, Smith, and Kohler glaciers, West Antarctica, from 1992 to 2011, Geophys. Res. Lett., 41(10), 3502–3509, doi:10.1002/2014GL060140, 2014.

Rignot, E., Bamber, J. L., Van Den Broeke, M. R., Davis, C., Li, Y., Van De Berg, W. J. and Van Meijgaard, E.: Recent Antarctic ice mass loss from radar interferometry and regional climate modelling, Nat. Geosci., 1(2), 106–110, doi:10.1038/ngeo102, 2008.

Robel, A. A. and Banwell, A. F.: A Speed Limit on Ice Shelf Collapse Through Hydrofracture, Geophys. Res. Lett., 46(21), 12092–12100, doi:10.1029/2019GL084397, 2019.

Rott, H., Rack, W., Nagler, T. and Skvarca, P.: Climatically induced retreat and collapse of norther Larsen Ice Shelf, Antarctic Peninsula, Ann. Glaciol., 27, 86–92, doi:10.3189/s0260305500017262, 1998.

Rott, H., Skvarca, P. and Nagler, T.: Rapid Collapse of Northern Larsen Ice Shelf, Antarctica, Am. Assoc. Adv. Sci., 271(5250), 788–792 [online] Available from: https://www.jstor.org/stable/2889887 (Accessed 6 April 2022), 1996.

Sandhäger, H., Rack, W. and Jansen, D.: Model investigations of Larsen B Ice Shelf dynamics prior to the breakup. [online] Available from: http://www.uib.no/People/ngfls/frisp/Rep16/sandhageretal.pdf, 2005.

Scambos, T. A., Bohlander, J. A., Shuman, C. A. and Skvarca, P.: Glacier acceleration and thinning after ice shelf collapse in the Larsen B embayment, Antarctica, Geophys. Res. Lett., 31(18), doi:10.1029/2004GL020670, 2004.

Scambos, T. A., Hulbe, C., Fahnestock, M. and Bohlander, J.: The link between climate warming and break-up of ice shelves in the Antarctic Peninsula, J. Glaciol., 46(154), 516–530, doi:10.3189/172756500781833043, 2000.

Scambos, T., Hulbe, C. and Fahnestock, M.: Climate-Induced Ice Shelf Disintegration in the Antarctic Peninsula, pp. 79–92., 2003.Schodlok, M. P., Menemenlis, D. and Rignot, E. J.: Ice shelf basal melt rates around Antarctica from simulations and observations, J. Geophys. Res. Ocean., 121(2), 1085–1109, doi:10.1002/2015JC011117, 2016.

Slater, T., Lawrence, I. R., Otosaka, I. N., Shepherd, A., Gourmelen, N., Jakob, L., Tepes, P., Gilbert, L. and Nienow, P.: Review article: Earth's ice imbalance, Cryosphere, 15(1), 233–246, doi:10.5194/tc-15-233-2021, 2021.

Speirs, J. C., Steinhoff, D. F., McGowan, H. A., Bromwich, D. H. and Monaghan, A. J.: Foehn winds in the McMurdo Dry Valleys, Antarctica: The origin of extreme warming events, J. Clim., doi:10.1175/2010JCLI3382.1, 2010.

Straneo, F. and Heimbach, P.: North Atlantic warming and the retreat of Greenland's outlet glaciers, Nature, 504(7478), 36–43, doi:10.1038/nature12854, 2013.

Tedesco, M., Fettweis, X., Mote, T., Wahr, J., Alexander, P., Box, J. E. and Wouters, B.: Evidence and analysis of 2012 Greenland records from spaceborne observations, a regional climate model and reanalysis data, Cryosphere, 7(2), 615–630, doi:10.5194/tc-7-615-2013, 2013.

The IMBIE team: Mass balance of the Greenland Ice Sheet from 1992 to 2018, Nature, 579(7798), 233–239, doi:10.1038/s41586-019-1855-2, 2020.

The IMBIE team: Mass balance of the Antarctic Ice Sheet from 1992 to 2017, Nature, 558, 219–222, doi:10.1038/s41586, 2018.

Trusel, L. D., Frey, K. E., Das, S. B., Karnauskas, K. B., Kuipers Munneke, P., Van Meijgaard, E. and Van Den Broeke, M. R.: Divergent trajectories of Antarctic surface melt under two twenty-first-century climate scenarios, Nat. Geosci., 8(12), 927–932, doi:10.1038/ngeo2563, 2015.

Trusel, L. D., Frey, K. E., Das, S. B., Munneke, P. K. and Van Den Broeke, M. R.: Satellite-based estimates of Antarctic surface meltwater fluxes, Geophys. Res. Lett., 40(23), 6148–6153, doi:10.1002/2013GL058138, 2013.

Turner, J., Lu, H., White, I., King, J. C., Phillips, T., Hosking, J. S., Bracegirdle, T. J., Marshall, G. J., Mulvaney, R. and Deb, P.: Absence of 21st century warming on Antarctic Peninsula consistent with natural variability, Nature, 535(7612), 411–415, doi:10.1038/nature18645, 2016.

Turton, J. V., Kirchgaessner, A., Ross, A. N. and King, J. C.: Does high-resolution modelling improve the spatial analysis of föhn flow over the Larsen C Ice Shelf?, Weather, 72(7), doi:10.1002/wea.3028, 2017.

Turton, J. V., Kirchgaessner, A., Ross, A. N. and King, J. C.: The spatial distribution and temporal variability of föhn winds over the Larsen C ice shelf, Antarctica, Q. J. R. Meteorol. Soc., doi:10.1002/qj.3284, 2018.

Van Den Broeke, M. R. and Van Lipzig, N. P. M.: Factors Controlling the Near-Surface Wind Field in Antarctica *., 2003.van den Broeke, M.: Strong surface melting preceded collapse of Antarctic Peninsula ice shelf, Geophys. Res. Lett., 32(12), 1–4, doi:10.1029/2005GL023247, 2005.

Van Den Broeke, M. R., Van De Wal, R. S. W. and Wild, M.: Representation of antarctic Katabatic winds in a high-resolution GCM and a note on their climate sensitivity, J. Clim., doi:10.1175/1520-0442(1997)010<3111:ROAKWI>2.0.CO;2, 1997.

Van den Broeke, M., Van As, D., Reijmer, C. and Van de Wal, R.: Sensible heat exchange at the Antarctic snow surface: A study with automatic weather stations, Int. J. Climatol., doi:10.1002/joc.1152, 2005.

Van Wessem, J. M., Reijmer, C. H., Van De Berg, W. J., Van Den Broeke, M. R., Cook, A. J., Van Ulft, L. H. and Van Meijgaard, E.: Temperature and wind climate of the Antarctic Peninsula as simulated by a high-resolution Regional Atmospheric Climate Model, J. Clim., 28(18), 7306–7326, doi:10.1175/JCLI-D-15-0060.1, 2015.

Vaughan, D. G., Marshall, G. J., Connolley, W. M., Parkinson, C., Mulvaney, R., Hodgson, D. A., King, J. C., Pudsey, C. J. and Turner, J.: Recent rapid regional climate warming on the Antarctic Peninsula, Clim. Change, 60(3), 243–274, doi:10.1023/A:1026021217991, 2003.

Vihma, T., Tuovinen, E. and Savijrvi, H.: Interaction of katabatic winds and near-surface temperatures in the Antarctic, J. Geophys. Res. Atmos., 116(21), doi:10.1029/2010JD014917, 2011.

Wang, W., Zender, C. S., van As, D., Fausto, R. S. and Laffin, M. K.: Greenland Surface Melt Dominated by Solar and Sensible Heating, Geophys. Res. Lett., 48(7), doi:10.1029/2020GL090653, 2021.

Wang, X., Zhang, Z., Wang, X., Vihma, T., Zhou, M., Yu, L., Uotila, P. and Sein, D. V.: Impacts of strong wind events on sea ice and water mass properties in Antarctic coastal polynyas, Clim. Dyn., 57(11–12), 3505–3528, doi:10.1007/s00382-021-05878-7, 2021.

Wenta, M. and Cassano, J. J.: The atmospheric boundary layer and surface conditions during katabatic wind events over the Terra Nova bay Polynya, Remote Sens., 12(24), 1–32, doi:10.3390/rs12244160, 2020.

Wiesenekker, J. M., Munneke, P. K., van den Broeke, M. R. and Paul Smeets, C. J. P.: A multidecadal analysis of Föhn winds over Larsen C ice shelf from a combination of observations and modeling, Atmosphere (Basel)., 9(5), doi:10.3390/atmos9050172, 2018.

Xie, Z., Ma, Y., Ma, W., Hu, Z. and Sun, G.: The statistics of blowing snow occurrences from multi-year autonomous snow flux measurements in the French Alps, Cryosph., doi:10.5194/tc-2021-260, 2021.

Zheng, F., Li, J., Clark, R. T. and Nnamchi, H. C.: Simulation and projection of the Southern Hemisphere annular mode in CMIP5 models, J. Clim., 26(24), 9860–9879, doi:10.1175/JCLI-D-13-00204.1, 2013.

APPENDIX A

Supporting Information for Ch. 2: Climatology and evolution of the Antarctic Peninsula föhn wind-induced melt regime from 1979–2018

Table A.1 Föhn classification sensitivity study statistics

Study	AWS 18				AWS 17				AWS 15				AWS 14			
	Föhn Occurence	True Positive	False Positive	False Negative	Föhn Occurence	True Positive	False Positive	False Negative	Föhn Occurence	True Positive	False Positive	False Negative	Föhn Occurence	True Positive	False Positive	False Negative
This Study	771	771	0	0	190	190	0	0	162.5	162.5	0	0	163	163	0	0
Cape et al., 2015	742 (96.2%)	739 (95.8%)	3 (0.4%)	29 (3.8%)	193 (101.6%)	187 (98.4%)	6 (3.2%)	3 (1.6%)	159.2 (98.0%)	152.2 (93.7%)	7 (4.3%)	3.2 (2.0%)	150 (92.0%)	142 (87.1%)	8 (4.9%)	13 (8.0%)
Datta et al., 2018	757 (98.2%)	753 (97.7%)	4 (0.5%)	14 (1.8%)	180 (94.7%)	174 (91.6%)	6 (3.2%)	10 (5.3%)	160.5 (98.8%)	154.5 (95.1%)	6 (3.7%)	2 (1.2%)	159.2 (97.7%)	149 (91.4%)	10.2 (6.3%)	3.7 (2.3%)

Note: Each value is the average number of classified föhn melt event hours per year. Each of the classification methods are compared to this study. True positive represents the methods ability to correctly classify föhn hours defined by this study. False positive represents the methods classification of a föhn event when our model does not classify an event. False negative represents the method did not classify a föhn event when our model did.

Table A.2 Summary of variables used for each dataset.
Bold variables indicate the highest feature weight for each dataset.

ERA5 (Hourly)		RACMO2 (3-hourly)	
Variable	Feature weight	Variable	Feature weight
Time variant variables			
Temperature (K)	**0.174**	**RACMO FonDA**	**0.183**
10m wind gust (m/s)	**0.062**	**Temperature (K)**	**0.105**
ERA5 FonDA	**0.051**	**Skin Temperature (K)**	**0.073**
Month (1-12)	0.041	**Relative Humidity (%)**	**0.072**
Direction to Low pressure (°)	0.038	**Sensible Heat Flux ($W \cdot m^{-2}$)**	**0.058**
Direction to High Pressure (°)	0.037	Latent Heat Flux ($W \cdot m^{-2}$)	0.05
Snow Albedo (0-1)	0.033	Direction to High Pressure (°)	0.046
Runoff (m)	0.033	Wind from Direction (°)	0.043
Ice Temperature (k)	0.032	Wind Speed (m/s)	0.039
Wind from Direction (°)	0.028	Snow Evaporation (m w.e.)	0.036
Skin Temperature (K)	0.027	Direction to Low pressure (°)	0.031
Wind Speed (m/s)	0.019	Longwave Radiation ($W \cdot m^{-2}$)	0.027
Relative Humidity (%)	0.017	Snow Albedo (0-1)	0.021
Sensible Heat Flux ($W \cdot m^{-2}$)	0.016	Distance to low Pressure (km)	0.02
Latent Heat Flux ($W \cdot m^{-2}$)	0.015	Month (1-12)	0.019
Distance to low Pressure (km)	0.015	Distance to high Pressure (km)	0.018
Distance to high Pressure (km)	0.014	Shortwave Radiation ($W \cdot m^{-2}$)	0.015
Evaporation (m w.e.)	0.014	Surface Pressure (hPa)	0.012
Surface Pressure (hPa)	0.013	Hour of the Day (0-24)	0.01
Shortwave Radiation ($W \cdot m^{-2}$)	0.012	Mean Sea Level Pressure (hPa)	0.009

Snow Evaporation (m w.e.)	0.011		
Longwave Radiation ($W \cdot m^{-2}$)	0.011		
Mean Sea Level Pressure (hPa)	0.009		
Cloud Cover (0-1)	0.009		
Hour of the Day (0-24)	0.008		
Snow Depth (m w.e.)	0		
Time invariant variables			
Distance to highest elevation (km)	**0.116**	Distance to highest elevation (km)	0.037
Elevation (m)	**0.049**	Latitude	0.022
Distance to steepest slope (km)	0.032	Longitude	0.021
Slope	0.029	Distance to steepest slope (km)	0.02
Longitude	0.021	Elevation (m)	0.012
Latitude	0.014	Slope	0.001

Table A.3 Machine learning model summary
Each parameter is adjustable in the gradient boosting algorithm through XGBoost.

Dataset	Algorithm	Parameter description
ERA5	Gradient boosting	n_estimators = 826, learning_rate = 0.0673, max_depth = 27, min_child_weight = 3, scale_pos_weight = 43.65, subsample = 0.65, colsample_bylevel = 0.98, colsample_bytree = 0.73, gamma = 0.06, max_delta_step = 1, reg_alpha = 0.028, reg_lambda = 6.3e-09
RACMO2	Gradient boosting	n_estimators = 995, learning_rate = 0.0263, max_depth = 50, min_child_weight = 5, scale_pos_weight = 66.66, subsample = 1.0, colsample_bylevel = 0.09, colsample_bytree = 0.44, gamma = 8.8e-09, max_delta_step = 0, reg_alpha = 1.78e-07, reg_lambda = 1e-09

APPENDIX B

Supporting Information for Ch. 3: The role of föhn winds in Antarctic Peninsula rapid ice shelf collapse

Table B.2 Ice shelf intercomparison to the LBIS. T-statistic was calculated using a two-tailed t-test. Bold values represent ice shelves that are significantly different from the LBIS at the 95% confidence interval.

Surface Melt Production

	Total		Non-föhn		Föhn	
	t-statistic	p-value	t-statistic	p-value	t-statistic	p-value
Larsen A	0.04	0.969	-0.39	0.695	0.54	0.591
SCAR inlet	**2.01**	**0.050**	1.23	0.225	**2.75**	**0.009**
Larsen C (north)	**2.44**	**0.019**	1.60	0.117	**3.18**	**0.003**
Larsen C	**4.57**	**0.000**	**3.99**	**0.000**	**4.73**	**0.000**

Air Temperature

	Total		Non-föhn		Föhn	
	t-statistic	p-value	t-statistic	p-value	t-statistic	p-value
Larsen A	**-5.01**	**0.000**	**-6.19**	**0.000**	**-7.24**	**0.000**
SCAR inlet	**2.90**	**0.006**	**2.13**	**0.039**	**2.20**	**0.033**
Larsen C (north)	**2.29**	**0.027**	1.78	0.082	**4.23**	**0.000**
Larsen C	**6.55**	**0.000**	**6.27**	**0.000**	**8.80**	**0.000**

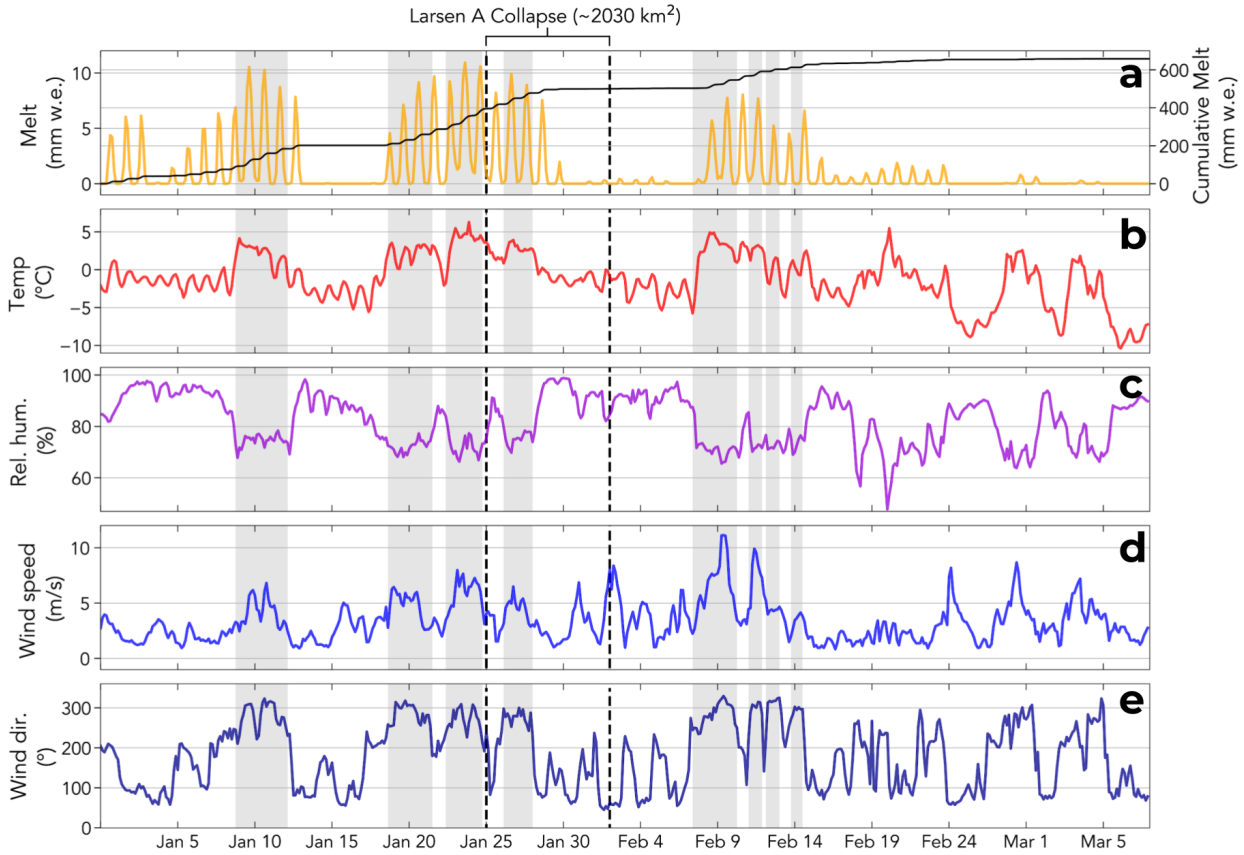

Figure B.1 Time series during the 94/95 melt season averaged over the LAIS. Grey shading indicates the presence of föhn winds. (a) Surface melt production and Cumulative melt (b) Air temperature, (c) Relative Humidity, (d) 10 m Wind Speed, (e) Wind direction. *Note*: Values that occur after the collapse event indicated by the dashed lines are estimates if the ice shelf did not collapse.

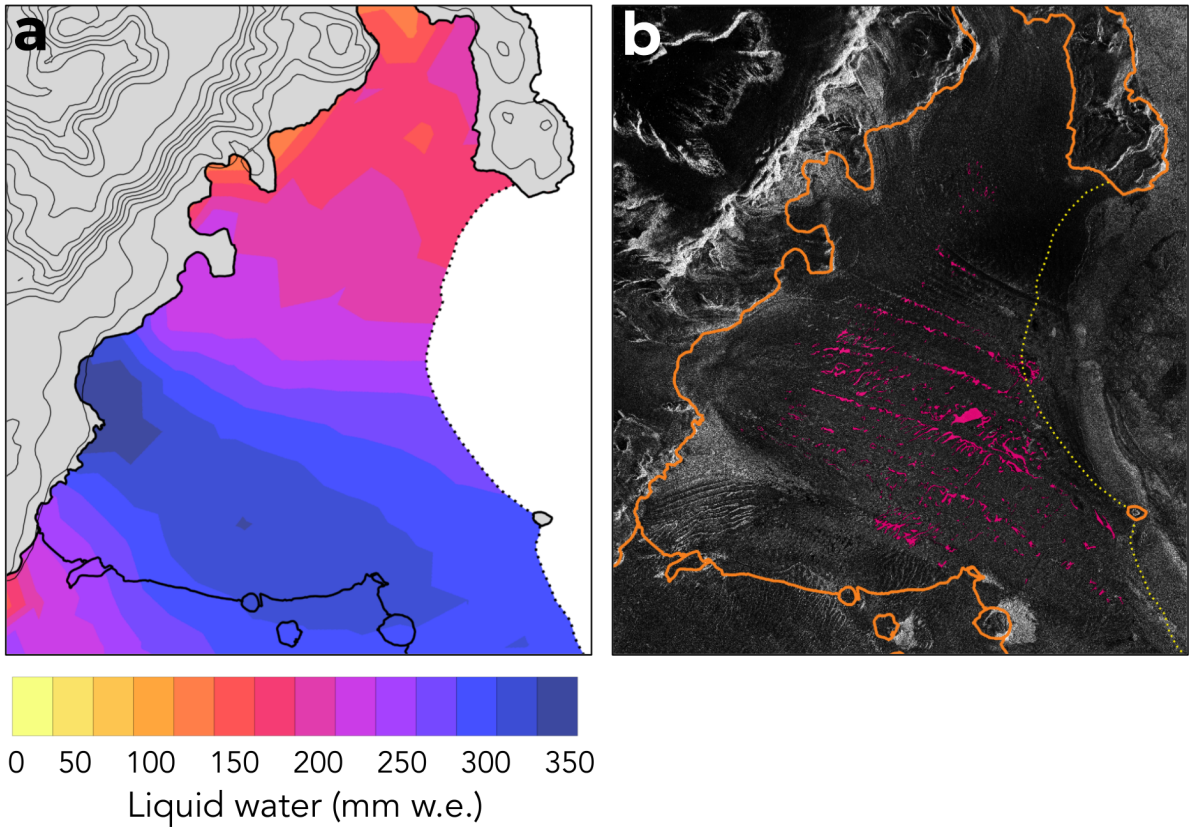

Figure B.2 (**a**) Cumulative surface melt production on the LAIS during the nine-day föhn wind event period, January 18 - 27, 1995 (**b**) Advanced Very High-Resolution Radiometer (AVHRR) image of the LAIS on December 8, 1992, with surface melt lakes identified with pink shading. The solid orange line denotes the grounding line and the dashed yellow line denotes the location of the calving front prior to collapse in January 1995.

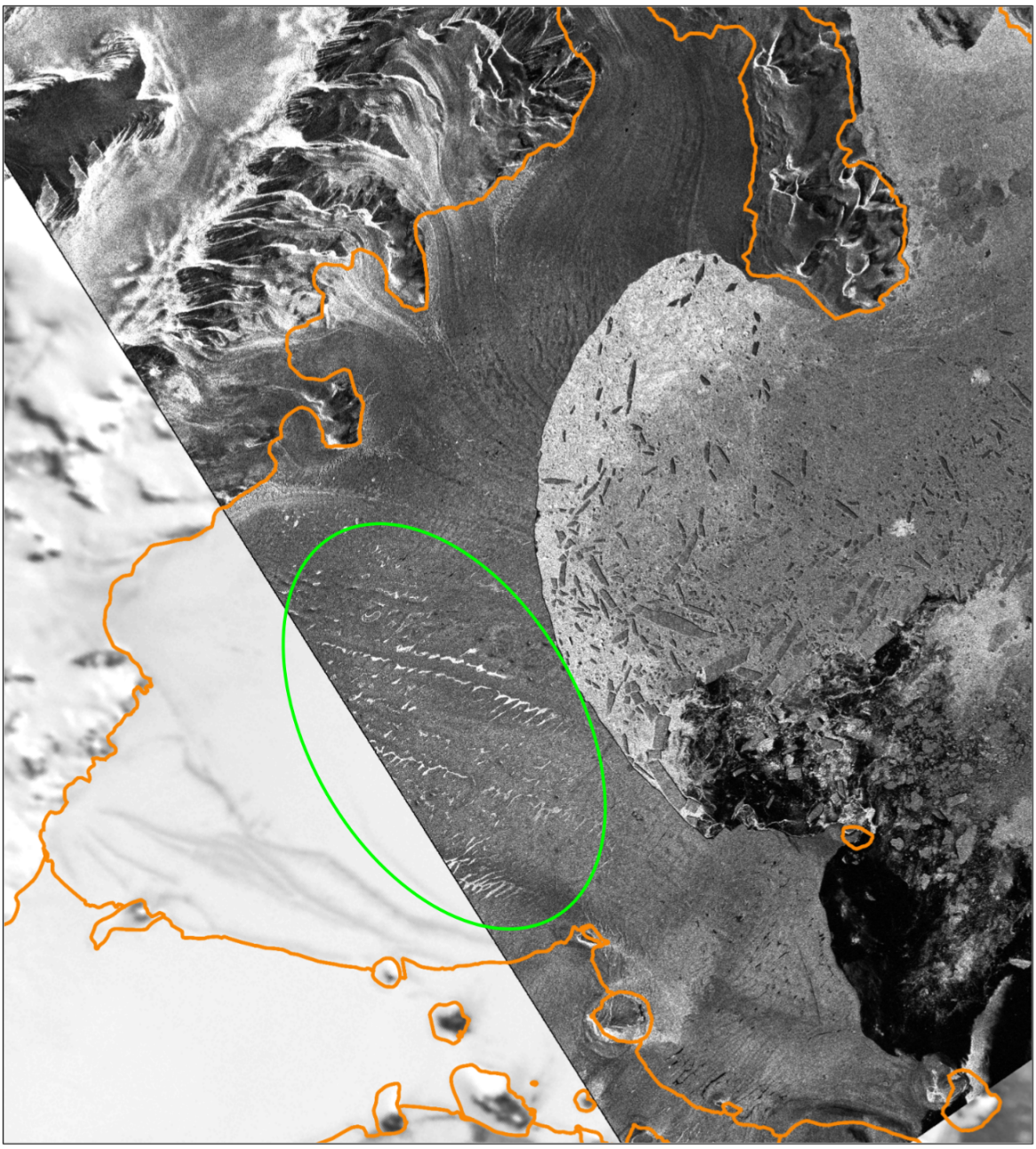

Figure B.3 Advanced Very High-Resolution Radiometer (AVHRR) image of the LAIS on January 28, 1995, with surface melt lakes identified with the green oval.. The solid orange line denotes the grounding line at the time of collapse.

APPENDIX C

Supporting Information for Ch. 4: The contribution of föhn and katabatic winds to ice sheet surface melt in Greenland and Antarctica

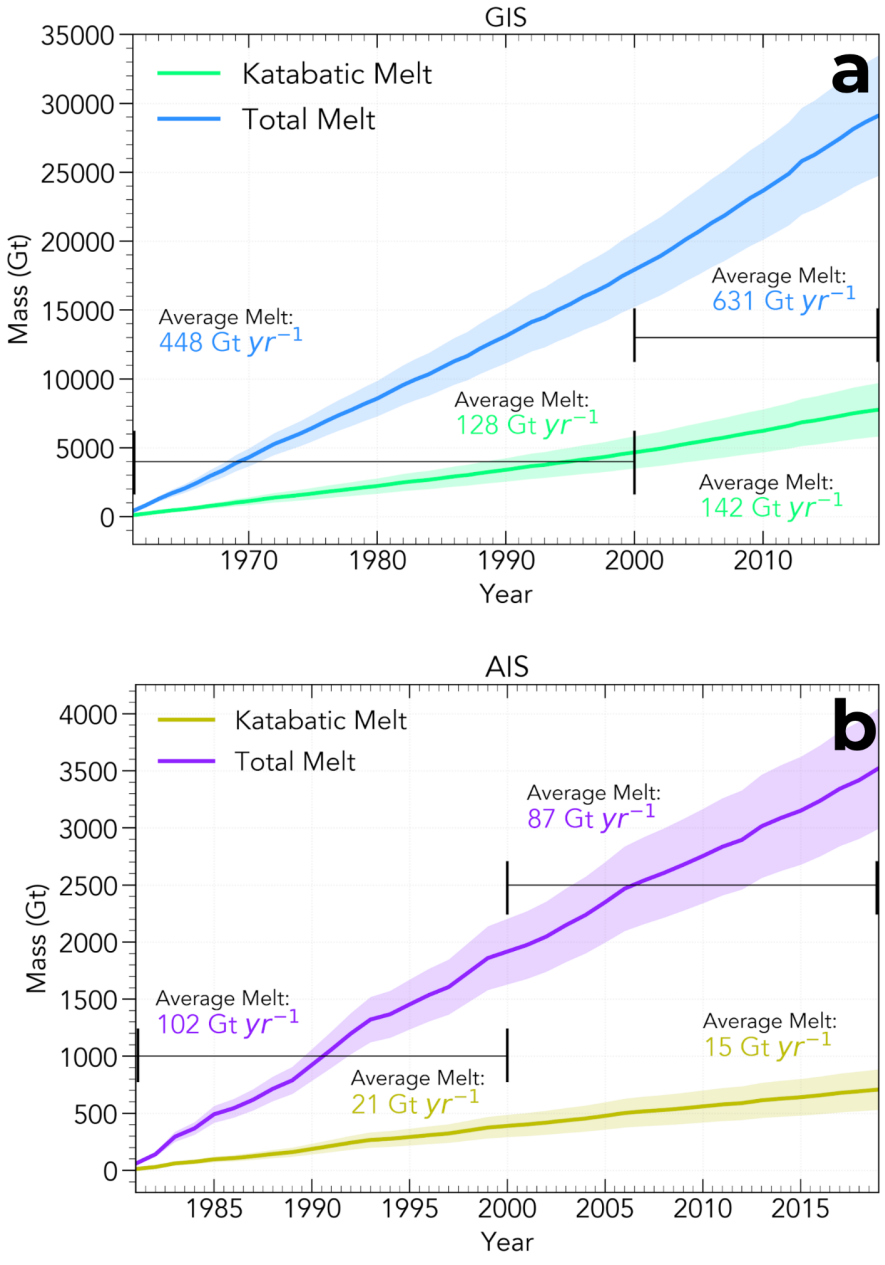

Figure C.1 (**a**) Cumulative surface melt on the GIS in total melt (blue) and melt associated with downslope winds (green) in gigatons (gigaton = 10^{12}kg) for the time period 1961-2019. (**b**) Cumulative surface melt on the AIS in total melt (purple) and melt associated with downslope winds (yellow) in gigatons (gigaton = 10^{12}kg) for the time period 1981-2019.

Table C.1 Melt and Energy Balance Statistics
Downslope winds (föhn and katabatic winds and associated melt) are identified in this table as "Kat". Trends on the GIS were calculated by comparing the first 40 years (1961-1999) with the second 20 years (2000-2019). Trends on the AIS were calculated by comparing the first 20 years (1981-1999) with the second 20 years (2000-2019). SW = net shortwave radiation, SHF = sensible heat flux, LW = net longwave radiation, LHF = latent heat flux. Positive energy values represent energy entering the ice from the atmosphere, while negative values represent energy leaving the ice to the atmosphere.

	GIS		AIS	
Kat melt	135 Gt/yr		18 Gt/yr	
Total melt	491 Gt/yr		91 Gt/yr	
% of total	27.5 ± 4.5%		19.7 ± 3.8%	
Kat melt trend	14 Gt/yr (10.3 ± 2.5%)		-5.8 Gt/yr (-31.8 ± 5.3%)	
Total melt trend	183 Gt/yr (34 ± 5.8%)		-15 Gt/yr (-15.4 ± 2.4%)	
Energy balance	**Melt**	**non-melt**	**Melt**	**non-melt**
SW-Kat	87 W/m²	24 W/m²	56 W/m²	22 W/m²
SW	82 W/m²	20 W/m²	50 W/m²	23 W/m²
SHF-Kat	12 W/m²	15 W/m²	18 W/m²	19 W/m²
SHF	10 W/m²	12 W/m²	17 W/m²	18 W/m²
LW-Kat	-42 W/m²	-36 W/m²	-38 W/m²	-36 W/m²
LW	-41 W/m²	-35 W/m²	-37 W/m²	-37 W/m²
LHF-Kat	-7 W/m²	-3 W/m²	-7 W/m²	-1 W/m²
LHF	-5 W/m²	-3 W/m²	-6 W/m²	-1 W/m²